Imaging the Relationship Between the Brain, Heart and Cardiovascular Disease Risk

Amy Isabella Sentis

Program in Neural Computation
Neuroscience Institute
Carnegie Mellon University

Committee:
Timothy D. Verstynen, Chair
Peter J. Gianaros
Leila Whebe
Tor D. Wager, Dartmouth

Submitted in partial fulfillment of the requirements
for the degree of Doctor of Philosophy

July, 2023

Abstract

Cardiovascular disease is the number one cause of death for humans worldwide [76]. While much is known about conventional risk factors for CVD [5, 23, 26, 75, 96, 105, 109, 160, 167, 176], as well as pharmacologic [32, 61, 139] and surgical [30, 117] therapies, comparatively little is known about the influence of the high-level brain areas (e.g., telencephalon, diencephalon) on early CVD pathophysiology and later stage CVD clinical risk. A growing body of work in human neuroimaging suggests that CVD risk may be associated with functional and structural brain measures [10, 66, 161, 166] and indeed that brain-based predictions of cardiovascular health outcome can rival the performance of conventional clinical markers [83, 84, 152]. Here we utilize machine learning methods on neuroimaging and cardiovascular data to investigate how neural variability associates with markers of CVD risk, including regulatory control of cardiac function. To do so, we test prediction accuracy and reliability and characterize the networks of brain regions most critical in the brain-heart relationships.

Acknowledgments

First and foremost, thank you to my advisor Tim Verstynen. You have been an incredible mentor, inspiring and helping me to become a better scientist and thinker and I am so thankful for your constant guidance and support. To Pete Gianaros, thank you for your encouragement and the direction and insight you provided on my projects. To my family, thank you for your unconditional love and support, I wouldn't be where I am today without you. To Jenna, I'm so grateful that we're on this journey together, thank you for being such a wonderful friend. Finally, to Harry, thank you for being such a supportive and encouraging partner and for always making me laugh.

Contents

List of Figures

Chapter 1

Introduction

1.1 Cardiovascular disease and risk

Cardiovascular disease (CVD) is the leading cause of death for both men and women in the United States, responsible for one out of every five deaths [76]. CVD is an umbrella term that encompasses many distinct types of heart disease, including coronary artery disease, heart failure, arrhythmia, valvular disease and cardiomyopathy, among others. Atherosclerotic coronary artery disease is the most common type of CVD, with 50% of Americans older than 45 [8, 13] and 10% Americans ages 33-45 living with some form of subclinical disease [8, 98]. Each year, 7% of deaths in the United States are attributed to overt coronary artery disease [8]. Numerous complications of CVD including ischemia and myocardial infarction contribute to the morbidity and mortality of the disease [6, 47]. Perhaps even more alarmingly, there exist persistent and increasing health disparities in the prevalence of CVD and resulting complications across racial and age groups, despite an overall decline in CVD prevalence [103, 104, 119].

Conventional risk factors for CVD include unmodifiable (age, sex, race/ethnicity), mod-

ifiable (BP, cholesterol and triglyceride levels), behavioral (smoking, BMI, diet, physical inactivity) as well as more recently recognized risk factors (systemic inflammation and biochemical markers, SES) [121]. During the development of treatment and therapies for CVD, there is an obvious focus on addressing risk factors that can be minimized. For example, regarding behavioral risk factors, extensive evidence has proven the detrimental effect of cigarette smoking on cardiovascular health. In particular, it has been shown to accelerate atherosclerotic plaque formation and trigger acute CVD events [9, 21]. High BMI is known to be associated with increased insulin resistance, systemic inflammation and clotting, imbalance of lipids and endothelial dysfunction [126]. Regular exercise is known to be protective in multiple ways - directly decreasing progression of atherosclerotic plaques and also helping to minimize other risk factors, including BP, BMI, and blood lipid and glucose levels [123]. Recent studies have also shown that social disadvantage is positively associated with increased risk of hypertension, diabetes, obesity, smoking, systemic inflammation, and CVD events and mortality [2, 86, 174].

Importantly, it is common for multiple cardiovascular risk factors to be prevalent within the same individuals concurrently [41, 102, 177]. Furthermore, risk factors combine and interact to increase an individual's total CVD risk profile, jumping from a four-fold risk from one factor to a 60-fold risk from five factors [41, 173]. It has also been demonstrated that the majority of CVD events do not occur in individuals that have a significant increase in risk due to only one risk factor, but rather occur in individuals with almost insignificant increases in numerous risk factors. An unfortunate result therefore is that death is the first and only CVD event [41]. Evidence from trends in CVD deaths support this, showing that even as rates of death from CVD are slowing, the total number of CVD events occurring is

rising [8, 41].

1.2 Neurocardiology: brain-heart relationships

While there has been significant study of the risk factors for CVD [5, 23, 26, 75, 96, 105, 109, 160, 167, 176] (including factors related to tobacco use, diet, sleep, physical activity and genetics), and pharmacologic [32, 61, 139] and surgical [30, 117] interventions and treatments, comparatively little is known about the influence of the brain on early CVD pathophysiology and later stage CVD clinical risk.

The brain plays a central role in regulating cardiovascular function and peripheral physiology, mainly via visceral control circuits, defined as cortical and subcortical brain regions that govern autonomic and neuroendocrine function across a range of behavioral states, as shown in Figure 1.1 [10, 66, 161, 166]. Given emerging epidemiological findings, it is hypothesized that these circuits may relate to CVD risk via intermediate peripheral physiological parameters under neural control [43, 45, 151]. Functional brain activity from magnetic resonance imaging (MRI) and PET has been linked to peripheral physiological parameters that confer CVD risk, such as markers of autonomic nervous system function, blood pressure, and heart rate [10, 66, 161, 166]. Indeed, the emerging field of neurocardiology [142, 143] has shown that late stage CVD outcomes, such as myocardial infarction and metabolic dysregulation, associate in longitudinal studies with baseline brain activity and the preclinical pathophysiological and peripheral end organ functions that the brain influences and regulates as part of its response to internal physiologic and external environmental triggers [84, 152]. There is also mounting evidence showing brain-based predictions of various cardio-

vascular health outcomes that rival the performance of conventional clinical markers. For instance, (a) PET/CT imaging of the amygdala demonstrated prediction of future adverse clinical CVD events (e.g. myocardial infarction, stroke, heart failure, coronary death) [152], (b) brain measures and activity from structural MRI and PET imaging predicted individual differences in blood pressure (BP) response to pharmacological treatment [84], and (c) measures of regional cerebral blood flow from MRI during a cognitively challenging task predicted longitudinal progression of BP [83].

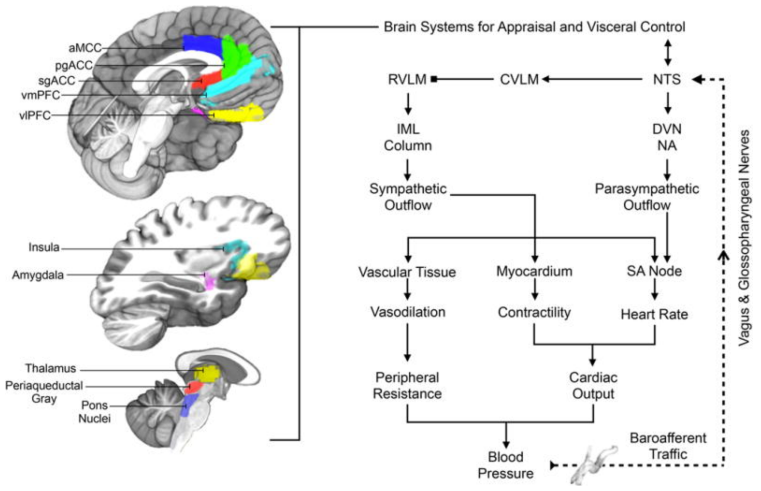

Figure 1.1: Schematic of visceral control circuit brain regions involved in physiologic mediators of cardiovascular health, likely via interactions with the baroreflex response, and also engaged by psychological stressors. Reproduced with permission from Gianaros and Wager, 2015.

Consider, for a moment, a central cardiac control function: heart rate. Heart rate has been shown to be a dominant risk factor for CVD [16, 124], for example, high resting heart rate is mechanistically linked to atherosclerosis [17, 39, 57, 116]. There is extensive evidence from animal studies [72, 113] and human lesion studies [36, 37, 155] that shows that heart

rate is under autonomic control via pattern generators in the brainstem [162]. A growing body of work from non-invasive human neuroimaging studies validates this link and offers the opportunity to further expand our knowledge about how networks of higher level brain regions interact with the brainstem's autonomic control [36, 37]. Much less is concretely known about which upstream brain regions regulate the brainstem via top-down modulation and the underlying mechanisms of such control. This is important knowledge as these same upstream regions react to emotional and environmental stressors, known processes that play a critical role in risk factors for CVD [42, 91, 153].

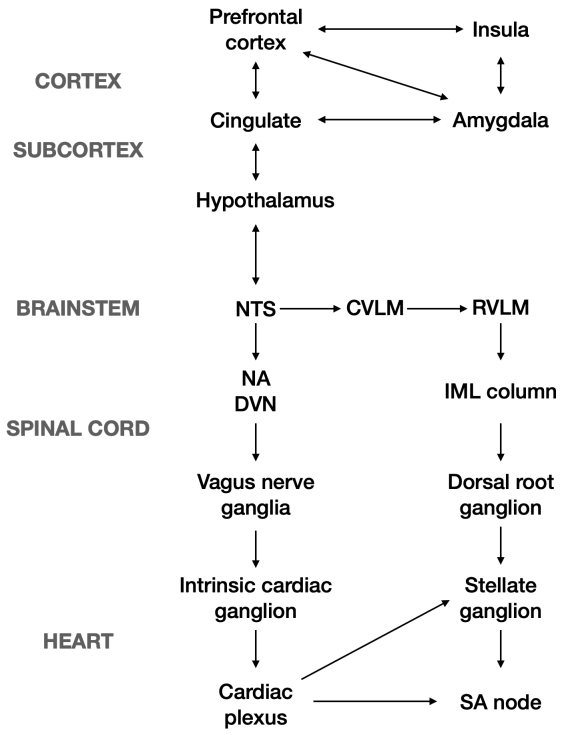

Figure 1.2: Schematic of autonomic regulation of heart rate through the SA node. NTS = nucleus tractus solitarius, CVLM = caudal ventrolateral medulla, RVLM = rostral ventrolateral medulla, NA = nucleus ambiguous, DMN = dorsal motor nucleus, IML = intermediolateral, SA = sinoatrial.

Figure 1.2 shows a schematic of brain regions and pathways associated with cardiac control. Multimodal recordings in animal models have shown connections between forebrain and midbrain regions, including prefrontal cortex, insula and amygdala [143]. Both animal studies and human neuroimaging metaanalysis provides evidence for associations between the hypothalamus and the nucleus tractus solitarius (NTS) in the brainstem [7, 138]. Anatomical pathways downstream of the brainstem can be separated into parasympathetic and sympathetic outflow tracts and have primarily been elucidated through animal studies, with human anatomical and neuorimaging studies providing additional confirmation. The parasympathetic outflow tract from the NTS activates through the nucleus ambiguous (NA) and dorsal motor nucleus (DMN), to the superior and then inferior ganglia of the Vagus nerve before reaching the intrinsic cardiac ganglia, which act as parasympathetic preganglionic synapses within the heart itself [7, 120, 154]. The sympathetic outflow tract from the NTS first traverses the caudal ventrolateral medulla (CVLM) to inhibit the rostral ventrolateral medulla (RVLM) within the brainstem. From the medulla, the tract continues through the intermediolateral (IML) cell column of the spinal cord to the dorsal root ganglion (preganglionic efferents) and the gray rami communicantes (postganglionic efferents) [7, 36, 120, 141, 154]. The parasympathetic and sympathetic outflow tracts converge at the cardiac plexus before reaching the sinoatrial (SA) node, which is the electrical pacemaker of the heart atria [79, 134, 141]. The stellate ganglion, located along the cervical sympathetic trunk also provides a sympathetic pathway between the cardiac plexuses and the SA node [54, 134].

Yet, to date, risk factors for CVD most conventionally refer to the unmodifiable, modifiable and behavioral risk factors discussed in section 1.1 [121]. Most of these predictors

of CVD risk are based on peripheral parameters (e.g. heart rate), they are not comprehensive, generally use late-stage outcomes, and do not incorporate the effects of visceral control circuits [84, 152]. Moreover, identification of pre-clinical disease in particular has not been amenable to existing methods and analytical strategies. Additionally, the mechanisms by which brain circuits relate to control of cardiac functions and physiological risk factors for CVD is not fully understood. Neurocardiology findings thus far have shown neural predictors to be independent of and complementary to these conventional risk factors [84, 152]. This raises the possibility that there may be value to be added to traditional risk prediction measures. In turn, this could pave the way for development of new therapies for CVD that target the brain and related processes, as has been done for hypertension [100, 112] and comorbidities of CVD, such as depression [48, 58].

It is clear that there is a wealth of opportunity for advancing our collective understanding of brain-heart connections and in particular our understanding of how the brain influences CVD risk. Addressing the field's open questions could have an important impact on treatment and prevention efforts, for example, the development of a brain-based biomarker that complements existing peripheral clinical predictors and that could be used as a surrogate outcome measure in future research. There is also the opportunity to develop novel therapies that take into account the role of the brain in regulating cardiovascular physiology and influencing risk to target early stage intervention, prior to the occurrence of adverse clinical events.

1.3 Specific aims

The first step towards development of novel risk factors, treatments, and prevention strategies for CVD is to more fully understand the role of the brain, in particular neocortical control mechanisms, in cardiac function and CVD risk. Our group has demonstrated that brain patterns and structural metrics identified by MRI and machine learning methods predict individual differences in a vascular marker of preclinical CVD risk, carotid-artery intima-media thickness (CA-IMT), as well as markers of autonomic and cardiovascular function [63, 64]. This thesis will replicate and extend these prior findings in novel ways using rigorous data science and machine learning methods, and larger datasets with multiple MRI modalities and state-of-the-art concurrent cardiovascular data. Specifically, we aim to understand how neural variability between individuals (Aim 1) and within individuals (Aim 2) associates with markers of CVD risk (Aim 1) and control of cardiac function (Aim 2).

Much of the CVD research focuses on late stage disease health outcomes, such as CVD mortality. This thesis instead focuses on subclinical disease - reflecting early, pathophysiological stages of atherosclerotic CVD. Such a focus is promising from a clinical and research perspective, given the increased likelihood of avoiding research confounds (e.g. medication use, clinical events, comorbidities) and the improved possibility of successful early intervention and prevention. More generally, this dissertation's focus on (1) the central neural control mechanisms of peripheral physiology as predictors of CVD risk, and (2) building reliable brain-based biomarkers for cardiovascular health, are advancements that can contribute to the growing field of neurocardiology.

In this dissertation I will explore two central aims at understanding brain-heart relation-

ships.

Specific Aim 1: Characterize brain networks predictive of individual differences in CA-IMT, a vascular marker of cardiovascular risk. We developed a stacked prediction model (linear support vector regression with random forests) that uses structural and functional brain measures from standard, clinically accessible MRI scans (T1 and resting-state fMRI) to predict individual differences in CA-IMT. We hypothesized that our multimodal model would reliably predict variability in CA-IMT across individuals and furthermore that the brain regions and subnetworks that comprise the visceral control circuits would be most influential in the prediction of CA-IMT. For this aim, we intentionally implemented parsimonious models that can be readily extended to address questions about how our models relate to existing risk factors: Are our models independent of conventional CVD risk factors, or do they add predictive value synergistically? Do conventional CVD risk factors modify observed associations between brain activity and early stage markers of CVD risk? Aim 1 is addressed in Chapter 2.

Specific Aim 2: Characterize brain networks predictive of prevailing heart rate within individuals, an important component of cardiovascular risk. We developed a machine learning model from neuroimaging data that predicts dynamic changes in the prevailing heart rate from instantaneous fMRI measures with concurrent ECG data within individuals. Sub Aim 2.a: Develop a python toolbox to extract and clean physiological signals obtained during MRI. Sub Aim 2.b: Use L1-constrained principal component regression (LASSO-PCA) on fMRI data to create a model that predicts instantaneous heart rate. Hypothesis 2.1: Our model will reliably predict modulation of heart rate from hemodynamic responses in the brain. Hypothesis 2.2: The brain regions that are most important for this prediction are

the visceral control circuits. Transient fluctuations in the activity of upstream brain regions comprising the visceral control circuits should track with transient fluctuations of heart rate (because these upstream brain regions control the descending pathways that regulate heart rate). This would bolster our argument about the benefits of studying the brain to more fully understand CVD. Chapters 3 and 4 focus on Specific Aim 2.a and 2.b, respectively.

The overarching hypothesis that connects my thesis projects is as follows: we hypothesize that neural biomarkers, influenced primarily by visceral control circuits, will reliably predict peripheral markers of CVD risk, such as mean CA-IMT and prevailing heart rate.

Chapter 2

Multimodal Imaging and Subclinical Atherosclerosis

The following text was adapted from Sentis, Rasero, Gianaros, and Verstynen 2022 [140].

Human neuroimaging evidence suggests that cardiovascular disease (CVD) risk may relate to functional and structural features of the brain. The present study tested whether combining functional and structural (multimodal) brain measures, derived from magnetic resonance imaging (MRI), would yield a multivariate brain biomarker that reliably predicts a subclinical marker of CVD risk, carotid-artery intima-media thickness (CA-IMT). Neuroimaging, cardiovascular, and demographic data were assessed in 324 midlife and otherwise healthy adults who were free of (a) clinical CVD and (b) use of medications for chronic illnesses (aged 30-51 years, 49% female). We implemented a prediction stacking algorithm that combined multimodal brain imaging measures and Framingham Risk Scores (FRS) to predict CA-IMT. We included imaging measures that could be easily obtained in clinical settings: resting state functional connectivity and structural morphology measures from T1-weighted images. Our models reliably predicted CA-IMT using FRS, as well as for several individual

MRI measures; however, none of the individual MRI measures outperformed FRS. Moreover, stacking functional and structural brain measures with FRS did not boost prediction accuracy above that of FRS alone. Combining multimodal functional and structural brain measures through a stacking algorithm does not appear to yield a reliable brain biomarker of subclinical CVD, as reflected by CA-IMT.

2.1 Introduction

Cardiovascular disease (CVD) encompasses many heart and vascular conditions that contribute to a primary cause of death for both men and women in the United States [164]. Atherosclerotic coronary artery disease is the most common CVD, with 50% of Americans older than 45 [13, 164] and 10% Americans ages 33-45 living with some form of subclinical disease that prestages later clinical conditions [98, 164]. In 2018, 13% of deaths in the United States were attributed to overt coronary artery disease [164]. Numerous complications of atherosclerotic CVD, including ischemia and myocardial infarction, contribute to morbidity and mortality [6, 47].

Typically, CVD is not considered in relation to brain-based biomarkers. For example, most clinical diagnostic and assessment criteria, like the Framingham Risk Score [40], focus on peripheral physiological factors, health behaviors (e.g., smoking), and demographics to predict someone's risk of CVD [51, 87]. Yet, there is cumulative evidence that structural and functional features of the brain associate with CVD risk factors and that CVD risk factors (e.g., blood pressure, lipid levels, etc.) may be precursors to neurocognitive decline, some dementias, and brain aging [107, 147].

There are both efferent and afferent mechanisms by which brain structure and function can be linked to subclinical CVD. On the efferent or brain-to-body side, the brain systems for autonomic, neuroendocrine, and immune control shape peripheral physiology in ways that confer CVD risk [66, 152]. For instance, recent findings suggest the possibility that increased amygdala activity may increase hematopoietic tissue activity, which in turn leads to increased arterial inflammation and incident CVD events [152]. There is also a large body

of evidence supporting afferent or body-to-brain contributions as well, with longstanding evidence linking risk factors for CVD to premature brain aging, including cognitive decline [101, 147]. Hence, it is well established that CVD is a risk factor for neurocognitive decline [111, 148]. Carotid-artery intima-media thickness (CA-IMT), a surrogate measure of preclinical atherosclerosis [63], is associated with risk factors for CVD (and cerebrovascular disease), including hypertension, diabetes and smoking [38]. Moreover, CA-IMT itself has been shown to associate with progressive cognitive decline [171] and increased risk of dementia [169]. In these regards, CA-IMT may plausibly reflect decreased perfusion of brain tissue as reflected by reduced CBF, which in turn can result in silent brain infarctions and microvascular damage as precursors to neurocognitive decline [107].

In fact, many CVD outcomes, such as myocardial infarction and preclinical markers of CVD risk, have recently been associated with functional and structural features of macroscopic brain systems. Longitudinal studies, for example, suggest that baseline metabolic activity in the amygdala predicts future myocardial infarction and components of the metabolic syndrome [152], and that baseline levels of stress reactivity in the rostromedial prefrontal cortex are associated with future major adverse cardiovascular events [106]. Moreover, structural MRI measures of brain aging (composite measures of ventricle size, sulcal size and white matter hyperintensities) and regional cerebral blood flow relate to individual differences in the magnitude of blood pressure lowering induced by antihypertensive medication [84], as well as the longitudinal progression of blood pressure over multiple years [83]. Lastly, functional activation in insular, anterior cingulate, medial prefrontal, hypothalamus and brainstem regions, measured in response to mental stress and emotional stimuli, has been shown to predict clinical CVD events [106], mental stress-induced blood pressure reactivity [64],

and CA-IMT [63].

It is also important to consider the influence of the cardiovascular system on the brain. For example, carotid artery stenosis, narrowing of the carotid artery usually due to atherosclerosis (plaque build-up), has been theorized to have a negative effect on cognitive function through reduced blood flow to the brain in asymptomatic cases and ischemic brain damage in symptomatic cases [168]. Nickel and colleagues studied patients with high-grade carotid artery stenosis without ischemic brain lesions. Patients had lower cognitive function compared to controls, however there was no corresponding association with cortical thickness [110]. Cheng and colleagues also studied patients with asymptomatic carotid artery stenosis and found that patients displayed lower cognitive and memory performance than controls and this difference correlated with disruption in resting-state functional connectivity (FC) across multiple networks [31]. Thus, given the associations between cardiovascular system and neurocognitive systems, it should be possible to identify a reliable, predictive association between brain measures and preclinical markers of CVD.

At present, however, there is largely mixed evidence as to whether there are reliable functional and structural brain imaging correlates of subclinical markers of CVD, particularly indexed by CA-IMT. Functional evidence shows, for example, that CA-IMT is associated with higher regional cerebral blood flow in some areas (medial frontal gyrus, putamen, and hippocampal regions), but also lower regional cerebral blood flow in other areas (lingual, inferior occipital, and superior temporal regions) [145]. Other findings indicate that CA-IMT associates with lower cerebral blood flow (CBF) in gray matter and across the entire brain [27]. This association with CBF is particularly interesting given ongoing work showing that variability in CBF is detectable in the resting blood oxygenation level dependent (BOLD)

signal measured with functional MRI (fMRI). For example, work by Fukunaga and colleagues (2008) utilized the ratio between BOLD signal activation and cerebral blood perfusion to demonstrate that resting-state activity incorporates both a neuronal or metabolic component as well as a vascular component (i.e., blood flow; [60]). Furthermore, cerebral perfusion has been shown to correlate with resting-state BOLD signal and connectivity in terms of spatial distribution across the brain [165]. Since CA-IMT is associated with CBF, and CBF is associated with the resting state BOLD signal, this would appear to support the possibility of detecting associations across individuals in the variability of CA-IMT as related to the resting BOLD signal itself.

Separately from functional neuroimaging studies, there is structural brain imaging evidence indicating that CA-IMT is inversely associated with total brain tissue volume, as well as cortical tissue volume more specifically [108, 159]. In parallel, however, other lines of evidence suggest no association between CA-IMT and total brain tissue volume or gray matter tissue volumes [27]. Lastly, some structural neuroimaging findings suggest an inverse association of CA-IMT and cortical thickness [24], but again not all findings are consistent with the latter observations [3]. This heterogeneity in functional and structural brain imaging findings, as well as the isolated (unimodal) treatment of functional and structural brain imaging measures have created an open question as to whether the simultaneous (multimodal) modeling of functional and structural brain features would combine to predict a known marker of subclinical CVD and predictor of future clinical events; namely, CA-IMT. Moreover, whether such multimodal modeling would add to the prediction of subclinical CVD beyond established demographic, behavioral, and biological risk factors is unknown.

To elaborate, a majority of studies on the brain correlates of CVD risk, particularly

CVD markers such as CA-IMT, use conventional analytical approaches that include univariate correlation and regression methods. A problematic feature of these methods is that they are not combined with out-of-sample validation testing, limiting inferences about model and sample generalizability. Moreover, these studies have historically relied on brain measures from a single neuroimaging modality, e.g., task-based or resting-state fMRI, structural connectivity, metabolic activity via PET. Such unimodal analyses do not exploit or account for the distinct neurobiological properties of different neuroimaging modalities, that when combined may improve predictive power. Lastly, a focus thus far on the brain correlates of CVD risk has been on particular neural systems or networks, rather than all systems and networks across the entire brain. Taken together, it appears that integrating and combining whole-brain modalities into a transmodal machine learning model [133, 175] has the potential to overcome methodological limitations to improve the predictive utility and robustness of putative brain biomarkers of CVD risk to facilitate replication and generalization.

In the above regards, an effective biomarker or multimodal brain correlate of CVD risk would have the following characteristics. First, it would take into account the unique variability inherent to the different measures derived from imaging modalities (e.g., cortical thickness, cortical surface area, and tissue volumes derived by structural MRI, as well as dynamic activity measures reflecting neural networks derived by fMRI). Second, it would rely on either standard clinical brain imaging sequences (e.g., T1 weighted anatomicals) or MRI data acquisition sequences that are amenable to clinical contexts and testing in diverse populations of people (e.g., resting-state fMRI). Third, it would reliably predict CVD risk, not just associate with it (e.g., out of sample validation testing). Finally, a reliable brain correlate of CVD risk would account for additional variability above-and-beyond that already

accounted for by other established risk factors for CVD. To these ends, the present study examined whether morphological and basic functional measures derived from T1-weighted and resting-state fMRI data could be combined in a multimodal machine learning analysis framework (with predictor variables comprised of cortical surface area, cortical thickness, subcortical volumes and whole-brain resting-state FC) to reliably predict inter-individual variability in CA-IMT in a sample of neurologically healthy adults. For this we modified an identical multimodal machine learning approach used previously to predict "brain age" [93] - a measure of brain aging when compared to chronological age that has been shown to correlate with numerous risk factors of CVD, including smoking and diabetes [33]. We then evaluated performance against the prediction of CA-IMT by Framingham Risk Score [40].

2.2 Methods

2.2.1 Participants

Neuroimaging, cardiovascular, and demographic data were collected from N=324 healthy participants (ages 30-51, 49% female) from the Pittsburgh Imaging Project (see Table 1). All participants provided informed consent. The University of Pittsburgh Human Research Protection Office granted study approval. Detailed information about the study population has been published in [63]. This is the first report bearing on the multimodal prediction of CA-IMT from this sample and these results have not been published previously. Data and code are available at https://github.com/CoAxLab/multimodal-imt.

Characteristic	Mean or (%)	SD
Age (years)	40.3	6.28
Race (%)		
Caucasian	66	
African-American	28.4	
Multiracial/ethnic	5.6	
BMI (kg/m^2)	26.93	5.07
Smoking status (%)		
Never	62.65	
Former	20.06	
Current	17.28	
Systolic BP (mm Hg)	120.8	10.01
Diastolic BP (mm Hg)	72.63	8.75
Seated resting HR (bpm)	74.1	9.63
Glucose (mg/dL)	88.34	9.75
HDL (mg/dL)	50.73	16.06
Triglycerides (mg/dL)	94.43	56.94
CA-IMT (mm)	0.61	0.08
FRS	5.35	5.99

Table 2.1: Sample Characteristics (N=324; 164 Men, 160 Women). Note: SD = standard deviation, BMI = body mass index, BP = blood pressure, HDL = high-density lipoproteins, CA-IMT = carotid artery intima-media thickness, FRS = Framingham Risk Score.

2.2.2 Preclinical atherosclerosis

Carotid-artery IMT was measured at three locations (distal common carotid artery, carotid artery bulb, and internal carotid artery) by trained ultrasound sonographers using an Acuson Antares ultrasound device (Acuson-Siemens, Malvern, PA). Measurements were obtained on both the left and right carotid artery in three specific locations: 1) both the near and far walls of the distal common carotid artery, located 1 cm proximal to the carotid bulb (the location

at which the near and far walls of the common carotid are no longer parallel and extending to the flow divider), 2) far wall of the carotid bulb, and 3) the first centimeter of the internal carotid measuring from the distal edge of the flow divider. These three measurements were then averaged bilaterally and across locations to calculate the mean CA-IMT, which was used as the outcome variable. Further information about measurement methods and test-retest reliability of CA-IMT measurements can be found in [63]. Figure 2.1 panel A shows example images of IMT acquisition. Figure 2.1 panel B shows the CA-IMT values in our sample, which are approximately normally distributed [94, 128].

2.2.3 Framingham risk

Framingham Risk Score (FRS) was calculated for each participant according to [40]. This metric incorporates age, sex, smoking, hypertension and cholesterol data from each participant. Five participants had missing FRS data. For analysis purposes, these missing values were imputed using the mean FRS. Figure 2.1 panel C shows the distribution of FRS.

2.2.4 MRI data acquisition and processing

Functional blood oxygenation level-dependent images were collected on a 3 Tesla Trio TIM whole-body scanner (Siemens), equipped with a 12-channel phased-array head coil. Resting-state functional images were acquired over a 5-minute period with eyes open and the following acquisition parameters: FOV = 205×205mm, matrix size = 64×64, TR = 2000ms, TE = 28ms, and FA = 90°. Thirty-nine slices (interleaved inferior-to-superior, 3mm thickness, no gap) were obtained for each of 150 volumes (three initial volumes were discarded to allow for magnetic equilibration). T1-weighted neuroanatomical magnetization prepared

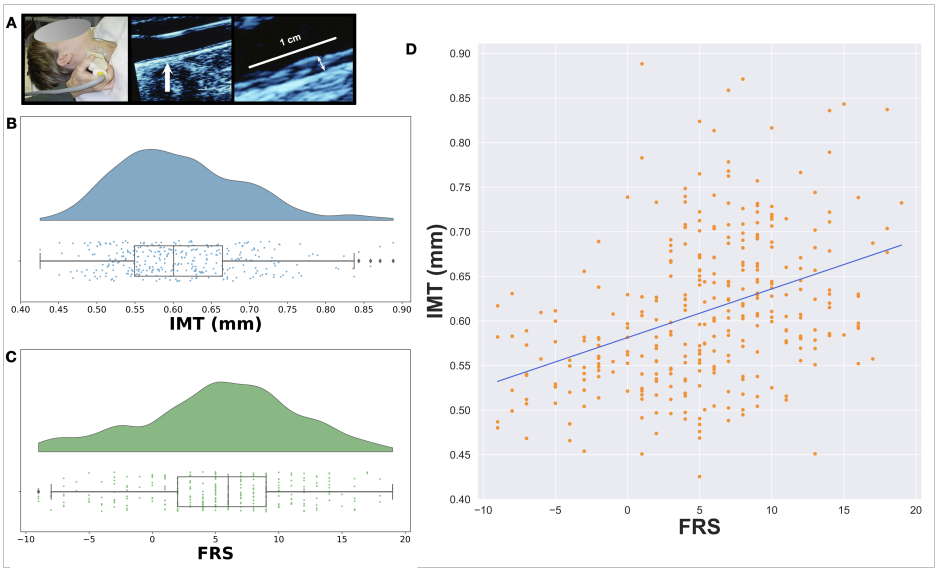

Figure 2.1: A) Left panel shows CA-IMT acquisition using ultrasound. Middle and right panels show example ultrasound images with the CA-IMT indicated. B) Raincloud plot showing distribution of CA-IMT (mm) in our sample. C) Raincloud plot showing distribution of FRS in our sample. D) Scatterplot showing the linear regression of FRS on CA-IMT. Line of best fit shown in blue. CA-IMT = carotid artery intima-media thickness, FRS = Framingham Risk Score.

rapid gradient echo (MPRAGE) images were acquired over 7 min 17 sec with the following parameters: FOV = 256×208mm, matrix size = 256×208, TR = 2100ms, inversion time = 1100ms, TE = 3.31ms, and FA = 8° (192 slices, 1mm thickness, no gap).

Resting-state fMRI data were preprocessed using SPM12 and included slice-timing correction, realignment to the first image using a six-parameter rigid-body transformation, co-registration to skull-stripped and biased-corrected MPRAGE images, normalization to standard Montreal Neurological Institute (MNI) space and smoothing using a 6mm full-width-at-half-maximum (FWHM) Gaussian kernel. Head motion at the individual participant image level was estimated via framewise displacement (FD) according to Power et al.,

2015 [130] for use during FC processing (described further below).

Resting-state data were denoised, including six motion parameters, white matter (WM), cerebrospinal fluid (CSF), and global signal (GS). The first principal component for each of WM, CSF and GS was used. Data were also bandpass filtered with a range of 0.009 - 0.08 Hz. A functional correlation matrix was calculated using the Craddock 200 parcellation [34] by first computing the average time series from the voxels within each of the 200 parcels, and then calculating the z-transformed Pearson correlation coefficient between pairs of parcel time series. The upper triangular elements were extracted from the functional correlation matrix to form a vector of 19,900 FC features for each participant. FD was regressed out and the final FC vector for each participant is comprised of the resultant residuals. By this approach, correlations that are partial for FD between all possible ROIs in the Craddock atlas.

MPRAGE images were analyzed using FreeSurfer (v6), with 148 cortical thickness and cortical surface area measures from the thickness and area freesurfer files respectively, using the Destrieux Atlas [46], as well as 67 subcortical volume measures directly extracted from the aseg.stats freesurfer file of each participant.

2.2.5 Multimodal prediction of IMT

We adopted a transmodal approach to stacking learning for prediction of CA-IMT [133, 175]. In machine learning, stacking is classified as an ensemble learning method and involves combining predictions from a set of models into a new meta feature matrix for subsequent input into a new model for final prediction [93, 135].

As detailed in Figure 2.2, our model comprised a two-step process that used multiple

output predictions for each participant from a first level support vector regression (SVR) model as the inputs into the second level random forest model. The set of first level SVR models used different groups of features, or channels, corresponding to 1) resting-state FC, 2) cortical surface area, 3) cortical thickness and 4) subcortical volume measures. Performance of the predictive models at the first and second levels of analyses was determined using cross-validation. This model was predicated on the work of Liem et al., 2017, who used this transmodal approach to predict brain age. In order to validate our model implementation, we predicted brain age in our sample and compared the results to those presented in Liem et al., 2017.

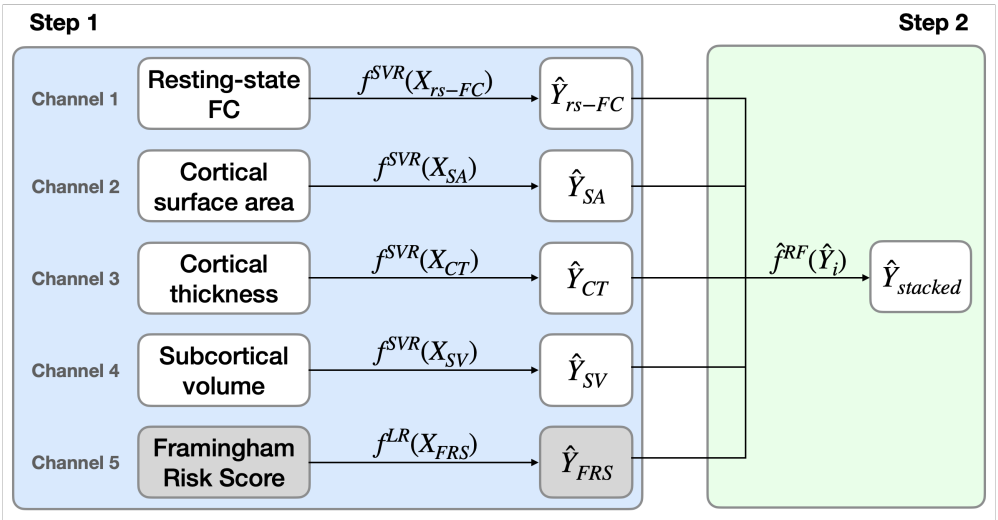

Figure 2.2: Prediction stacking model schematic, with linear SVR and linear regression used in the unimodal predictions and random forest used in the multimodal prediction. FC = functional connectivity, SVR = support vector regression, LR = linear regression, RF = random forest.

To do so, we first split the data such that 80% were used for training and the remaining 20% for testing. Next, we used five-fold cross-validation during the training stage to generate

out-of-sample SVR predictions for each channel on the training set data. We used a previously tuned parameter, C, for this type of data from Liem et al., 2017. As input into the second level, the out-of-sample predictions from the training set as well as the test set predictions were stacked across channels, forming new matrices of 80% observations x 4 channels and 20% observations x 4 channels, respectively. The second level random forest model was then tuned for the tree depth hyperparameter and trained using five-fold cross-validation to generate out-of-sample predictions on the new training matrix and tested on the new test matrix to generate the final predictions for brain age. Performance of the single-channel and stacked models was then evaluated by comparing participant's chronological age with the participant's predicted brain age in the out-of-sample test data. Prediction error was measured using the coefficient of determination, R-squared, and the root mean squared error (RMSE). All predictive analyses were performed using scikit-learn [122].

Once validated using age, this analysis pipeline was used to predict CA-IMT as the target outcome variable. An additional fifth channel consisting of a participant's FRS was included in this pipeline. Since over parameterization is not a concern with a single feature model, simple linear regression (LR) was used for the single channel prediction of CA-IMT from FRS. Thus, five single channels (four brain measures plus FRS) were stacked as input into the second level random forest model. Performance was similarly evaluated through comparison of observed CA-IMT values with the predicted CA-IMT values in the out-of-sample test data.

We subsequently evaluated and compared model performance on CA-IMT prediction for every possible combination of single data channels, again using the coefficient of determination, R-squared, representing model goodness-of-fit as the measure of model performance.

Finally, in order to test robustness of our analysis and confirm that results were not dependent on a particular training/testing data split, we generated 100 random training/testing splits, using different random seeds, for analysis through our cross-validated, channel combination implementation. Final model performance was evaluated using the median of the Pearson correlation coefficient, coefficient of determination, RMSE and Bayesian information criterion (BIC) values of each partition.

2.3 Results

We first tested whether we could confirm previously reported patterns in our data set. Our primary outcome measure, mean CA-IMT, was measured using ultrasound (Fig. 2.1 panel A; see Methods 2.2.2). Consistent with the assumptions of our statistical models, these CA-IMT values across our sample were approximately normally distributed (Fig. 2.1 panel B), with a slight skew, in ranges consistent with an unbiased sample across the population [149]. We next wanted to replicate the well established relationship between FRS and CA-IMT [127, 136]. FRS values were approximately normally distributed (Fig. 2.1 panel C). As expected the linear regression of the association between FRS and CA-IMT confirms a positive association, with a Pearson correlation coefficient of $r=0.3857$, $p < 0.001$ (Fig. 2.1 panel D). Taken together, these results are in line with the literature and constitute a replication of effects shown previously [49, 127, 136].

In order to validate the feasibility of our transmodal stacking approach, we first attempted to replicate the findings of Liem et al., 2017 and predict chronological age using morphological brain measures as well as resting-state FC. This prior study was able to pre-

dict chronological age from the same imaging measures used here, with an accuracy of +/- 4 years. Implementing our own version of the pipeline, applied it to our sample, revealed an association between chronological age and predicted brain age that was positive and equivalent in magnitude to the original report, with a Pearson's correlation coefficient of r = 0.5246, p <0.001 and coefficient of determination, R-squared = 0.2732 for the hold-out test set. Figure 2.3 shows the observed versus predicted scatter plot for chronological age and brain age. Our age prediction error (≈ 4 years) approximated that of the results presented in Liem et al., 2017, confirming the validity of our stacking approach.

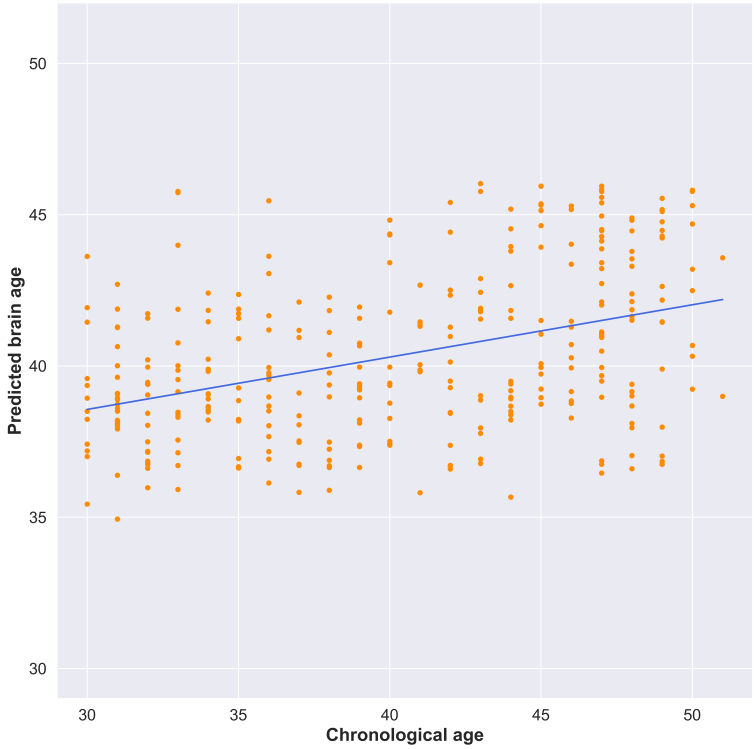

Figure 2.3: Scatterplot showing correlation between participants' chronological age and predicted brain age according to multimodal model. Blue line represents the line of best fit.

In order to evaluate our primary aim of determining whether clinically obtainable brain imaging measures boost the prediction accuracy of individual differences in markers of CVD risk, we applied our stacked learning approach to predicting CA-IMT. Figure 2.4 shows the distribution of four different metrics for each random Monte Carlo data partition for both the single channel predictions of CA-IMT, as well as every possible channel combination for the second level random forest prediction of CA-IMT. Panel A shows Pearson correlation coefficients, r values, panel B shows RMSE values (with the horizontal dotted line representing the standard deviation of CA-IMT in our sample, 0.084 mm), panel C shows coefficient of determination, R-squared values, and panel D shows BIC values.

Across all panels, the blue bars show the first level SVR and linear regression CA-IMT predictions using the single channel brain measures and FRS. Figure 2.4 panel A shows that FRS has the largest median Pearson correlation coefficient, r = 0.3916 (95% CI [0.3739, 0.4058]), with the brain measures showing much smaller associations (resting-state FC median r=-0.0132 (95% CI [-0.0375, 0.0096]), cortical SA median r=0.1111 (95% CI [0.0959, 0.1402]), cortical thickness median r=0.1373 (95% CI [0.1237, 0.1560]), subcortical volume median r=0.1435 (95% CI [0.1245, 0.1646])). Figure 2.4 panel B demonstrates that the single channel predictions of CA-IMT from the brain measures had the largest median RMSE values (resting-state FC median RMSE=0.0869 mm, cortical SA median RMSE=0.0868 mm, cortical thickness median RMSE=0.0862 mm, subcortical volume median RMSE=0.0.0974 mm), and were higher than the standard deviation of CA-IMT (Fig. 2.4B). The single channel FRS prediction of CA-IMT had the lowest RMSE out of all models, with a median RMSE=0.0778 mm, and was the only single channel model with an RMSE value beneath the standard deviation of CA-IMT in our sample. Figure 2.4 panel C shows that median R-

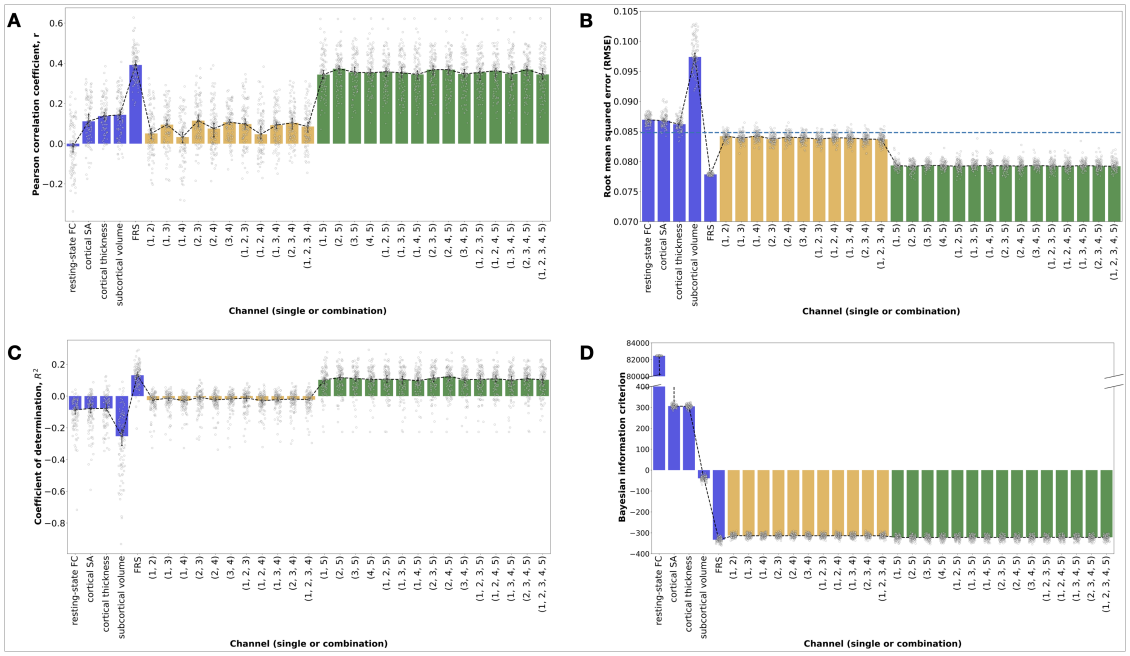

Figure 2.4: For all panels, blue bars show single channel predictions of CA-IMT. Yellow bars show channel combination predictions that include only brain measures. Green bars show channel combinations predictions that include FRS. Error bars indicated 95% confidence intervals (calculated using 1000 bootstrap iterations). Channel combinations are indicated numerically with 1 = resting-state FC, 2 = cortical SA, 3 = cortical thickness, 4 = subcortical volume, 5 = FRS. Median values for the Monte Carlo simulation for single channel and every possible channel combination prediction of mean CA-IMT: A) Pearson correlation coefficient, r, B) RMSE (horizontal dotted line represents the standard deviation of CA-IMT in our sample, 0.084 mm), C) coefficient of determination, and D) Bayesian information criterion. CA-IMT = carotid-artery intima-media thickness, FRS = Framingham Risk Score, FC = functional connectivity, SA = surface area.

squared values for the single channel brain measure predictions of CA-IMT are all negative, indicating that our model does not appropriately predict CA-IMT using brain measures. However, the median R-squared value for single channel prediction of CA-IMT using FRS is positive, R-squared=0.1314 (95% CI [0.1139, 0.1421]), indicating that FRS accounts for over 13% of the variance in CA-IMT. Figure 2.4 panel D shows a large range of BIC values for

the single channel predictions of CA-IMT, with FRS being the most negative (resting-state FC median BIC = 82,454, cortical SA median BIC = 306.18, cortical thickness median BIC = 305.06, subcortical volume median BIC = -38.99, FRS median BIC = -332.89). Note that BIC reflects the amount of information lost by a model, so lower values are better. This confirms the results from panels A-C, demonstrating that the FRS single channel model is preferred over the single channel brain measure models.

In all panels, the yellow bars show the second level random forest CA-IMT predictions from the channel combinations comprised of brain measures only. Figure 2.4 panel A shows the median Pearson correlation coefficients, which ranged between r=0.0328 (95% CI [0.0025, 0.0467]) and r=0.1143 (95% CI [0.0963, 0.1383]). Stacking only the brain measures did not improve performance accuracy over the best single channel brain measure. Figure 2.4 panel B shows the RMSE values, which hovered around the standard deviation of CA-IMT, and slightly improved upon the RMSE values of the single channel brain measures. Figure 2.4 panel C shows that median R-squared values for the channel combination predictions of CA-IMT using only brain measures are all negative, albeit less negative than the R-squared values from the single channel brain models. This indicates that our model does not appropriately predict CA-IMT using brain measures. Figure 4D shows improved median BIC values for the channel combination predictions of CA-IMT using only brain measures compared to that of the single channel brain measure models, ranging from BIC=-312.89 to BIC=-314.22. However, these BIC values do not improve upon the median BIC value from the single channel FRS model, indicating that a combination of brain measures will not be a better feature selection choice than FRS.

In all panels of Figure 2.4, the green bars show the second level random forest CA-IMT

predictions from the channel combinations that include FRS. Individually, some brain measures perform above chance in predicting CA-IMT, specifically the morphometry measures from T1, when looking at the correlation between observed and predicted values. However, the effect size is smaller compared to that of the single channel FRS model. In Figure 2.4 panel A, the median predicted vs. observed correlation values for the channel combinations that include FRS were more than three times that of the maximum value of the channel combinations that only include brain measures, ranging between r=0.3436 (95% CI [0.3261, 0.3653]) and r=0.3727 (95% CI [0.3412, 0.3772]). Figure 2.4 panel B shows that the inclusion of FRS resulted in a reduction in median RMSE values, hovering around 0.079 mm. Figure 2.4 panel C demonstrates positive median R-squared values for the channel combination predictions of CA-IMT that include FRS, ranging between R-squared=0.09 (95% CI [0.0731, 0.1051]) and R-squared=0.11 (95% CI [0.0810, 0.1131]), though all are lower than that of the single channel FRS model. Similarly, Figure 2.4 panel D shows median BIC values that are smaller than that of the channel combinations that only include brain measures, but larger than that of the single channel FRS model, ranging between BIC=-320.90 and BIC=-322.23. Adding in FRS resulted in an overall increase in performance across all metrics shown in Figure 2.4. However, this is solely driven by FRS, as none of the channel combinations that include FRS perform better than FRS alone. These results indicate that brain measures do not assist in the prediction of CA-IMT beyond FRS.

2.4 Discussion

Our goal for this study was to evaluate whether structural and functional brain measures from standard, clinically accessible MRI scans (T1 and resting-state fMRI) could be used to boost prediction of a marker of preclinical CVD above what is achievable from more standard clinical metrics, namely the FRS. Results show that our stacking algorithm is a sound methodology. We also see a strong association between FRS and CA-IMT, as expected. By comparison, we fail to find an improvement in our model predictions when using these brain measures individually, or in combination.

Our findings emphasize the complex nature of the role of the brain in CVD risk. Emerging mechanistic insights that link markers of CVD risk with structural and functional brain measures provide support for the need to further understand the role of the brain in CVD risk. Subclinical markers of CVD risk have been shown to associate with cerebral hypoxia and silent brain infarctions [131]. CVD risk factors (such as smoking, diabetes, obesity, hypertension) also demonstrate associations with inflammation, oxidative stress, brain atrophy, ischemic changes and reduced CBF, which can also contribute to neurocognitive decline [20, 89, 118, 146, 172]. In addition, there is emerging evidence that functional and structural alterations within the brain, particularly in brain systems for peripheral physiological control, may confer CVD risk via efferent or brain-to-body pathways [66]. Thus, based on this evidence in the literature, we predicted CA-IMT could connect with resting-state fMRI in two ways (body-to-brain and brain-to-body pathways), yet failed to detect an association.

Alignment of our work with prior literature is seen in a few different ways. Firstly, we replicate existing findings that demonstrate a substantial relationship between FRS and CA-

IMT [49, 127, 136]. Secondly, our methodological approach replicates that of Liem et al., 2017 in a new sample, validating stacked learning as a useful tool for predicting individual differences from MRI-based measures. Finally, our results confirm some of the findings in the neuroimaging literature, namely that individually, cortical thickness and brain volumes are associated with CA-IMT [24, 108, 159]. However, these associations are weak in comparison to that of FRS and do not add to that model's predictive power. Our findings also contrast with prior literature showing no association between CA-IMT and structural brain measures, including cortical thickness and brain volumes [3, 27], though it is possible that differences in the demographic makeup of the sample populations preclude direct comparisons.

Our failure to detect a reliable prediction of CA-IMT from the sole functional measure, resting-state FC, contrasts with recent work from our group showing reliable prediction of CA-IMT using task-based fMRI measures [63]. This contrast is particularly revealing. Resting-state FC is a passive measure reflecting global intrinsic brain networks [59, 137]. Thus, targeted recruitment of specific brain networks during stressful or engaging tasks is likely necessary in order to use such functional brain signals as a predictor of individual differences in CA-IMT [55]. Indeed, this type of task-based functional brain measure could boost the predictive power of FRS. However, there is a vast body of tasks that needs to be explored before this type of functional data can be incorporated into our stacking model. Furthermore not all task-based fMRI work has observed an association between CVD risk factors and neural activity patterns (e.g., there is no association between the cortico-limbic network activation during a social threat fMRI task and an individual's cardiometabolic risk [92]). Finally, it is possible that alternative resting-state FC analysis methods, including dynamic resting-state FC, graph analysis metrics (global efficiency, degree centrality), or

wavelet methods for determining connectivity, may provide different measures of the underlying resting hemodynamic response which may include signal for detecting individual differences in CA-IMT. However, a full survey of these different methods and their relationship to CA-IMT is itself an entire study in its own right, constituting a promising next step in investigation.

One interpretive consideration regarding the findings of this study centers on the particular model used and whether it is truly effective for using multimodal brain measures to predict CA-IMT. Notably, we first replicated the method exactly by successfully predicting brain age in our sample, demonstrating that the method works as expected. We also see above chance prediction performance from individual brain measures as well as FRS. Finally, we showed successful stacking with FRS, despite no performance improvements when we include brain measures.

Another important consideration when interpreting our findings relates to our sample population. It is possible that the study selection criteria may have restricted the range of subclinical CVD present in the sample, which could partly explain the failure of multimodal brain measures to predict CA-IMT. We note, however, that FRS explained a moderate amount of the variance in CA-IMT across individuals (see Figure 2.4). Notwithstanding, a useful future direction would be to replicate and extend our approach in a more diverse sample, spanning a range of preclinical and clinical phenotypes of CVD.

It is also possible that predictive performance in the present study was limited by the use of CA-IMT, which has been suggested to have limited performance in the prediction of clinical CVD outcomes [70, 97]. Nevertheless, evidence from intervention trials indicates that CA-IMT progression is an important outcome measure, especially for the detection of

early pathophysiological vascular changes [77]. Moreover, it has been noted that carotid ultrasound is feasible in nearly all persons, relatively inexpensive, and associated with the incident (future) development of atherosclerotic plaques [125, 158]. In these regards, CA-IMT is regarded as a surrogate measure of the atherosclerotic disease process that predicts later CVD events [6, 114, 125, 170]. Taken together, while CA-IMT has advantages as a subclinical CVD marker, it is possible that predictive performance from MRI measures could be improved by using other subclinical disease markers, such as coronary calcium scores or omnibus metrics based upon CA-IMT, such as arterial stiffness and endothelial function, which reflect vascular morphology and function [90].

The brain imaging modalities we used may have further constrained predictive performance, creating the possibility that other imaging modalities may capture brain features that are more reliably associated with subclinical CVD (e.g., arterial spin labeling for the assessment of cerebral blood flow and diffusion imaging for the assessment of white matter morphology) [82].

In addition, our cross-sectional findings do not rule out the possibility that baseline brain measures could forecast future (prospective) changes in disease endpoints, as has been found previously. Baseline amygdalar activity has been shown to predict future occurrence of CVD events [152], changes in visceral adipose tissue [81] as well as risk of Takotsubo syndrome [132]. Levels of stress reactivity within the rostromedial prefrontal cortex are also associated with future adverse CVD events [106].

2.5 Conclusion

In summary, the present cross-sectional human neuroimaging findings suggest that subclinical CVD reflected by CA-IMT does not reliably relate to a combined brain biomarker generated by stacking functional and structural features of the brain. Rather, CA-IMT predicted by FRS alone outperformed aggregate and individual MRI measures. In these regards, combining multimodal functional and structural brain measures by prediction stacking may not have utility in otherwise healthy midlife adults to characterize the neural correlates of subclinical CVD indexed by CA-IMT.

Chapter 3

niphlem: NeuroImaging-oriented Physiological Log Extraction for Modeling

Here we present *niphlem*, a pip-installable python toolbox that extracts physiological recordings from MRI sessions and performs quality control. The niphlem toolbox can generate multiple models of physiological noise to include as regressors in future GLM models from either ECG, pneumatic breathing belt or pulse-oximetry data. *Niphlem* operates in three distinct stages: preprocessing, data cleansing, and artifact model generation. Input files are BIDS consistent data files for either 1) ECG channels, 2) pulse oximetry, or 3) pneumatic respiration belt. Preprocessing may include data transformations, such as demean, and filtering. In the case of ECG input files, additional preprocessing steps may include combining signals from multiple channels. Data cleansing consists of detection of signal peaks (e.g., R peaks within the QRS waveform for ECG signals) and removal of artifacts in the detected peaks. Artifacts are identified through two one-sided Grubb's tests for outliers and subsequently corrected. Text files of the mean filtered timeseries and timepoints of the detected peaks are optionally saved as outputs. An html quality control report can

also be generated and saved that includes filtered signal statistics and visualization of data preprocessing and cleansing steps. Finally, *niphlem* generates two classes of artifact models: RETROICOR or variability models. RETROICOR is a phasic decomposition method that isolates the fourier series that best describes the spectral properties of the input signal. The variability model for low frequency signals (such as respiration from pneumatic belt and low-pass filtered pulse-oximetry) computes the combined respiration variance and response function. The variability model for high frequency signals (such as ECG or high-pass filtered pulse-oximetry) generates the heart-rate variance and cardiac response function. Through preprocessing, analysis and quality control of ECG data collected alongside resting-state fMRI, we show that *niphlem* is effective at identifying and removing physiological noise artifacts for future use in neuroimaging analyses.

3.1 Introduction

It is now well known that the hemodynamic blood oxygenation level dependent (BOLD) response that forms the basis of functional MRI (fMRI) includes both oxygenated changes related to neural activity, as well as blood flow changes related to local activity, but also contains artifacts arising from mechanical and physiological processes, such as heartbeats and respiration [69]. More specifically, approximately 50% of the variance in fMRI signals can be attributed to noise associated with these physiological processes, depending on the location within the brain and acquisition parameters [157]. There are also multiple mechanisms through which these cardiac and respiratory physiological processes can influence the BOLD fMRI signal, including pulsatile movement, field modulations as well as direct changes of blood oxygenation [15, 18, 29, 69, 99]. This uncertainty in what is signal versus what is noise in the BOLD response can have troubling implications, particularly for functional connectivity analyses or when physiological responses can be phase-locked to task events. To overcome this uncertainty, it is important to understand how these physiological processes affect the hemodynamic BOLD response so that we can account for these sources of noise in analyses of neural data. Failure to do so could result in erroneous interpretation of results as attributed to neural processes, when in actuality a large portion of the variance could be due to physiologic artifact.

Given this signal-to-noise uncertainty, there has been substantial work focused on both characterizing and building analytical tools to account for these physiological artifacts [14, 15, 28, 29, 44, 69, 73]. For example, modeling and incorporating the phasic fluctuations of cardiac and respiratory signals [28, 69] as well as information about variations in cardiac

and respiratory characteristics (e.g., heart rate and breath volume), into the design matrix of a GLM can improve the clarity of the underlying neural processes by removing portions of variance associated with physiological artifacts [14, 15] (see [22, 95] for reviews). Methods like cardiac-gating [71] have also been applied to account for physiological, in this case cardiac, artifacts in diffusion and cerebral blood flow measures, but these sorts of time-locked acquisition approaches have limited effectiveness in contexts where task-based activation are of interest, as is the case with fMRI.

With these limitations, there has been renewed interest in modeling and accounting for physiological signals in fMRI. This is particularly important for fields like health neuroscience [52], for example neurocardiology [142], where these cardiorespiratory signals can be both artifact and signal. This mixing of artifact and signal only emphasizes the need for adequate removal of physiological artifacts from neural signals. In such cases, the physiological signals themselves may also need to be cleaned before use in analyses, something that most current toolboxes for modeling physiological artifacts do not do.

With this in mind, we developed the NeuroImaging-oriented Physiological Log Extraction for Modeling (*niphlem*) toolbox. *Niphlem* is a pip-installable python toolbox that extracts physiological recordings from MRI sessions, performs quality control and estimates the signal phases for future use as covariates. *Niphlem* can generate multiple models of physiological noise to include as regressors in future GLM models from either ECG, pneumatic breathing belt or pulse-oximetry data. The toolbox is the python version of the original PhLEM toolbox written in Matlab (and no longer supported). The goal of *niphlem* is to be simple and flexible to use and as open as possible. In this paper we describe the toolbox functions in detail and demonstrate example usage with cardiac and respiration data collected in concert

with resting-state fMRI data. Further information (including API references and tutorials) is available on the *niphlem* website and github repository.

3.2 Methods

3.2.1 Toolbox installation

Niphlem is installable through PyPI as follows:

```
pip install -U niphlem
```

The toolbox's current dependencies include `matplotlib`, `numpy`, `outlier_utils`, `pandas`, `scikit-learn` and `scipy`, which are installed if necessary during niphlem installation.

3.2.2 Toolbox functions

Niphlem operates in three distinct stages: preprocessing, data cleansing, and artifact model generation. Input signals are BIDS consistent data files from electrocardiogram (ECG), pulse-oximetry, or pneumatic respiration belt.

3.2.2.1 Preprocessing

Quality control reports can be generated that conveniently implement the preprocessing and data cleansing steps, though users are also able to separately perform these steps using individual functions. Preprocessing of the physiological data signal includes data transformation steps, such as demean, and filtering. In the case of ECG input files, additional preprocessing steps may include combining signals from multiple channels. Data cleansing consists of detection of signal peaks (e.g., R peaks within the QRS waveform for ECG signals) and removal

of artifacts in the detected peaks. Peak detection uses Eli Billauer's MATLAB algorithm translated into python. Artifacts are identified through two one-sided Grubb's tests for outliers and subsequently corrected, by either adding a missed peak or removing an incorrect peak. The html quality control report contains relevant statistics and visualizations for the preprocessed and cleansed physiological data signal. In addition, the report function returns a data object containing the preprocessed and cleansed physiological signal as well as the timepoints of peaks within the signal. The report and data objects can be optionally saved at the users discretion.

Niphlem's function `make_ecg_report` takes the ECG signal (of shape n_samples x n_channels) and signal-related parameters as inputs and returns the report and data objects described above. The input parameters include: the signal sampling rate (Hz), the minimum separation (in physiological recording units) between signal peaks, the relative height of signal peaks, the order of Fourier series expansion, time window (s), the column in the input ECG signal to be used as a ground channel, high-pass and low-pass filtering frequencies (Hz). For a detailed example of how to use the report functions, we recommend viewing the tutorials on `coaxlab.github.io/niphlem`.

3.2.2.2 Noise models

Niphlem currently generates two classes of artifact models: RETROICOR [69] or variability models [14, 15, 28], although the open-source structure of *niphlem* makes it possible to incorporate newer modeling approaches as they arise.

3.2.2.2.1 RETROICOR

RETROICOR stands for Retrospective Image Correction and is a phasic decomposition

method that isolates the Fourier series that best describes the spectral properties of the input signal [69]. For physiological signals used in fMRI analyses, RETROICOR calculates the Fourier series expansion using phases from cardiac and respiratory cycles.

The algorithm is as follows (see Figure 3.1 for a graphical representation):

1. Identify the peaks in the physiological data signal. For ECG signals, the peak corresponds to the R component of the QRS complex. For pneumatic belt signals, the peak expansion of the diaphragm. And for pulse-oximetry signals, the maxima in the local blood oxygenation.

2. Estimation of a phase time to be between 0 and 2π between consecutive time peaks t_1 and t_2, i.e., as having full phase cycles: $\phi(t) = \frac{2\pi(t-t_1)}{(t_2-t_1)}$.

3. Computation of sines and cosines of these phases up to a specified order, k, i.e., $[\sin(k(t)), \cos(k(t))]$, with $k = 1, 2, ...$

4. Downsampling each of these terms to match the scanner time resolution.

These steps allow us to obtain a series of phase regressors that we can then use in future analyses, e.g., fMRI models, to account for the physiological signal.

Niphlem implements a class called `RetroicorPhysio`, that preprocesses the physiological signal (transforms and filters) and implements this algorithm to generate RETROICOR cardiac and respiration regressors. The class takes a number of signal-related parameters as inputs: the physiological signal sampling rate (Hz), TR (s), the minimum separation (in physiological recording units) between signal peaks, the relative height of signal peaks, the order of Fourier series expansion, time window (s), preprocessing options (demean, z-score,

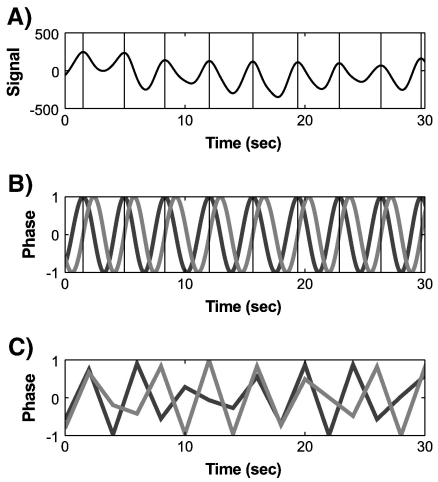

Figure 3.1: RETROICOR algorithm procedure (reproduced with permission from Verstynen and Deshpande, 2011 [163]). A) Individual events in the signal were identified using a peak detection procedure (vertical lines). B) Samples between each event were recategorized to being between 0 and 2π. The cumulative summed phase time served as an estimate of the primary Fourier series for the signal of interest. The sine (gray lines) and cosine (black lines) of this phase were then computed. C) These phase regressors were down-sampled to the TR interval and saved as covariate regressor terms in the GLM.

absolute value), high-pass and low-pass filtering frequencies (Hz), channel options (i.e., how to handle multiple signal input channels), and whether to implement peak outlier detection and correction. For a detailed example of how to use this class, we recommend viewing the tutorials on `coaxlab.github.io/niphlem`.

3.2.2.2.2 Variability models

Niphlem can also generate nuisance regressors for variation in respiration rate/volume and heart rate. The variability model for low frequency signals (such as respiration from pneumatic belt and low-pass filtered pulse-oximetry) computes the combined respiration variance and response function [15]. The algorithm for variability artifacts from respiration rate/volume is as follows (see Figure 3.2 for a graphical representation):

1. Computation of the standard deviation of the signal within a time window (usually of length 3*TR) centered at each TR [28]. This yields a time series at the scanner acquisition time resolution.

2. Z-score normalization.

3. Convolution with the respiratory response function ($RRF(t)$), where: $RRF(t) = 0.6t^{2.1}e^{-t/1.6} - 0.0023t^{3.54}e{-}^{t/4.25}$.

The *niphlem* class `RVPhysio` preprocesses the physiological data signal (transforms and filters) and implements this algorithm to generate respiration rate variability regressors. The class takes a number of signal-related parameters as inputs: the physiological signal sampling rate (Hz), TR (s), time window (s), preprocessing options (demean, z-score, absolute value), high-pass and low-pass filtering frequencies (Hz), and channel options (i.e., how to handle multiple signal input channels).

The variability model for high frequency signals (such as ECG or high-pass filtered pulse-oximetry) generates the heart-rate variance and cardiac response function [28]. The algorithm for variability artifacts from heart rate is as follows (see Figure 3.3 for a graphical representation):

1. Computation of the average deviation in inter-event interval (i.e., ms between R-components of the QRS complex), per second, within a time window (usually of length 3*TR) centered at each TR [28]. This yields a time series at the scanner acquisition time resolution.

2. Z-score normalization.

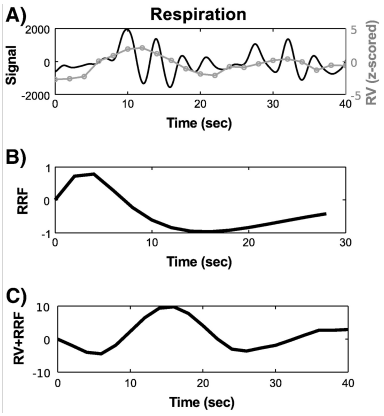

Figure 3.2: Variations in breathing rate/volume procedure (reproduced with permission from Verstynen and Deshpande, 2011 [163]). A) Respiration variance (RV) was calculated by taking the standard deviation of the respiration signal (black line; either from the pneumatic belt or pulse-oximetry) between each successive TR (gray line). B) The respiration response function (RRF) was simulated using parameters derived elsewhere (Birn et al., 2008; Eq. (3)). C) The RV was convolved with the RRF to produce a model regressor.

3. Convolution with the respiratory response function ($CRF(t)$), where: $CRF(t) = 0.6t^{2.7}e^{-t/1.6} - \frac{16}{\sqrt{18\pi}}e^{-\frac{1}{2}\frac{(t-12)^2}{9}}$.

The *niphlem* class `HVPhysio` preprocesses the physiological data signal (transforms and filters) and implements this algorithm to generate heart rate variability regressors. The class takes a number of signal-related parameters as inputs: the physiological signal sampling rate (Hz), TR (s), the minimum separation (in physiological recording units) between signal peaks, the relative height of signal peaks, time window (s), preprocessing options (demean, z-score, absolute value), high-pass and low-pass filtering frequencies (Hz), channel options (i.e., how to handle multiple signal input channels), and whether to implement peak outlier detection and correction.

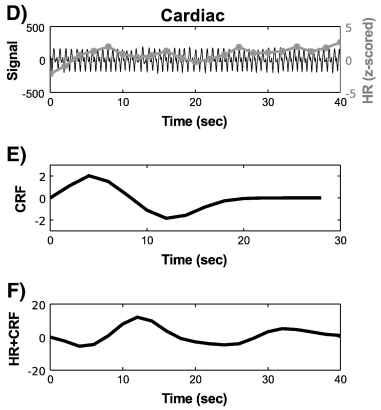

Figure 3.3: Variations in heart rate procedure (reproduced with permission from Verstynen and Deshpande, 2011 [163]). D) Heart-beat variation (HR; gray line) was calculated as the average deviation in inter-event interval for pulsations between each TR (black line). E) The cardiac response function (CRF) was simulated according to Chang et al., 2009; Eq. (5). F) The HR was then convolved with the CRF to produce a model regressor.

3.2.3 Data

In the test analysis below, we draw from a resting-state data set collected from one healthy participant (white male, age 43). Functional blood oxygenation level-dependent images were collected on a Siemens Prisma 3T scanner, equipped with a 64-channel head coil. Over a 8 minute 54 second period with eyes open, functional images were acquired with acquisition parameters as follows: 2mm iso voxels, FOV = 212x212mm, TR = 1500ms, TE = 30ms, FA = 79°, multiband acceleration factor = 4. Sixty-eight interleaved slices (2mm thickness, no gap) in the ascending direction were obtained for each of 353 volumes (with three initial volumes discarded to allow for magnetic equilibration). Electrocardiogram (ECG) data were collected concurrently during functional MRI (fMRI) scans at a sampling rate of 400 Hz using the Siemens physiological monitoring unit's standard configuration. Pneumatic belt

data were also collected concurrently at a sampling rate of 400 Hz.

3.2.4 Analysis

To showcase *niphlem*'s functionality, we performed quality control and generated RETROICOR regressors for a single ECG and pneumatic belt signal collected alongside a resting-state fMRI scan. ECG preprocessing steps are as follows: 1) subtraction of ground ECG channel from remaining channels, 2) demean channels, 3) Butterworth bandpass filtering (0.6 Hz - 5 Hz), 4) average channels. Additional parameters for the ECG quality control report include a minimum peak separation of 200 and a relative peak height of 0.75. Second order cardiac RETROICOR regressors were generated. Pneumatic belt preprocessing steps included demeaning and Butterworth bandpass filtering (0.1 Hz - 0.5 Hz). Additional parameters for the pneumatic belt quality control report include a minimum peak separation of 800 and a relative peak height of 0.5. Second order respiration RETROICOR regressors were generated. Nilearn was used to generate design matrices and run first level GLM analyses for each of the cardiac and respiration signals [1]. Specifically, the design matrices included an intercept term, three translational motion parameters, three rotational motion parameters as well as the four (two sine and two cosine) cardiac or respiration RETROICOR regressors. The first level GLMs fit these design matrices to our resting-state fMRI data on a voxelwise basis, across the whole brain, to estimate the cardiac and respiration physiological artifact response, respectively.

3.3 Results

3.3.1 Physiological signal curation

We used *niphlem*'s quality control function to preprocess and cleanse the ECG signal. The full report is included as supplementary material. Figure 3.4 is an excerpt of the graphs generated during the quality control process. These graphs draw from raw, or unfiltered, ECG data as well as the filtered ECG data. Panel A shows a portion of the raw, or unfiltered ECG signal in blue as well as the transformed, or filtered ECG signal in orange. Transformation includes the ECG preprocessing steps described in section 3.2.4 (ground subtraction, demeaning, bandpass filtering, averaging). Panel B shows the power spectrum for the unfiltered and filtered ECG signal. It is clear that the power of the signal drops off above 5 Hz, showing the effect of filtering. Panel C shows a portion of the filtered ECG signal with red x's marking the location of identified peaks of the signal, i.e., the R peak of the QRS complex. Panel D shows the average QRS waveform over the entire ECG signal timeseries, as well as the average heart rate of the timeseries. We can see that the shape of the QRS waveform is as expected from an ECG signal. Panel E shows the RR interval (difference between successive R peaks) histogram and statistics, according to the identified peaks of the filtered ECG signal. Panel F shows the instantaneous heart rate of the ECG signal timeseries, where the instantaneous heart rate is calculated as follows: instantaneous HR $= \frac{\text{sample frequency}}{\text{RR interval}} * 60$.

Figure 3.5 depicts another set of graphs from *niphlem*'s quality control report that compares ECG signal characteristics before and after anomaly correction. Panels A and B show the average QRS waveform across the filtered and corrected timeseries respectively. While

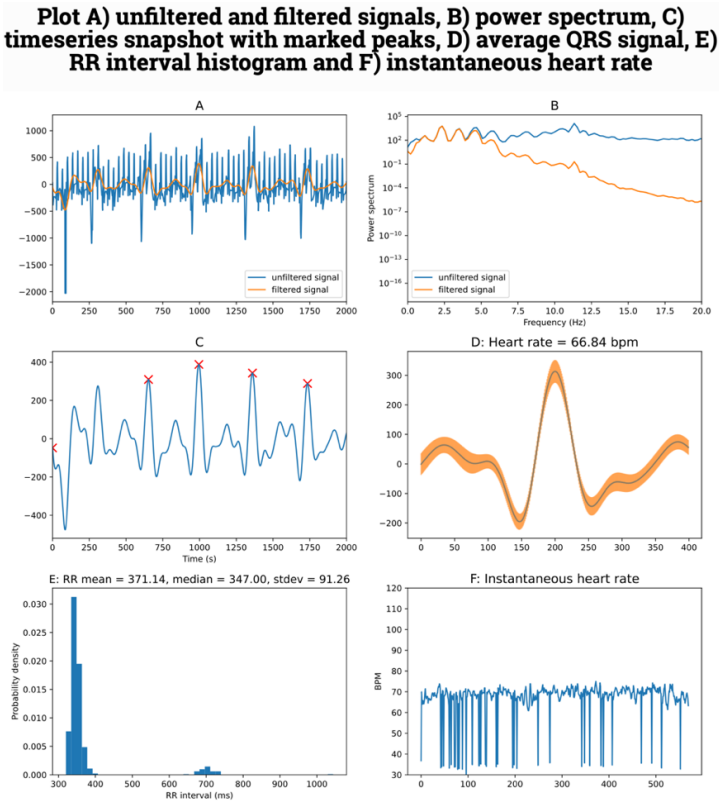

Figure 3.4: Excerpt from ECG quality control report demonstrating filtering and peak detection steps. A) Unfiltered and filtered ECG signal (first 2000 msec). B) Power spectrum of ECG signal. C) ECG signal snapshot (first 2000 msec) with identified peaks. D) Average QRS waveform across the entire ECG signal and average heart rate. E) ECG RR interval histogram. F) Calculated instantaneous heart rate across ECG signal.

there aren't visually discernible changes in the shape of the waveform, the corrected average heart rate increases by a few beats per minute. Panels C and D show the RR interval histograms before and after anomaly correction. The set of RR intervals around 700ms in the filtered, but uncorrected ECG data (panel C) are due to peaks that were not identified. *Niphlem*'s anomaly correction procedure identified these missed peaks and thus the 700ms RR interval outliers are not present in the histogram in panel D. Panels E and F show the

instantaneous heart rate before and after anomaly correction. The low instantaneous heart rate spikes in panel E correspond to the missed peaks and the 700ms RR intervals and constitute artifacts. These artifacts are corrected in panel F and the resultant instantaneous heart rate is much smoother.

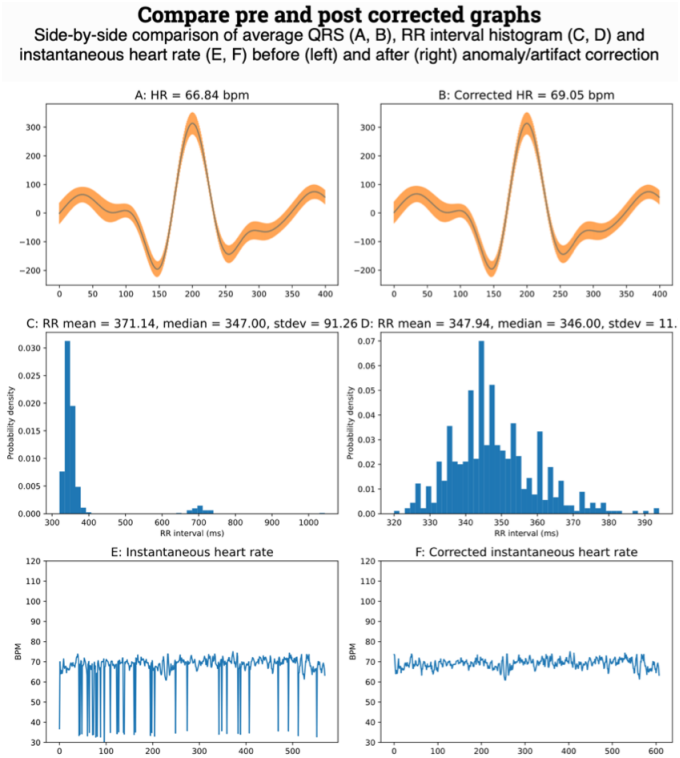

Figure 3.5: Excerpt from ECG quality control report demonstrating comparison of ECG signal and measures before (left) and after (right) anomaly correction. A, B) Average QRS waveform across the entire ECG signal timeseries and average heart rate. C, D) ECG RR interval histogram. E, F) Calculated instantaneous heart rate across ECG signal.

3.3.2 Artifact detection in voxelwise responses

We next used *niphlem*'s `RetroicorPhysio` class to generate second order cardiac RETROICOR regressors. We generated a design matrix that included an intercept term, six motion regressors (three translational and three rotational) and the four cardiac RETROICOR regressors. Using Nilearn [1], we performed a first level GLM analysis using this design matrix on our resting-state fMRI data. Figure 3.6 shows the design matrix in panel A and the recovered artifact effects, estimated from the average regression parameters for the RETROICOR noise terms in the GLM. Regions in red indicate areas with increased intensity of activation in response to cardiac signals. These are located in regions near the large vessels of the cortex as well as the edges of the brain, both are areas expected to have increased presence of cardiac noise.

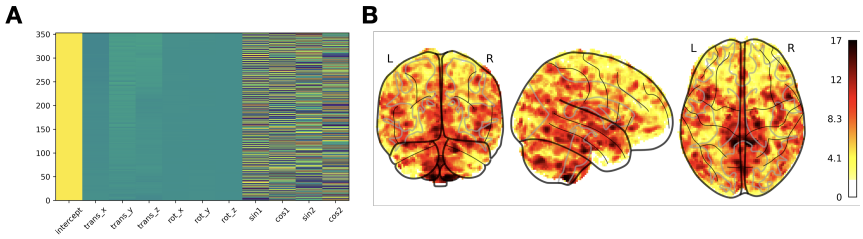

Figure 3.6: A) Design matrix generated using Nilearn with RETROICOR regressors for ECG included from *niphlem* output. B) First-level GLM results generated using Nilearn applied to resting-state fMRI with design matrix in panel A.

We next performed preprocessing (demeaning and bandpass filtering) and data cleansing steps on the pneumatic belt signal using *niphlem*'s quality control function for respiration. The full report is included as supplementary material. Figure 3.7 shows the instantaneous respiration rate before (panel A) and after (panel B) *niphlem*'s anomaly correction procedure.

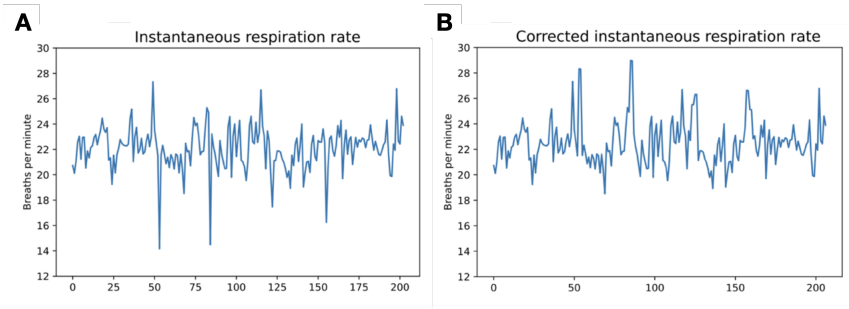

Figure 3.7: A) Instantaneous respiration rate across the filtered pneumatic belt signal time-series. B) Instantaneous respiration rate across the filtered and corrected pneumatic belt signal.

Using second order respiration RETROICOR regressors generated through *niphlem*, we created the design matrix shown in Figure 3.8, panel A, which includes an intercept term, motion regressors and respiration regressors. We again used this design matrix in a first level GLM analysis. Results are shown on the brain in Figure 3.8, panel B. Compared to the cardiac GLM results (Figure 3.7), we see greater activation in frontal and superior regions of the brain, where variation in frontal distortion fields (from sinus cavities) due to head movements associated with breathing are expected to be present.

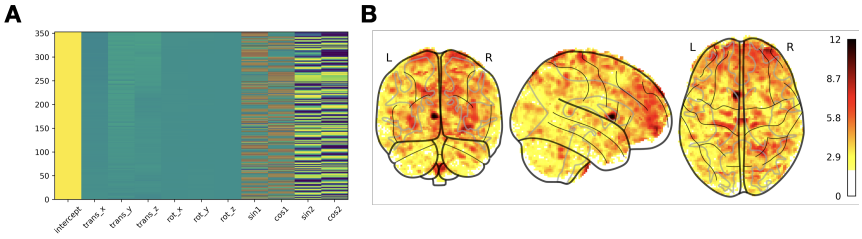

Figure 3.8: A) Design matrix generated using Nilearn with RETROICOR regressors for pneumatic belt included from *niphlem* output. B) First-level GLM results generated using Nilearn applied to resting-state fMRI with design matrix in panel A.

3.4 Discussion

Here we have described and demonstrated the functionality of *niphlem*, including preprocessing and cleansing of input physiological signals, as well as generating covariates based on physiological signals, that can be used to decontaminate task or network related signals from the hemodynamic BOLD response. We show the effect of preprocessing and cleansing of an ECG signal as part of *niphlem*'s quality control pipeline. We also use *niphlem*-generated physiological noise regressors (from cardiac and respiration sources separately) in a first level GLM analysis applied to resting-state fMRI data and see expected activation in areas of the brain affected by cardiac pulsatility and head motion due to respiration. The ultimate goal of these functions is to facilitate the use of the cleaned physiological signals themselves, with a degree of certainty about their quality, and to incorporate them into neuroimaging analyses, as is standard in the field.

There is increasing interest in studying the bidirectional brain-body relationships that are the foundation of the field of health neuroscience [52]. These relationships include brain-behavior and brain-physiology connections, which emphasize the necessity of removing non-neural confounds that are the result of physiological processes. The fields of health neuroscience and neurocardiology must account for these artifacts in order to use the BOLD response for further study. More generally, any task-based and functional connectivity driven analyses of fMRI signal cannot rule out phase-locking of physiological artifacts, which risks conflating noise with true signal.

Mass univariate neuroimaging analysis methods, such as GLM, connectivity based approaches, as well as multivariate analyses for activation estimates require the neural signal

to first be preprocessed in part to remove the influence of physiological artifacts. This is the case for both task-based fMRI and resting-state fMRI data. For task fMRI, it is not sufficient to assume that averaging across blocks or trials will eliminate the effects of noise, since they could be due to motion, heart rate or breathing changes that are associated with the task. For estimates of functional connectivity from resting-state fMRI, which rely on temporal correlation of signal fluctuations across brain regions, connectivity could be due to the influence of physiological noise on multiple brain regions simultaneously, rather than coordinated activation of brain regions [156]. RETROICOR and variability methods are popular model-based choices for generating covariates that can be included as additional variables to account for influence of physiological noise, and provide more certainty that the results of fMRI analyses are not in fact due to noise artifacts.

Niphlem was built to accomplish a few specific goals, including preprocessing of physiological signals collected during MRI sessions and generation of noise models. The toolbox is a good option for automated cleansing of ECG, pneumatic belt and pulse-oximetry signals - removing artifacts that do not truly represent the underlying heart rate or respiration rate. Helpful quality control reports can be optionally generated that summarize the preprocessing and data cleansing steps for a given input signal. Finally, *niphlem* is also highly flexible, providing the user with the ability to modify toolbox options, steps and outputs depending on individual needs.

There are, however, some clear limitations of the current version of *niphlem* that are worth discussing. First, and most obviously, the toolbox does not provide data-driven noise correction [22]. While these approaches can be helpful in certain circumstances, especially when physiological data is not collected in concert with neuroimaging data, they are beyond

the scope of the toolbox. Second, we focused here on ensuring that *niphlem* is flexible to allow for broad usage according to individual users' needs. However, taking advantage of *niphlem*'s flexibility necessitates some baseline knowledge of python on the part of the user, to be able to manipulate the inputs and outputs as desired. Additionally, unlike comprehensive toolboxes such as SPM and FSL, *niphlem* does not have a graphical user interface that would provide an option for interfacing with the code. We believe this acts as a positive in terms of the flexibility of the toolbox if users have a certain level of python knowledge as well as in terms of the toolbox not acting like a black box. However, this same flexibility could be an obstacle to overcome, for instance if inclusion in existing automated pipelines is the goal. Another limitation of *niphlem* is the lack of automated visualization of the entire signal for visual quality assessment, as well as the absence of options for manual user modifications/changes to certain toolbox functions, e.g., the ability for users to manually select peaks to add or remove from a signal. Though it could be argued that this is outside the goals of our toolbox. In future iterations of *niphlem*, we hope to include more sophisticated anomaly correction algorithms for detected peaks. It could also be beneficial to add functionality that would calculate some popular physiological characteristics, for instance HRV. Although, by being an open-source toolbox, each of these limitations can be overcome with greater community involvement in developing and expanding *niphlem*.

3.5 Conclusion

Niphlem is a flexible python toolbox that can be used to evaluate the quality and effectively clean physiological signals from ECG, pneumatic belt and pulse-oximetry collected during

MRI sessions for further analyses of the signals themselves or for use in removing noise artifacts in future neuroimaging analyses. The toolbox also contains functionality to generate model-based covariates of physiological noise artifacts.

Chapter 4

Cortical and Subcortical Brain Networks Predict Prevailing Heart Period

Resting heart rate is a critical risk factor for cardiovascular disease (CVD) for individuals with and without pre-existing conditions. While the brainstem's autonomic control over heart rate is well established, there exists a need to investigate the role of higher-level cortical and subcortical brain regions and the mechanisms by which they interact with regulatory cardiac control. The present study sought to characterize the brain networks that predict variation in prevailing heart rate within individuals. To do so, we used machine learning approaches designed for handling complex, high-dimensional datasets, to predict instantaneous heart period (the inter-heartbeat-interval) from temporal variation in whole brain hemodynamic signals measured using fMRI. Task-based and resting-state fMRI, as well as peripheral physiological recordings, were used from two datasets that included extensive repeated measurements within individuals. We implemented a LASSO-PCA continuous regression model that predicted instantaneous heart period from the hemodynamic BOLD signal. Our models reliably predicted instantaneous heart period from whole brain fMRI data both within and

across individuals, though prediction accuracies were marginally lower when we tested generalizability across participants. We found that a network of cortical and subcortical brain regions work in concert to modulate regulatory cardiac control, as indexed by heart period. This work adds to an increasing body of work that investigates brain-heart connections and constitutes an incremental step towards developing clinically-applicable biomarkers of brain contributions to CVD risk.

4.1 Introduction

Resting heart rate (HR) is not only an indicator of overall physical health, as measured by all-cause mortality, but it is specifically a notable risk factor for cardiovascular disease in individuals with and without pre-existing cardiovascular disease (CVD; [16, 57, 116, 124]). High resting HR has been shown to be associated with progression of coronary artery atherosclerosis and the occurrence of myocardial ischemia and arrhythmias as well as being detrimental to left ventricular function [17, 39, 57, 80, 116, 124]). Indeed, health risks seem to increase steadily as HR increases [57]. Conversely, reduction of resting HR has long been associated with the prevention of activity related angina and ischemia [57]. High resting HR is often comorbid in individuals with other cardiometabolic risk factors, including hypertension, blood lipid and glucose level, and overweight BMI [54, 115]. However, it is nonetheless an independent risk factor. A large scale, long-term follow up epidemiological study found high resting HR to be a significant risk factor for all-cause mortality as well as death from acute myocardial infarction, after adjusting for possible confounds such as age, BMI, systolic BP, diabetes diagnosis and level of physical activity [57, 85].

Evidence from animal studies and human lesion studies have shown conclusively that HR is under autonomic control, with the brainstem performing extensive regulation [37, 72, 113, 155, 162]. This brain-heart link has been more recently validated by human neuroimaging studies [36, 37]. This link also extends further "up" the brain, to evolutionarily newer brain regions like the telencephelon (i.e., neocortex), which seems to play a particularly critical role in stress-related modulation of HR [67], in which the cortex appears to exert control, either directly or indirectly on the autonomic nervous system (specifically, sympathetic activation

followed by parasympathetic inhibition), elevating HR and other peripheral physiological responses in response to both physical and psychological stress [19, 25, 88, 150]. Indeed, the role of psychological stress in modulating cardiac function provides a particularly clear indication of the role that cortical function has on HR control [42, 50, 67, 91, 153]. Given what we know about resting HR as a risk factor for CVD, this offers an opportunity to expand our knowledge further, delving into questions about the role of higher-level cortical and subcortical brain regions and the mechanisms by which they interact with and regulate the brainstem's autonomic control over HR.

Here we sought to characterize the brain networks that predict variation in prevailing HR within individuals. To do so, we used machine learning approaches designed for handling complex, high-dimensional datasets, to predict instantaneous heart period (the inter-heartbeat-interval) from temporal variation in whole brain hemodynamic signals measured using fMRI. Our hypotheses were twofold. First, we hypothesized that our model would reliably predict modulation of heart period from hemodynamic responses in the brain within individuals. Second, we hypothesized that the brain regions that are most important for this prediction would encompass part or all of the visceral control circuits.

4.2 Methods

4.2.1 Human QA dataset

4.2.1.1 Participants

Neuroimaging and cardiovascular data were collected from one healthy participant (white male, age 43) at 14 repeated scan sessions over a period of 20 weeks. Three fMRI scans with concurrent electrocardiogram (ECG) and pneumatic belt physiological signals were collected at each session, along with a structural MRI scan, for a total of 42 runs. The participant provided informed consent to complete the study, which was approved by the Carnegie Mellon University (Pittsburgh, PA) Institutional Review Board.

4.2.1.2 MRI data acquisition and processing

4.2.1.2.1 Acquisition

Functional blood oxygenation level-dependent images were collected on a Siemens Prisma 3 Tesla scanner, equipped with a 64-channel head coil. Over a 8 minute 54 second period with eyes open, resting-state and task dependent functional images were acquired with acquisition parameters as follows: 2mm iso voxels, FOV = 212x212mm, TR = 1500ms, TE = 30ms, FA = 79°, multiband acceleration factor = 4. Sixty-eight interleaved slices (2mm thickness, no gap) in the ascending direction were obtained for each of 353 volumes (with three initial volumes discarded to allow for magnetic equilibration). T1-weighted neuroanatomical magnetization prepared rapid gradient echo (MPRAGE) images were collected in 208 slices (1mm thickness, no gap) over a 7 minute 58 second period with acquisition parameters as follows: 1mm iso

voxels, FOV = 256x256mm, TR = 2300ms, TE = 2.03ms, TI = 900ms, FA = 9°.

4.2.1.2.2 Preprocessing

Preprocessing was performed using fMRIPrep version 20.2.7 ([53]; RRID:SCR_016216). Eight T1-weighted images collected across the 14 sessions were combined into one average T1-weighted reference map. Anatomical and functional images were normalized to the ICBM 152 Nonlinear Asymmetrical template version 2009c ([56], RRID:SCR_008796; TemplateFlow ID: MNI152NLin2009cAsym).

4.2.1.2.3 Gray Matter (GM) mask

Using the GM tissue probability reference image in MNI152NLin2009cAsym standard space output from fMRIPrep, we generated a binary mask (thresholded at probability >0.2) to limit our analysis to GM voxels.

4.2.1.3 Heart period from ECG

ECG data were collected concurrently during functional MRI (fMRI) scans at a sampling rate of 400 Hz using the Siemens physiological monitoring unit's standard configuration. Data were processed using niphlem and included the following steps: 1) subtraction of ground ECG channel from remaining channels, 2) demean channels, 3) bandpass filtering (0.6 Hz - 5 Hz), 4) average channels. Signal peaks were identified (specifically, the R peaks within the QRS waveform) with subsequent detection of artifacts through two one-sided Grubb's tests for outliers and correction. The processed ECG signal peaks were then downsampled to match the fMRI TR, to allow for a one-to-one correspondence of our X and y data for our prediction models.

It is known that heart rate behaves non-linearly in many contexts, especially with re-

spect to underlying autonomic input [12, 62]. An alternative measure is heart period (the interbeat interval, or the time between ECG signal peaks), which is the inverse of heart rate. While both measures are controlled in part by autonomic inputs, there exists a more linear relationship between autonomic control and heart period, when compared to heart rate [12, 62]. Thus heart rate and heart period are not interchangeable with respect to autonomic control. For this reason, we use heart period as our target variable.

4.2.1.4 Analysis

Figure 4.1 shows the structure of our analysis pipeline, which involves three stages: preprocessing, denoising, and model analysis. Preprocessing was performed using fMRIPrep and *niphlem* for the fMRI and physiological data, respectively as detailed in sections 4.2.1.2 and 4.2.1.3.

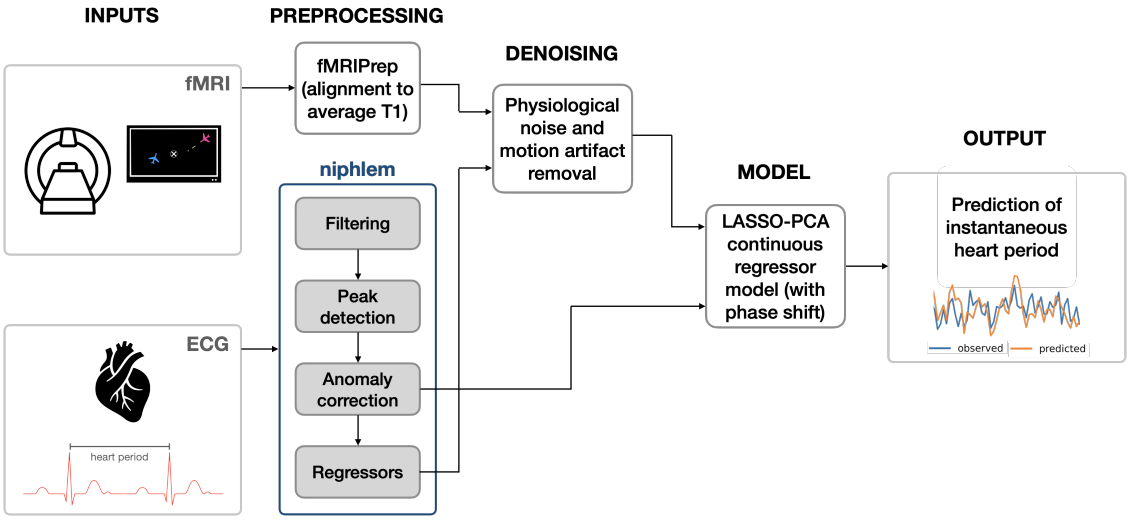

Figure 4.1: Analysis pipeline schematic.

Denoising constituted removal of physiological noise from the hemodynamic signal itself.

To do so, we used *niphlem* to generate variability regressors from the cardiac and respiratory response functions [15, 28]. We then conducted a GLM of these variability regressors onto our fMRI signal to capture the artifact components from mechanical physiological noise. We removed these artifacts from the fMRI signal by isolating the GLM residuals to use for further analysis.

The next stage of our pipeline was a leave-one-run-out nested cross-validated LASSO-PCA model that took the GLM residuals as input and predicted instantaneous heart period. We set up multiple models (13 total), each of which predicted instantaneous heart period from fMRI timeseries data at time points ranging from t-3 seconds to t+15 seconds (shifting by one TR at a time, i.e., 1.5 seconds). This range of lag time shifts between the fMRI signal and instantaneous heart period ensures that we take into account the HRF delay (6-8 seconds) inherent with BOLD data. See Figure 4.2 for a graphical illustration of the lag time shifts to isolate the desired drive signal. Thus, for each run across sessions, instantaneous heart period was predicted at every TR from GM voxels of the fMRI signal. First, as part of the PCA step, singular value decomposition was performed to reduce the dimensionality of the predictor matrix. This also addresses the issue of multicollinearity across voxels. The inner loop then performed five-fold cross-validation on the training runs to optimize lambda (λ), the shrinkage parameter that controls the L1 penalty in LASSO, using a sequence of 100 λ values. Finally, the outer leave-one-run-out cross validation loop performed the entire LASSO-PCA algorithm using this optimal lambda value. We repeated this analysis using the preprocessed timeseries before removal of artifacts for comparison.

Overall model performance was evaluated using prediction accuracy on a hold-out test set. This was done by comparing predicted heart period and observed heart period using

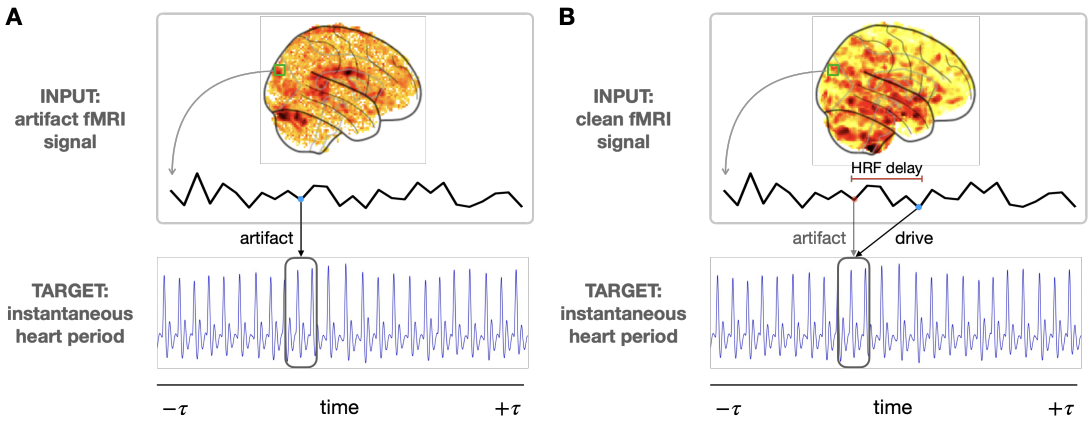

Figure 4.2: A) Prediction of heart period from physiological noise component of fMRI signal. B) Prediction of heart period after removing artifacts from the fMRI signal and accounting for the HRF delay.

fMRI runs that were not included in the model training. Model performance was measured using Pearson correlation coefficient, r.

In order to visualize which brain regions were contributing the most to the prediction of heart period, we projected the voxelwise decoding maps into approximations of their encoding representations [74]. For this LASSO coefficients were extracted from each model run and multiplied by the V matrix (from the singular value decomposition $X = USV^T$) to generate weights in feature space. These weights were then multiplied by the covariance matrix of X (our voxel data) to convert to encoding weights [74].

To minimize computation time and excessive memory requirements of our analysis pipeline with large datasets, we adopted a modular approach that takes advantage of model averaging [78]. We trained individual LASSO-PCA models for each run and extracted the associated weights. For the outer leave-one-out cross-validation loop, we averaged these weights from the $n-1$ trained models, using the mean voxel decoding weights, to test our model's hold-out

prediction accuracy.

We performed a one-sample t-test on the encoding weights for lag time shift +7.5 seconds for each run with a false discovery rate (FDR) <0.00005 to generate a statistically thresholded weight map corresponding to the Human QA dataset participant. Visualization of the participant's projected weights on the 3D brain was performed using Surf Ice.

4.2.1.5 Power analysis

We conducted a power analysis to test the number of runs needed for reliable prediction of heart period from fMRI data, using sample sizes n = 2, 4, 8, 10, 16, 20, and 30. For each sample size, we randomly selected n runs from the 42 total runs to use in our analysis. Working with the cleaned fMRI data at lag time shift +7.5 seconds, we trained a LASSO-PCA model on each run then used a leave-one-out cross-validation scheme to test each model on the average weights from the $n-1$ trained models, as described in section 4.2.1.4. This procedure was repeated 40 times for each sample size. Hold-out test set prediction accuracy was evaluated using Pearson correlation coefficient and the mean r value and 95% confidence interval was calculated for each sample size.

4.2.2 Natural Scenes Dataset (NSD)

4.2.2.1 Participants

Neuroimaging and cardiovascular data from eight healthy participants (six females; aged 19–32 years) from the NSD were used for Experiment 2. A detailed description of the Natural Scenes Dataset (NSD) is provided elsewhere [4]. Physiological data was only available for a subset of scan sessions: four participants had data from ten scan sessions (S1, S2, S5, S7;

nsd21-30), two participants had data from nine scan sessions (S3, S6; nsd21-29) and two participants had data from seven scan sessions (S4, S8; nsd21-27). Each session contained 14 functional runs (12 task and two resting-state scans). The total number of runs for each participant are as follows: S1 n = 140, S2 n = 140, S3 n = 126, S4 n = 93, S5 n = 140, S6 n = 126, S7 n = 139, and S8 n = 84.

4.2.2.2 Heart period from pulse-oximetry

Physiological data from pulse-oximetry and pneumatic belt were used to record cardiac and respiration events respectively. *Niphlem* was used as described in section 4.2.1.2 to extract instantaneous heart period and generate cardiac and respiratory variability regressors. In this case however, heart period was derived from the pulse-oximetry data.

Runs with noisy or interrupted pulse-oximetry data that prevented recovery of heart period were excluded from analysis: five runs for S4, one run for S7, and 14 runs (one entire session) for S8.

4.2.2.3 MRI data acquisition and processing

4.2.2.3.1 Acquisition

FMRI data in the NSD were collected at 7T using a whole-brain, 1.8mm, 1.6 second, gradient-echo, echo-planar imaging (EPI) pulse sequence. Further details can be found in [4].

4.2.2.3.2 Preprocessing

We used the 1.8mm volume preparation of the preprocessed NSD timeseries data. FMRI preprocessing involved two steps. First, a temporal resampling was performed using a cubic interpolation. The timeseries for each voxel was upsampled to 1.333 second to correct for

slice-time differences (resulting in 226 volumes for each run). Second, a spatial resampling was performed using a cubic interpolation to correct for head motion, EPI distortion, gradient nonlinearities, and across-scan-session alignment.

4.2.2.3.3 GM mask

We used the surface-based HCP_MMP1 parcellation [68] available in 1.8mm functional space for each participant to generate binary masks that limited our analyses to GM voxels.

4.2.2.4 Individual participant analysis

Analyses for the NSD data were performed separately for each participant using the methods detailed in section 4.2.1.4. We again set up 13 models in total, each of which predicted instantaneous heart period from fMRI timeseries data at time points ranging from t-2.66 seconds to t+13.3 seconds (shifting by one TR at a time, i.e., 1.33 seconds).

We performed one-sampled, two-sided t-tests on the encoding weights for lag time shift +7.99 seconds across runs for each participant with FDR <0.05. For three participants we were able to use more conservative thresholds: S3=0.0001, S5=0.005, and S7=0.001.

4.2.2.5 Group analysis

We tested each participant's average trained model on every other participant for lag time shift +7.99 seconds. In order to do so, we first converted each participant's GM mask into MNI space (using the nsdcode mapping utility) and then created a global participant mask from the union of the individual masks in MNI space. After converting the individual participant weight maps back into nifti images, we used the union MNI GM mask to extract matrices of a common size across participants. These weight matrices were averaged for each

participant. Each average weight matrix was used as the trained model and tested on each individual run for every other participant, resulting in 56 group models. For each of these group models, we calculated the Euclidean distance between weight maps as a measure of similarity. We also replicated the within-participant analysis in MNI space for lag time shift +7.99 seconds.

To visualize the common brain regions involved in prediction of heart period across participants, we generated two probability maps (one for positive weights and one for negative weights) that show the probability of a voxel being significant across participants. To do so, we thresholded and then binarized the positive and negative weights from the individual participant t-tests separately, using FDR <0.05. We then averaged the positive and negative weight maps separately across participants. Each voxel has a value between 0 and 1 that represents the probability of that voxel being significant across all participants. Positive and negative probability maps were overlaid and visualized using Surf Ice.

4.2.3 Generalization

We conducted a cross-dataset analysis to test the generalizability of our method and models, most notably across MRI acquisition resolutions. Using the NSD union MNI GM mask described in section 4.2.2.5, we repeated the physiological denoising steps discussed in section 4.2.1.4 on the Human QA dataset to extract the GLM residuals (X data) using an identical voxel mapping for both datasets. We then averaged the model decoding weights from lag time shift +7.99 seconds for all runs across all NSD participants to use as our average trained model. Finally, we tested each Human QA dataset run at lag time shift +7.5 seconds on the average NSD trained model, resulting in 42 total models. Model accuracy was again

evaluated using Pearson correlation coefficient, along with mean and confidence interval summary measures.

4.3 Results

4.3.1 Within-participant decoding performance

4.3.1.1 Prediction of instantaneous heart period

We first set out to show that the modular approach, where we average decoding maps across runs to predict instantaneous HR in a hold out run (see section 4.2.1.4 above), performs as well as a more conventional approach where a single decoding map is generated from data aggregated across training set runs. This was done on a subset of the single-participant dataset (four sessions, 12 runs total). Supplementary Figure 4.7 shows the Pearson correlation coefficient values for both analysis approaches. The modular approach achieves qualitatively similar results, if not has overall higher prediction accuracy, than the conventional modeling approach. We found this to be acceptable to move forward with the modular approach for all subsequent analyses.

Results for the single-participant dataset from our leave-one-run-out cross-validation pipeline can be seen in Figure 4.3. Here we show that our LASSO-PCA model prediction accuracy in the form of the correlation between observed and predicted heart period using clean, or denoised data (i.e. the residuals from the GLM of cardiac and respiration variability regressors), and the raw data (i.e., without the artifact signal from the physiological noise removed). When we look at how well our model predicts instantaneous heart period

across lag time shifts, (Figure 4.3A), we see several patterns emerge. First, the cleaned data (blue lines), with the physiological noise artifacts removed, performs generally much better across lag time shifts than the raw data (orange lines). Second, we see the expected peak in prediction accuracy around the 0 and +1.5 second lag time shift, which reflects the point at which the physiological artifacts from cardiac and respiratory events would be expressed in the hemodynamic signal (see Figure 4.2A). Finally, there is an expected peak in model performance for the cleaned data but not for the raw data at lag time shift +7.5 seconds, as represented by the dashed vertical line in panel A, which accounts for any potential drive signals in the brain that regulate variation in instantaneous heart period. In particular, we only see this boost in model performance at this time shifted lag in the data where physiological artifacts have been removed from the signal. Figure 4.3B shows the instantaneous heart period timeseries from a single run in green, with the predicted heart period from the cleaned data model at lag time shift +7.5 seconds overlaid in purple. The close tracking of the predicted heart period timeseries with the observed instantaneous heart period visually demonstrates the peak in model performance associated with the brain's drive signal which regulates instantaneous heart period.

The current results use a large within-participant dataset to predict instantaneous heart period from variations in the whole brain hemodynamic signal (i.e., 42 fMRI runs collected across 14 separate sessions). However, is a dataset this large necessary to predict instantaneous heart period within an individual? In order to determine the number of required runs needed for reliable prediction of heart period, we conducted a power analysis using sample sizes n = 2, 4, 8, 10, 16, 20, and 30 at lag time shift +7.5 seconds. As shown in Supplementary Figure 4.8, the correlation between observed and predicted heart period increases

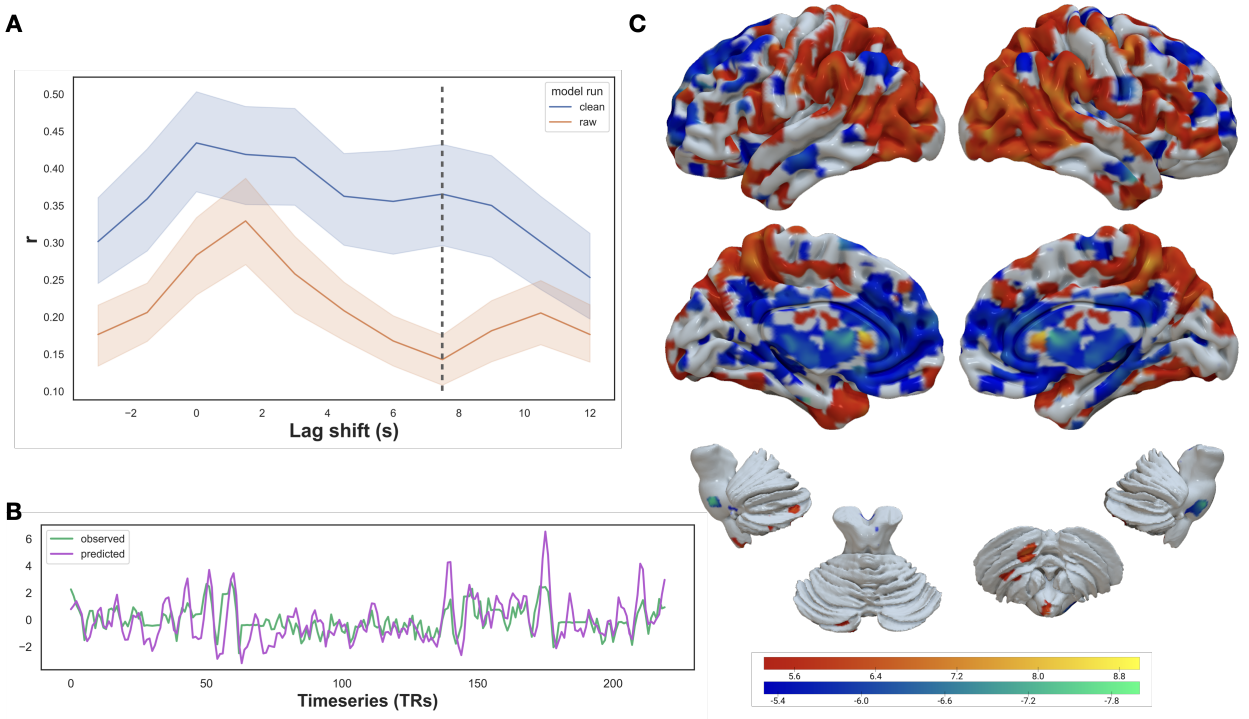

Figure 4.3: A) Mean out-of-sample Pearson correlation coefficient, r, of predicted vs. observed instantaneous heart period across 14 sessions (42 runs total) for each lag time shift for the original (orange) and cleaned (blue) fMRI signal. Shaded regions represent 95% confidence intervals (calculated using 1000 bootstrap iterations). Dashed vertical line represents the drive signal at lag time shift +7.5 seconds. B) Example observed and predicted instantaneous heart period across the timeseries at lag time shift +7.5 seconds for a representative run. C) One-sample t-test (FDR correction <0.00005) of encoding weight maps of instantaneous heart period prediction across sessions and runs for the Human QA dataset participant at lag time shift +7.5 seconds. Positive weights are shown in red-yellow. Negative weights are shown in blue-green.

with increasing sample sizes, plateauing at approximately r = 0.35 at n = 16. However, the largest jump in prediction accuracy occurs when increasing from sample size n = 2 to sample size n = 4, with a greater than 0.1 increase in Pearson correlation coefficient, r. Sample sizes

greater than n = 8 show diminishing increases in prediction accuracy.

4.3.1.2 Areas that associate with instantaneous heart period

Figure 3.3C shows the encoding maps, derived from the decoding weights, that reflect the brain regions that positively (red-yellow) and negatively (blue-green) associate with downstream changes in instantaneous heart period. Brain regions including the bilateral occipital cortex, superior parietal cortex, temporal pole, precuneus, supramarginal, dorsolateral prefrontal cortex (dlPFC), right insula, left cerebellum and a portion of the left medial PFC (mPFC) were positively associated with heart period prediction. Specifically, for these regions increases and or decreases in fMRI BOLD signal were associated with corresponding increased and or decreased instantaneous heart period. Bilateral occipital, superior parietal, supramarginal, temporal pole, superior temporal and temporoparietal junction appear to have the strongest positive association with heart period prediction. Comparatively, bilateral superior frontal, ventromedial PFC (vmPFC), middle temporal, anterior cingulate, angular gyrus, thalamus and periaqueductal gray (PAG) regions were negatively associated with prediction of heart period. For these brain regions, there was an anticorrelated relationship between fMRI BOLD signal and instantaneous heart period, e.g., an increase in the BOLD signal corresponded to a decrease in the instantaneous heart period. Bilateral anterior cingulate, middle temporal, left vmPFC and right posterior cingulate seem to have the strongest negative association with heart period prediction.

4.3.2 Across-participant performance

4.3.2.1 Replicating single-participant results

In order to replicate our within-participant analysis and extend results to characterize between-participant performance, we re-ran our model on the eight participants that make up the NSD (see section 4.2.2.1). For this we repeated the same analysis shown in section 4.3.1 for each NSD participant across lag time shifts -2.67 seconds $\leq$ t $\leq$ 13.3 seconds with the same LASSO-PCA method as used for the Human QA dataset. Figure 4.4A shows the individual model accuracies for each NSD participant as quantified by the correlation between observed and predicted heart period across lag time shifts. We see an expected peak around lag time shift +1.33 seconds, as indicated by the leftmost dashed vertical line, that reflects the time window during which physiological artifacts manifest in the BOLD signal. Three participants (S1, S6, S7), plotted in different shades of gray, have unexpectedly lower artifact signal correlation values (i.e., poor prediction at lag time shifts that should recover the physiological artifacts themselves). The rightmost dashed vertical line on the right at lag time shift +7.99 seconds represents the drive signal and is closest timepoint to the identified drive signal from the Human QA dataset at lag time shift +7.5 seconds. Focusing on how well the individual participant models predict instantaneous heart rate as part of the drive signal that regulates variation in heart period at lag time shift +7.99 seconds, there are some differences across participants. The majority of participants' average model accuracies fall in the 0.15 $\leq$ r $\leq$ 0.2 range (S2, S4-8), while S3 has a larger mean correlation value of r = 0.3065 and S1 has the smallest mean correlation value, of r = 0.0609. However, these patterns also persist across lag time shifts. It is also interesting to note that peak model

performance associated with the drive signal does not appear to be located at lag time shift +7.99 seconds for most participants, and indeed the peak performance for NSD participants varies somewhat across lag time shifts. For example, for participants S3 and S8, the peak performance during the time window associated with the drive signal occurs at +5.33 seconds, while for S4 and S7, it occurs at +6.67 seconds. Additionally, participants S3, S4 and S8 have more obvious drive signal peaks than participants.

It is clear from Figure 4.4A that most, but not all, participants show reliable model performance. However, three participants appear to have overall low prediction accuracy, even in the baseline condition of predicting the time-window when the physiological artifacts are present. Figure 4.4B shows the prediction accuracy from the window that predicts the artifact signal, at lag time shift +1.33 seconds, as shown by the leftmost dashed vertical line in panel A. For each participant bar (along the x axis), the correlation between observed and predicted heart period for every run is plotted as a separate point. The bar itself is the mean value and the error bars are 95% confidence intervals from 1000 bootstrap iterations. Participants are plotted in ascending order from left to right: S6 mean r = -0.0044, S1 mean r = 0.0582, S7 mean r = 0.1028, S2 mean r = 0.3133, S8 mean r = 0.3147, S4 mean r = 0.3773, S5 mean r = 0.389, S3 mean r = 0.4937. Given the different artifact signal response for participants S1, S6, and S7, we might expect diminished results when generalizing to test across participants.

To see how well the pattern of encoding regions observed in the single-participant experiment (section 4.3.1) replicates to a new dataset, we performed the same encoding projection procedure in the NSD sample. Supplementary Figure 4.9 shows these results for all participants except S6, for which no voxels survived correction at FDR <0.05. For participants

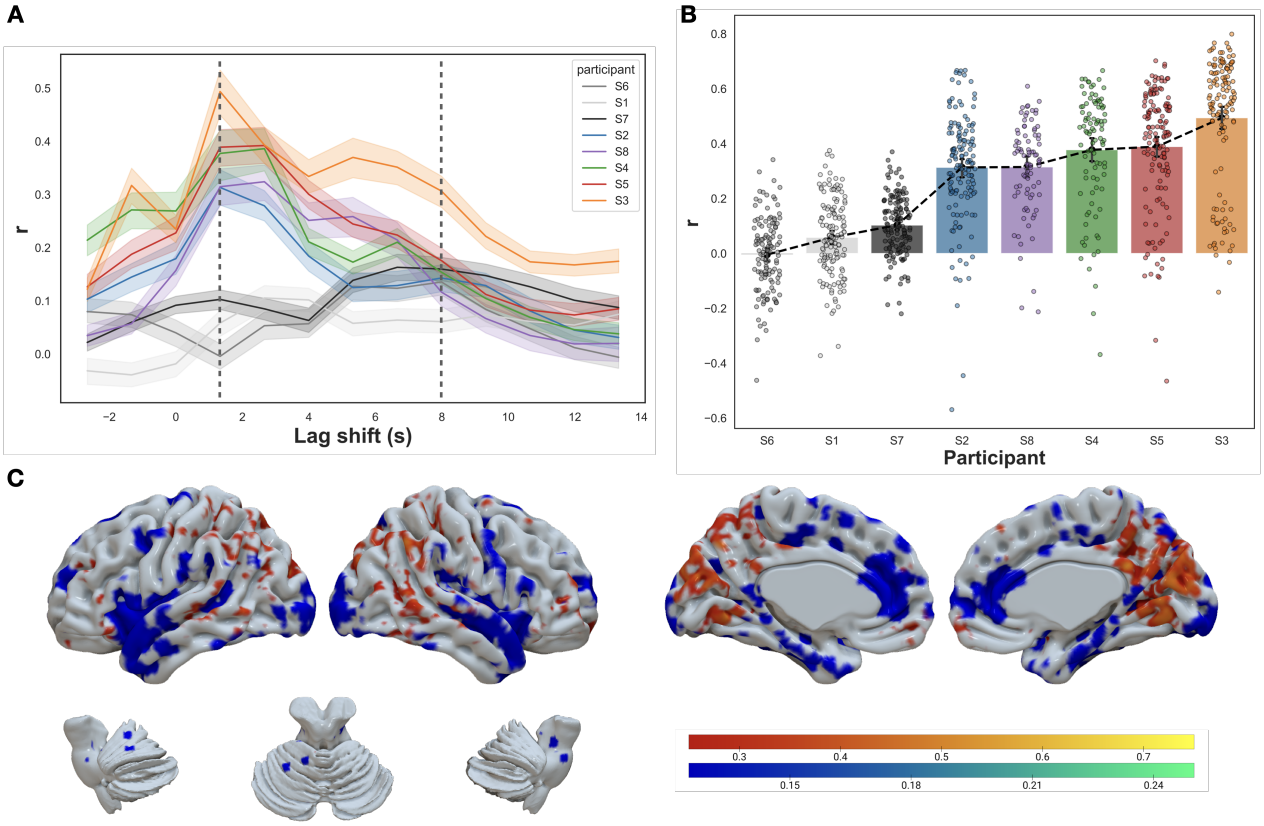

Figure 4.4: A) Mean out-of-sample Pearson correlation coefficient, r, of instantaneous heart period for each participant for each lag time shift for the clean fMRI signal. Shaded regions represent 95% confidence intervals (calculated using 1000 bootstrap iterations). Dashed vertical lines represent the artifact signal (left) at lag time shift +1.33 seconds and the drive signal (right) at lag time shift +7.99 seconds. B) Correlation coefficients for each run for each participant at lag time shift +1.33 seconds, reflected as the leftmost dashed line in panel A. Bars represent the mean r values, error bars show the 95% confidence intervals. C) Probability map of encoding weights of instantaneous heart period prediction averaged across all participants at lag time shift +7.99 seconds. Positive weights are shown in red-yellow. Negative weights are shown in blue-green.

S3, S5 and S7, we used more conservative thresholds of FDR <0.0001, 0.005, and 0.001, respectively. To visualize the common brain regions across participants, we performed a

one-sample, two-sided t-test using the average encoding weight maps for each participant. However, no voxels survived after correcting for multiple comparisons at a fairly liberal threshold, FDR <0.05. Instead, we generated probability maps from the individual participant t-tests that display the probability of a voxel surviving correction across all participants. Given the large percentage of voxels that are significant for at least one participant, 57%, Figure 4.4C shows only the voxels with a positive probability of 0.25 or greater, and voxels with a negative probability of 0.125 or greater. Brain regions along the bilateral medial wall and in the posterior cingulate and superior parietal areas were positively correlated with heart period prediction for at least two participants. Bilateral temporal pole, anterior cingulate, superior frontal and left cerebellum brain regions were negatively correlated with heart period prediction for at least one participant. Thus we were largely able to replicate the cortical regions that regulate variation in instantaneous heart period.

4.3.2.2 Generalization across participants

In order to further evaluate the reliability of our models' decoding weight maps, we tested within-dataset generalization across NSD participants, using the average trained model from one participant and testing it on every other participant. This allowed us to gauge the level of individual differences between decoding weight maps during the drive signal at +7.99 seconds. Figure 4.5A shows the average correlation between observed and predicted heart period for lag time shift +7.99 seconds for each training and testing participant combination of the group analysis. Darker colors represent lower prediction accuracy and lighter colors represent higher drive signal prediction accuracy. As anticipated, we are able to predict instantaneous heart period within participants more accurately than across participants, as

shown in the lighter colors along the diagonal and darker colors off the diagonal. There are some exceptions for particular participants however. Decoding weight maps for S8 predicted instantaneous heart period for S5 (mean r = 0.1592) more accurately than their own heart period signal (mean r = 0.1215). Similarly, S1 predicted S7 more accurately (mean r = 0.1037 compared to mean r = 0.0572). The horizontal and vertical white lines separate the participants with expected artifact signals (S2, S3, S4, S5, S8) from those that behave somewhat as outliers (S1, S6, S7), with either low or no peak in prediction accuracy during the artifact time window. Indeed as expected, when the decoding weight maps from these outlier participants are used as the training model, drive signal prediction accuracy performs more poorly in general, as shown in the darker colors of the lower left section of the heat map. Comparatively, it is interesting to note though, that when the outlier participants are used as test participants (upper right rectangle), model performance is generally higher. Focusing on the participant combinations in the top left rectangle, we show that generalization across participants is somewhat possible, albeit with lower performance. However, it is also clear that certain participant combinations have better model performance, which emphasizes the individual nature of the decoding weight maps that predict instantaneous heart period.

To get a clearer picture of this between-participant generalization, we plotted the within- and between-participant model accuracies separately in Figure 4.5B. Specifically, this compares the diagonal entries of the heat map (within-participant analysis) with the off-diagonal entries of the heat map (between-participant analysis), with gray dots representing a train-test participant combination that includes at least one outlier participant (S1, S6, S7). The within-participant analyses have higher mean prediction accuracies (mean r = 0.1588) compared to the between-participant analysis (mean r = 0.0570). The outlier participant

combinations have slightly lower mean prediction accuracies on average, though there is not a dramatic difference.

One factor that might explain this variability in between-participant prediction accuracy is the overall similarity in their decoding weight maps. To test this we calculated the Euclidean distance between decoding weight maps for each pair of participants and then saw how well this distance was associated with the ability of one participant's model to predict the other's. As a way of visualizing the association between the similarity of different participant weight maps and the average prediction accuracy, we generated the scatterplot shown in Figure 4.5C. Each point represents a between-participant pair (e.g. S1-S2), with gray points again representing participant combinations that contain one or more outlier participants. While there is no significant relationship overall (Pearson r = -0.2022, 95% confidence interval [-0.4416, 0.0641]), it appears that the weight maps of participants that are not outliers are more similar than outlier participants, regardless of prediction accuracy. Thus, similarity in maps may correlate with the ability to generalize, but the current sample may be too small to discern a reliable statistical effect

4.3.3 Across scanner generalization

Finally we set out to see how well decoding maps generated from one MRI scanner, in this case the 7T scanner, generalizes to data from another scanner (the 3T, single-participant dataset). We did this by using the average NSD trained model (across all participants) and testing on the Human QA dataset runs for the drive signal timepoint (+7.99 seconds for NSD, +7.5 seconds for Human QA). This is a true generalization in that scanner strength, scan acquisition parameters and physiological recording methods were different across the two

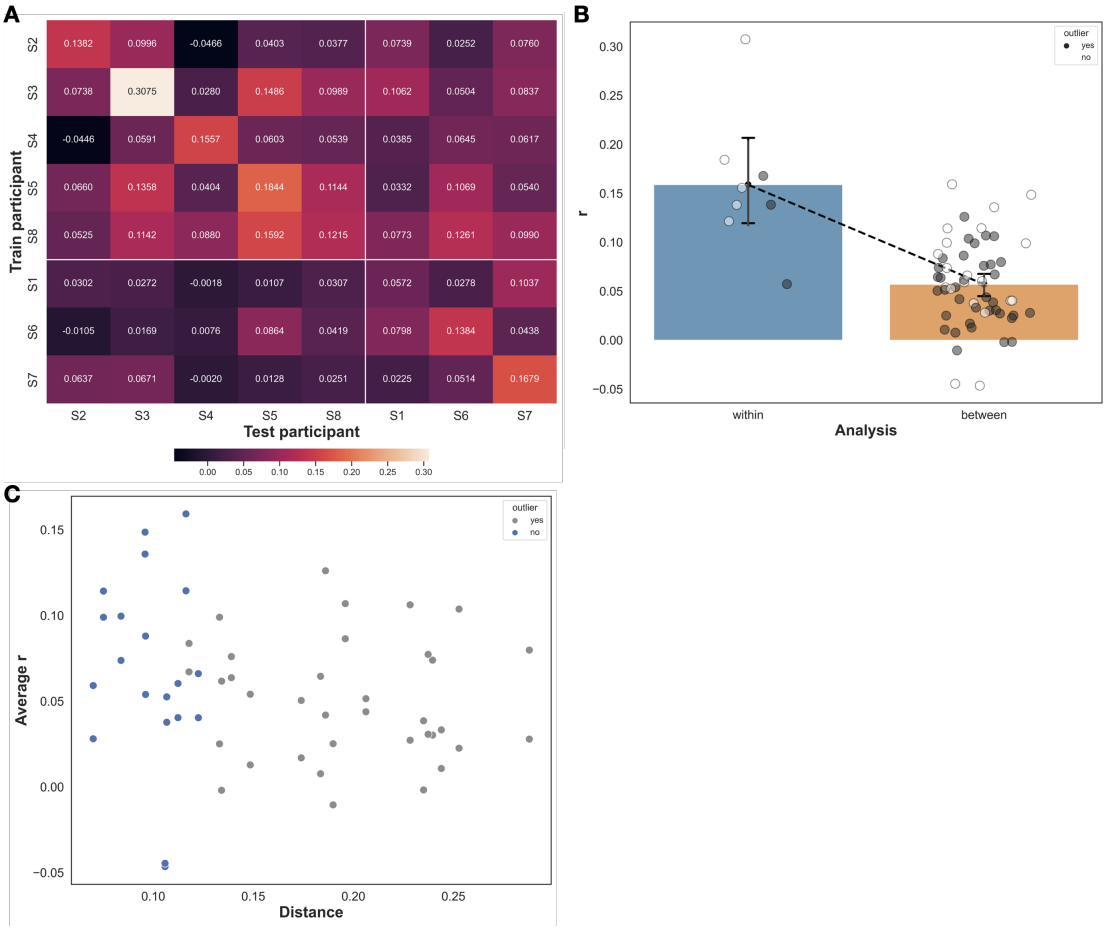

Figure 4.5: A) Heat map of mean out-of-sample Pearson correlation coefficient values from the group analysis across participants at lag time shift +7.99 seconds, with training participants on the y axis and testing participants along the x axis. B) Breakdown of within-participant model r values (heat map diagonals) and across participant model r values (heat map off diagonals). Bars represent the mean r values, error bars show the 95% confidence intervals. Gray points indicate the presence of S1, S6 or S7 in the train-test participant combination. C) Scatter plot of inter-participant euclidean distance, on the x axis and the average decoding accuracy (r values) on the y axis for between-participant models.

datasets. The correlation between observed and predicted heart period across runs ranged from r = -0.0568 to r = 0.4040, with a mean value of r = 0.1424 and 95% confidence interval

[0.1058, 0.1775] (generated from 1000 bootstrap iterations), as shown in Figure 4.6. This demonstrates that our model is generalizable, though prediction accuracy is not as robust as in individual participant analysis.

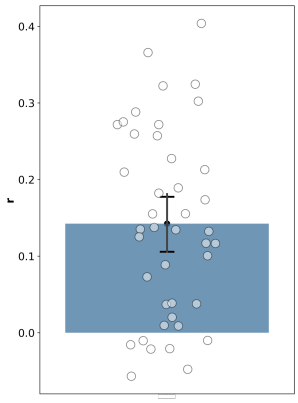

Figure 4.6: Correlation coefficient for each run from across scanner generalization models. The bar shows the mean r value, the error bars show the 95% confidence interval.

4.4 Discussion

Being able to reliably estimate the neural control of cardiac function at the single-participant level would present a critical first step in developing clinical biomarkers of brain contributions to CVD. Using machine learning approaches optimized for high-dimensional datasets, we successfully predicted instantaneous heart period from whole brain hemodynamic data both within and across individuals. We demonstrated these findings in two separate datasets that used different MRI and heart rate acquisition methods. We first observed robust prediction accuracy of instantaneous heart period for single participants. The strength of this within-participant effect has to do with the high statistical power of predicting events across

individual BOLD samples, as opposed to the trialwise or blockwise event-related designs of typical fMRI experiments. This allows for reliable prediction of individual participant effects. Models are also modestly generalizable across individuals, though with marginally lower prediction accuracies than within-participant models. Finally, brain regions in the parietal, frontal and temporal poles and in the anterior cingulate appear to reliably contribute to heart period prediction, suggesting that a network of cortical and subcortical brain regions work together to modulate the downstream brainstem's control of heart period. Furthermore, we have shown that only a handful of runs are needed to adequately power for predicting instantaneous heart period. Therefore, we have shown that dynamic fluctuations in the hemodynamic activity of upstream brain regions comprising the visceral control circuits track with transient fluctuations of heart period.

Despite the individual differences in brain regions associated with heart period prediction across participants in our study, taken together, the overlapping regions from both datasets are largely in line with existing literature. Eisenbarth et al. (2016) demonstrated a multivariate pattern of social threat evoked fMRI activity that predicts heart rate [50]. The positive predictive weights for this model were located in the dorsal anterior cingulate and negative predictive weights in the medial prefrontal cortex, which coincide with our results from both datasets. In addition, Gianaros et al. (2004) studied the associations between heart period and regional cerebral blood flow (rCBF) during a working memory task. Negative correlations between heart period and rCBF in the insula, anterior cingulate also align with results from both of our datasets [65]. Similarly, Porro and colleagues (2003) also reported correlations between heart rate and fMRI activity during pain anticipation [129]. Brain regions in the parietal cortex were positively correlated while regions in the medial

prefrontal cortex and cingulate cortex were negatively correlated, which again overlap with our findings. Finally, Critchley et al. (2000) found associations with heart rate and rCBF during motor and arithmetic tasks [35]. Their negative correlations in the medial prefrontal and cingulate cortices with heart rate also coincide with our results. Altogether, these collective findings emphasize the relationship between specific cortical and subcortical brain regions that might regulate the chronotropic aspect of cardiac activity, and by extension cardiovascular risk. Where our results extend this prior work is in showing that not only are these critical brain regions in higher-level cortex (i.e., upstream from the brainstem) associated with cardiac function, but can reliably predict it on a moment-by-moment basis and at the single-participant level.

With this in mind, there are two main methodological limitations to consider when interpreting the results of the present study. First, there are temporal differences between the parasympathetic and sympathetic heart rate responses [11], that we did not explicitly address in our model. It is possible that we only captured the parasympathetic response that occurs more immediately in response to stress. Intentionally incorporating these two autonomic heart rate responses into our model and investigating how this may alter both the accuracy of prediction and the brain regions involved would be a worthwhile future endeavor. Second, we treated task and rs-fMRI data identically as the tasks from both datasets were not explicitly designed to evoke changes in heart rate, but any spurious changes in cardiac activity only increased usable variance for our models to pick up on. However, it is still possible that there are different brain processes across task-states that may have had some influence on our models. Follow-up work will explore this difference between situations where there may be more top-down control of cardiac function (e.g., tasks) from those where the

system may be in a more passive state (e.g., rest).

Also, while our model predictions showed fairly high consistency at predicting heart period across participants, it is worth noting that the encoding maps showed substantial variability as well. In some ways this is not surprising. The decoding model used here was optimized for prediction, not localization, and uses correlated patterns across the entire brain to build its prediction. This can introduce substantial variability in the decoding weights, and consequently, the encoding projections used to localize regions of influence. Our results in the 7T dataset suggest that any questions on precise localization of control should rely on much larger datasets where consistent patterns across individuals can be more reliably discerned.

Despite these limitations, our study makes clear the feasibility of measuring the cortical and subcortical control signals, including brainstem areas, that associate with variation in cardiac function in humans. To expand on the relevant next steps, repeating our analysis with extended lag time shifts to look for a sympathetic response and trying to tease out the distinction between the two responses could provide some additional nuances to our current results. It would also be valuable to examine any differences between the brain regions most important for parasympathetic versus sympathetic heart rate responses. Performing a simulated lesion analysis, by removing certain brain regions in turn, would be another method of evaluating the relative importance of individual brain regions (or networks) contributions. Finally, replicating this analysis on much larger datasets, of hundreds or thousands of participants, would boost our ability to reliably localize consistent regions of control in the normative human brain. All of these approaches reflect important next steps in our work.

4.5 Conclusion

We have added to the growing existing body of literature looking at brain-heart connections, showing that heart period is reliably predicted by brain activity, even at the single-participant level, within cortical and subcortical regions that overlap with visceral control circuit networks. These results offer a promising step towards the development of a clinically applicable brain-based biomarker for CVD risk.

4.6 Supplementary Figures

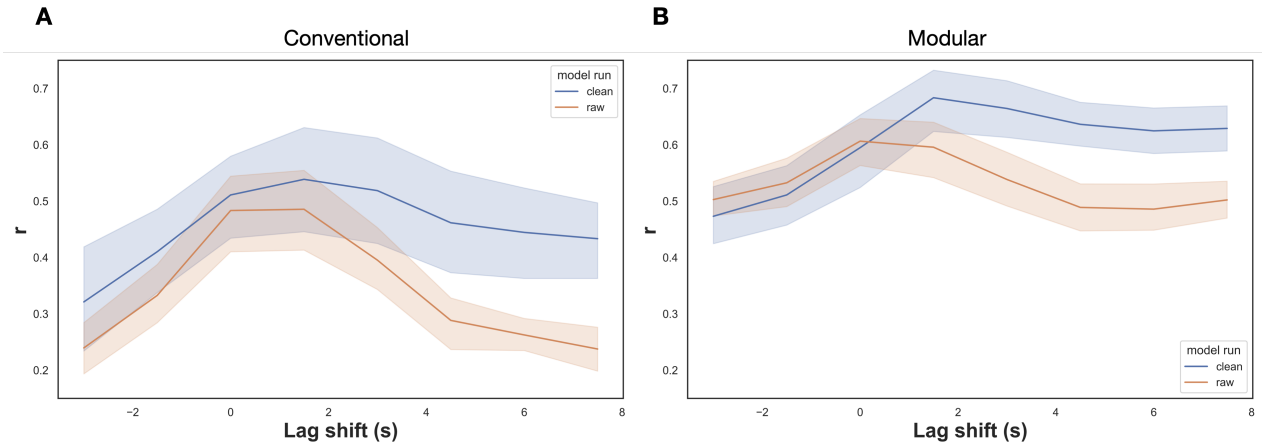

Figure 4.7: Mean out-of-sample Pearson correlation coefficient of predicted and observed instantaneous heart rate across four sessions (12 runs total) for each lag shift for both the clean fMRI signal and the artifact fMRI signal for the conventional analysis (A) and modular analysis (B) approaches. Shaded regions represent 95% confidence intervals (calculated using 1000 bootstrap iterations).

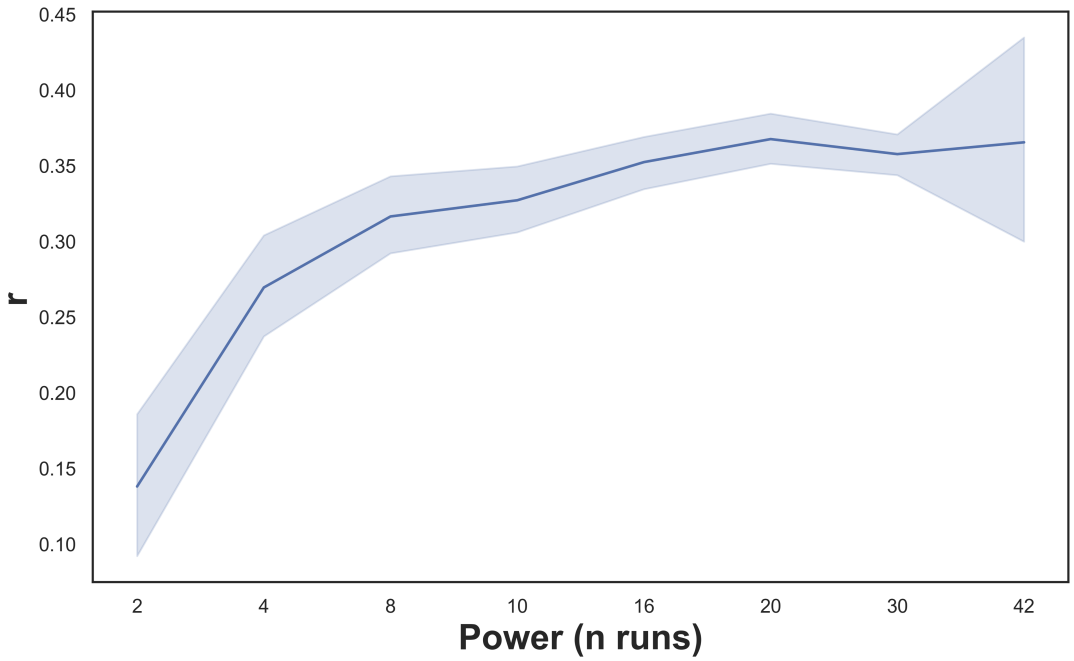

Figure 4.8: Mean out-of-sample Pearson correlation coefficient of predicted and observed instantaneous heart period across different sample sizes of Human QA dataset runs. For sample sizes n = 2 through n = 30, results are averaged across 40 iterations with randomly selected runs. The shaded region represents 95% confidence intervals (calculated using 1000 bootstrap iterations).

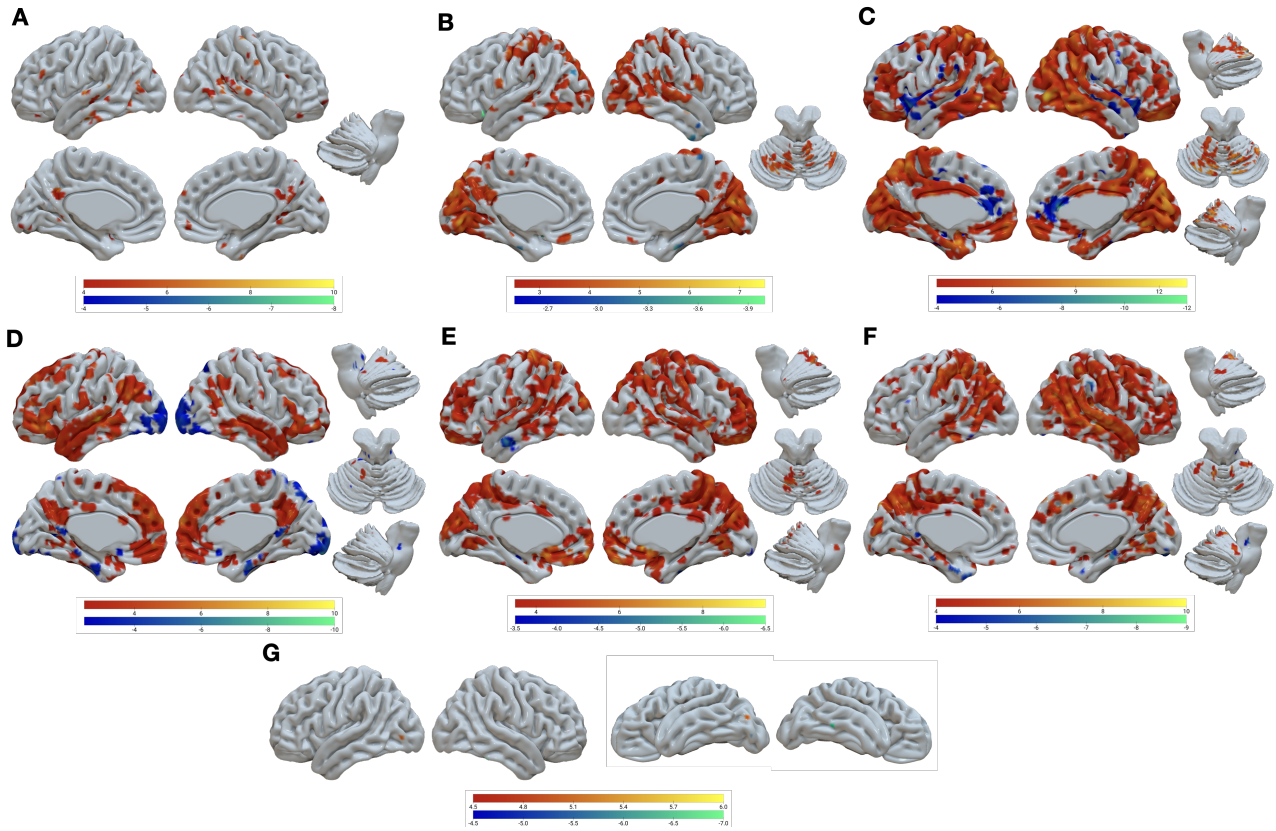

Figure 4.9: One-sample, two-sided t-tests of encoding weight maps of instantaneous heart period prediction for each NSD participant at time shift +7.99 seconds. A) S1, FDR <0.05, B) S2, FDR <0.05, C) S3, FDR <0.0001, D) S4, FDR <0.05, E) S5, FDR <0.005, F) S7 FDR <0.001, G) S8, FDR <0.05. Note: S6 is not included since no voxels survive correction at FDR <0.05. Positive weights are shown in red-yellow. Negative weights are shown in blue-green.

Chapter 5

Conclusion and Future Directions

The goal of this dissertation was to investigate the relationship between the brain and the heart using human neuroimaging and machine learning models. I achieved this goal by addressing two overarching aims. I first sought to predict a subclinical marker of atherosclerotic CVD risk, CA-IMT, using clinically accessible functional and structural brain measures. From there, I focused on the regulation of cardiac control circuits. To do so, I, along with my colleagues, developed *niphlem*, a toolbox to preprocess physiological data collected during MRI scans. I then utilized this toolbox in the prediction of instantaneous heart period from fMRI.

In Chapter 2, I tested whether combining multimodal brain measures that can be easily obtained in clinical settings (resting-state functional connectivity and structural morphology measures from T1-weighted images) would yield a multivariate brain biomarker that reliably predicts CA-IMT. I found that while individual brain measures reliably predict CA-IMT, they do not outperform FRS. And moreover, stacking functional and structural brain measures with FRS did not boost prediction accuracy above that of FRS alone. However, from a methodological perspective, I showed that prediction stacking is a flexible approach that

can be used to determine added predictive utility and furthermore, that multimodal stacking can be applied to individual difference factors. Altogether, these results indicate that while a brain-based biomarker indexed by CA-IMT may not provide additional clinical relevance, multimodal stacking of brain measures remains a useful method that should be utilized for the further investigation of other subclinical CVD markers.

Chapter 3 focuses on detailing the functionality of *niphlem*, our physiological processing toolbox. I described *niphlem*'s three distinct stages: preprocessing, data cleansing and artifact model generation. Using example cardiac (from ECG) and respiration (from pneumatic belt) data, I demonstrated the effectiveness of the toolbox at identifying and removing physiological noise artifacts. I also showed how the noise models generated in *niphlem* can be utilized in neuroimaging analyses. Ultimately, we believe the toolbox facilitates the use of cleaned physiological signals from MRI sessions for analysis alone as well as when incorporating into neuroimaging analyses and in doing so provides a degree of certainty about their quality.

Finally, Chapter 4 applies our work developing *niphlem* to explore the brain networks involved in predicting prevailing heart rate. Using two datasets that consist of extensive repeated data collection within-participants, I tested within- and between-participant prediction of instantaneous heart period using LASSO-PCA, a method optimized for high dimensional data, to identify top-down drive signals that may regulate the fast modulation of cardiac activity. I found reliable heart period prediction within individuals, which is generalizable across individuals, though not as robust. Results indicated that cortical brain regions involved in regulation of heart rate are encompassed within visceral control circuit networks, highlighting the cortex's role in controlling or, at the very least, modulating cardiac function.

There are numerous future directions to pursue from this dissertation, both focusing on extensions for individual aims and combining what we have learned across aims. A worthwhile next step for Aim 1 (Chapter 2) would be a straightforward replication analysis in additional samples, for example, the Neurobiology of Adult Health dataset (NOAH; PD Gianaros, Co-PI Verstynen). More generally, important future directions involve testing for the generalizability of brain-based biomarkers to related clinical markers of atherosclerotic CVD, such as arterial stiffness (measured by pulse wave velocity) [144]. Additionally, incorporating the successful methods used to capture the brain regulatory networks associated with HR from Aim 2 (Chapter 4) into the aims of Chapter 2 constitutes a promising future direction. More specifically, this would help answer the question of whether we can build a reliable brain-based predictor of CVD risk from these direct cardiac control signals or indeed from the prediction residuals.

Relevant next steps for Aim 2 (Chapter 4) would be to add a layer of information to our models that captures relevant task data (e.g., featurization of NSD task images) and to more directly test generalization across individuals using larger datasets, such as NOAH or Human Connectome Project. This also has the potential to address the issue we encountered involving variation in the localization of brain regions that influence prediction of cardiac control across individuals, since a larger sample could allow for characterization of more reliable and consistent patterns. Further extensions that provide more direct clinical applicability center around the following questions. Does the prediction residual of heart rate correlate with known CVD risk factors or clinical markers of CVD and risk? How are the brain-heart connections and the possibility of a brain-related biomarker altered by stress? Another valuable extension project with clinical relevance involves simulating lesions (e.g.,

stroke damage) in brain regions that reliably regulate HR to determine the impact of their removal on modulation of cardiac control. This would involve building a causal model of the brain circuits, which in turn would provide additional information about the nature of brain-heart connections.

Taken together, this dissertation provides incremental steps in our understanding of brain-heart relationships with respect to subclinical CVD risk markers and cortical regulation of heart rate. It is clear, however, that there is a wealth of opportunity for knowledge expansion in this field. Continued work to elucidate the role of the brain's cortical control mechanisms on cardiovascular function and disease risk is essential to further the development of novel therapies and prevention strategies for CVD.

References

[1] Alexandre Abraham, Fabian Pedregosa, Michael Eickenberg, Philippe Gervais, Andreas Mueller, Jean Kossaifi, Alexandre Gramfort, Bertrand Thirion, and Gaël Varoquaux. "Machine learning for neuroimaging with scikit-learn". en. In: *Front. Neuroinform.* 8 (Feb. 2014), p. 14.

[2] Isaac Acquah, Kobina Hagan, Zulqarnain Javed, Mohamad B Taha, Javier Valero-Elizondo, Nwabunie Nwana, Tamer Yahya, Garima Sharma, Martha Gulati, Aziz Hammoud, Michael D Shapiro, Ron Blankstein, Michael J Blaha, Miguel Cainzos-Achirica, and Khurram Nasir. "Social Determinants of Cardiovascular Risk, Subclinical Cardiovascular Disease, and Cardiovascular Events". en. In: *J. Am. Heart Assoc.* 12.6 (Mar. 2023), e025581.

[3] Saud Alhusaini, Sherif Karama, Tuong-Vi Nguyen, Alexander Thiel, Boris C Bernhardt, Simon R Cox, Janie Corley, Adele Taylor, Alan C Evans, John M Star, Mark E Bastin, Joanna M Wardlaw, Ian J Deary, and Simon Ducharme. "Association between carotid atheroma and cerebral cortex structure at age 73 years". en. In: *Ann. Neurol.* 84.4 (Oct. 2018), pp. 576–587.

[4] Emily J Allen, Ghislain St-Yves, Yihan Wu, Jesse L Breedlove, Jacob S Prince, Logan T Dowdle, Matthias Nau, Brad Caron, Franco Pestilli, Ian Charest, J Benjamin Hutchinson, Thomas Naselaris, and Kendrick Kay. "A massive 7T fMRI dataset to bridge cognitive neuroscience and artificial intelligence". en. In: *Nat. Neurosci.* 25.1 (Jan. 2022), pp. 116–126.

[5] Nancy T Artinian, Gerald F Fletcher, Dariush Mozaffarian, Penny Kris-Etherton, Linda Van Horn, Alice H Lichtenstein, Shiriki Kumanyika, William E Kraus, Jerome L Fleg, Nancy S Redeker, Janet C Meininger, Joanne Banks, Eileen M Stuart-Shor, Barbara J Fletcher, Todd D Miller, Suzanne Hughes, Lynne T Braun, Laurie A Kopin, Kathy Berra, Laura L Hayman, Linda J Ewing, Philip A Ades, J Larry Durstine, Nancy Houston-Miller, Lora E Burke, and American Heart Association Prevention Committee of the Council on Cardiovascular Nursing. "Interventions to promote physical activity and dietary lifestyle changes for cardiovascular risk factor reduction in adults: a scientific statement from the American Heart Association". en. In: *Circulation* 122.4 (July 2010), pp. 406–441.

[6] Usman Baber, Roxana Mehran, Samantha Sartori, Mikkel Malby Schoos, Henrik Sillesen, Pieter Muntendam, Mario J Garcia, John Gregson, Stuart Pocock, Erling Falk, and Valentin Fuster. "Prevalence, impact, and predictive value of detecting subclinical coronary and carotid atherosclerosis in asymptomatic adults: the BioImage study". en. In: *J. Am. Coll. Cardiol.* 65.11 (Mar. 2015), pp. 1065–1074.

[7] Florian Beissner, Karin Meissner, Karl-Jürgen Bär, and Vitaly Napadow. "The autonomic brain: an activation likelihood estimation meta-analysis for central processing of autonomic function". en. In: *J. Neurosci.* 33.25 (June 2013), pp. 10503–10511.

[8] Emelia J Benjamin, Paul Muntner, Alvaro Alonso, Marcio S Bittencourt, Clifton W Callaway, April P Carson, Alanna M Chamberlain, Alexander R Chang, Susan Cheng, Sandeep R Das, Francesca N Delling, Luc Djousse, Mitchell S V Elkind, Jane F Ferguson, Myriam Fornage, Lori Chaffin Jordan, Sadiya S Khan, Brett M Kissela, Kristen L Knutson, Tak W Kwan, Daniel T Lackland, Tené T Lewis, Judith H Lichtman, Chris T Longenecker, Matthew Shane Loop, Pamela L Lutsey, Seth S Martin, Kunihiro Matsushita, Andrew E Moran, Michael E Mussolino, Martin O'Flaherty, Ambarish Pandey, Amanda M Perak, Wayne D Rosamond, Gregory A Roth, Uchechukwu K A Sampson, Gary M Satou, Emily B Schroeder, Svati H Shah, Nicole L Spartano, Andrew Stokes, David L Tirschwell, Connie W Tsao, Mintu P Turakhia, Lisa B VanWagner, John T Wilkins, Sally S Wong, Salim S Virani, and American Heart Association Council on Epidemiology and Prevention Statistics Committee and Stroke Statistics Subcommittee. "Heart Disease and Stroke Statistics-2019 Update: A Report From the American Heart Association". en. In: *Circulation* 139.10 (Mar. 2019), e56–e528.

[9] Neal L Benowitz. "Cigarette smoking and cardiovascular disease: pathophysiology and implications for treatment". en. In: *Prog. Cardiovasc. Dis.* 46.1 (2003), pp. 91–111.

[10] Elliot T Berkman and Emily B Falk. "Beyond Brain Mapping: Using Neural Measures to Predict Real-World Outcomes". en. In: *Curr. Dir. Psychol. Sci.* 22.1 (Feb. 2013), pp. 45–50.

[11] G G Berntson, J T Bigger Jr, D L Eckberg, P Grossman, P G Kaufmann, M Malik, H N Nagaraja, S W Porges, J P Saul, P H Stone, and M W van der Molen. "Heart rate variability: origins, methods, and interpretive caveats". en. In: *Psychophysiology* 34.6 (Nov. 1997), pp. 623–648.

[12] G G Berntson, J T Cacioppo, and K S Quigley. “The metrics of cardiac chronotropism: biometric perspectives”. en. In: *Psychophysiology* 32.2 (Mar. 1995), pp. 162–171.

[13] Bild Diane E., Detrano Robert, Peterson Do, Guerci Alan, Liu Kiang, Shahar Eyal, Ouyang Pamela, Jackson Sharon, and Saad Mohammed F. “Ethnic Differences in Coronary Calcification”. In: *Circulation* 111.10 (Mar. 2005), pp. 1313–1320.

[14] Rasmus M Birn, Jason B Diamond, Monica A Smith, and Peter A Bandettini. “Separating respiratory-variation-related fluctuations from neuronal-activity-related fluctuations in fMRI”. en. In: *Neuroimage* 31.4 (July 2006), pp. 1536–1548.

[15] Rasmus M Birn, Monica A Smith, Tyler B Jones, and Peter A Bandettini. “The respiration response function: the temporal dynamics of fMRI signal fluctuations related to changes in respiration”. en. In: *Neuroimage* 40.2 (Apr. 2008), pp. 644–654.

[16] Michael Böhm, Jan-Christian Reil, Prakash Deedwania, Jae B Kim, and Jeffrey S Borer. “Resting heart rate: risk indicator and emerging risk factor in cardiovascular disease”. en. In: *Am. J. Med.* 128.3 (Mar. 2015), pp. 219–228.

[17] Konstantinos Dean Boudoulas, Jeffrey S Borer, and Harisios Boudoulas. “Heart Rate, Life Expectancy and the Cardiovascular System: Therapeutic Considerations”. en. In: *Cardiology* 132.4 (Aug. 2015), pp. 199–212.

[18] Jonathan C W Brooks, Christian F Beckmann, Karla L Miller, Richard G Wise, Carlo A Porro, Irene Tracey, and Mark Jenkinson. “Physiological noise modelling for spinal functional magnetic resonance imaging studies”. en. In: *Neuroimage* 39.2 (Jan. 2008), pp. 680–692.

[19] Daniel J Brotman, Sherita H Golden, and Ilan S Wittstein. "The cardiovascular toll of stress". en. In: *Lancet* 370.9592 (Sept. 2007), pp. 1089–1100.

[20] Renée F A G de Bruijn and M Arfan Ikram. "Cardiovascular risk factors and future risk of Alzheimer's disease". en. In: *BMC Med.* 12 (Nov. 2014), p. 130.

[21] David M Burns. "Epidemiology of smoking-induced cardiovascular disease". en. In: *Prog. Cardiovasc. Dis.* 46.1 (2003), pp. 11–29.

[22] César Caballero-Gaudes and Richard C Reynolds. "Methods for cleaning the BOLD fMRI signal". en. In: *Neuroimage* 154 (July 2017), pp. 128–149.

[23] Francesco P Cappuccio, Daniel Cooper, Lanfranco D'Elia, Pasquale Strazzullo, and Michelle A Miller. "Sleep duration predicts cardiovascular outcomes: a systematic review and meta-analysis of prospective studies". en. In: *Eur. Heart J.* 32.12 (June 2011), pp. 1484–1492.

[24] Valerie A Cardenas, Bruce Reed, Linda L Chao, Helena Chui, Nerses Sanossian, Charles C DeCarli, Wendy Mack, Joel Kramer, Howard N Hodis, Mingzhu Yan, Michael H Buonocore, Owen Carmichael, William J Jagust, and Michael W Weiner. "Associations among vascular risk factors, carotid atherosclerosis, and cortical volume and thickness in older adults". en. In: *Stroke* 43.11 (Nov. 2012), pp. 2865–2870.

[25] Pascal Carrive. "Dual activation of cardiac sympathetic and parasympathetic components during conditioned fear to context in the rat". en. In: *Clin. Exp. Pharmacol. Physiol.* 33.12 (Dec. 2006), pp. 1251–1254.

[26] Centers for Disease Control and Prevention (US), National Center for Chronic Disease Prevention and Health Promotion (US), and Office on Smoking and Health (US).

How Tobacco Smoke Causes Disease: The Biology and Behavioral Basis for Smoking-Attributable Disease: A Report of the Surgeon General. Atlanta (GA): Centers for Disease Control and Prevention (US), Apr. 2011.

[27] Pavla Cermakova, Jie Ding, Osorio Meirelles, Jared Reis, Dorota Religa, Pamela J Schreiner, David R Jacobs, R Nick Bryan, and Lenore J Launer. "Carotid Intima-Media Thickness and Markers of Brain Health in a Biracial Middle-Aged Cohort: CARDIA Brain MRI Sub-study". en. In: *J. Gerontol. A Biol. Sci. Med. Sci.* 75.2 (Jan. 2020), pp. 380–386.

[28] Catie Chang, John P Cunningham, and Gary H Glover. *Influence of heart rate on the BOLD signal: The cardiac response function*. 2009.

[29] Catie Chang and Gary H Glover. "Effects of model-based physiological noise correction on default mode network anti-correlations and correlations". en. In: *Neuroimage* 47.4 (Oct. 2009), pp. 1448–1459.

[30] Mineok Chang, Cheol Whan Lee, Jung-Min Ahn, Rafael Cavalcante, Yohei Sotomi, Yoshinobu Onuma, Yaping Zeng, Duk-Woo Park, Soo-Jin Kang, Seung-Whan Lee, Young-Hak Kim, Seong-Wook Park, Patrick W Serruys, and Seung-Jung Park. "Coronary Artery Bypass Grafting Versus Drug-Eluting Stents Implantation for Previous Myocardial Infarction". en. In: *Am. J. Cardiol.* 118.1 (July 2016), pp. 17–22.

[31] Hsien-Lin Cheng, Chun-Jen Lin, Bing-Wen Soong, Pei-Ning Wang, Feng-Chi Chang, Yu-Te Wu, Kun-Hsien Chou, Ching-Po Lin, Pei-Chi Tu, and I-Hui Lee. "Impairments in cognitive function and brain connectivity in severe asymptomatic carotid stenosis". en. In: *Stroke* 43.10 (Oct. 2012), pp. 2567–2573.

[32] Roger Chou, Tracy Dana, Ian Blazina, Monica Daeges, and Thomas L Jeanne. "Statins for Prevention of Cardiovascular Disease in Adults: Evidence Report and Systematic Review for the US Preventive Services Task Force". en. In: *JAMA* 316.19 (Nov. 2016), pp. 2008–2024.

[33] James H Cole. "Multimodality neuroimaging brain-age in UK biobank: relationship to biomedical, lifestyle, and cognitive factors". en. In: *Neurobiol. Aging* 92 (Aug. 2020), pp. 34–42.

[34] R Cameron Craddock, G Andrew James, Paul E Holtzheimer 3rd, Xiaoping P Hu, and Helen S Mayberg. "A whole brain fMRI atlas generated via spatially constrained spectral clustering". en. In: *Hum. Brain Mapp.* 33.8 (Aug. 2012), pp. 1914–1928.

[35] H D Critchley, D R Corfield, M P Chandler, C J Mathias, and R J Dolan. "Cerebral correlates of autonomic cardiovascular arousal: a functional neuroimaging investigation in humans". en. In: *J. Physiol.* 523 Pt 1.Pt 1 (Feb. 2000), pp. 259–270.

[36] Hugo D Critchley. "Neural mechanisms of autonomic, affective, and cognitive integration". en. In: *J. Comp. Neurol.* 493.1 (Dec. 2005), pp. 154–166.

[37] Hugo D Critchley, Christopher J Mathias, Oliver Josephs, John O'Doherty, Sergio Zanini, Bonnie-Kate Dewar, Lisa Cipolotti, Tim Shallice, and Raymond J Dolan. "Human cingulate cortex and autonomic control: converging neuroimaging and clinical evidence". en. In: *Brain* 126.Pt 10 (Oct. 2003), pp. 2139–2152.

[38] J R Crouse, U Goldbourt, G Evans, J Pinsky, A R Sharrett, P Sorlie, W Riley, and G Heiss. "Risk factors and segment-specific carotid arterial enlargement in the

Atherosclerosis Risk in Communities (ARIC) cohort". en. In: *Stroke* 27.1 (Jan. 1996), pp. 69–75.

[39] Florian Custodis, Stephan H Schirmer, Magnus Baumhäkel, Gerd Heusch, Michael Böhm, and Ulrich Laufs. "Vascular pathophysiology in response to increased heart rate". en. In: *J. Am. Coll. Cardiol.* 56.24 (Dec. 2010), pp. 1973–1983.

[40] Ralph B D'Agostino Sr, Ramachandran S Vasan, Michael J Pencina, Philip A Wolf, Mark Cobain, Joseph M Massaro, and William B Kannel. "General cardiovascular risk profile for use in primary care: the Framingham Heart Study". en. In: *Circulation* 117.6 (Feb. 2008), pp. 743–753.

[41] Björn Dahlöf. "Cardiovascular disease risk factors: epidemiology and risk assessment". en. In: *Am. J. Cardiol.* 105.1 Suppl (Jan. 2010), 3A–9A.

[42] Tawseef Dar, Azar Radfar, Shady Abohashem, Roger K Pitman, Ahmed Tawakol, and Michael T Osborne. "Psychosocial Stress and Cardiovascular Disease". en. In: *Curr. Treat. Options Cardiovasc. Med.* 21.5 (Apr. 2019), p. 23.

[43] Karina W Davidson, Carmela Alcántara, and Gregory E Miller. "Selected psychological comorbidities in coronary heart disease: Challenges and grand opportunities". en. In: *Am. Psychol.* 73.8 (Nov. 2018), pp. 1019–1030.

[44] Roel H R Deckers, Peter van Gelderen, Mario Ries, Olivier Barret, Jeff H Duyn, Vasiliki N Ikonomidou, Masaki Fukunaga, Gary H Glover, and Jacco A de Zwart. "An adaptive filter for suppression of cardiac and respiratory noise in MRI time series data". en. In: *Neuroimage* 33.4 (Dec. 2006), pp. 1072–1081.

[45] David DeSteno, James J Gross, and Laura Kubzansky. “Affective science and health: the importance of emotion and emotion regulation”. en. In: *Health Psychol.* 32.5 (May 2013), pp. 474–486.

[46] Christophe Destrieux, Bruce Fischl, Anders Dale, and Eric Halgren. “Automatic parcellation of human cortical gyri and sulci using standard anatomical nomenclature”. en. In: *Neuroimage* 53.1 (Oct. 2010), pp. 1–15.

[47] Robert Detrano, Alan D Guerci, J Jeffrey Carr, Diane E Bild, Gregory Burke, Aaron R Folsom, Kiang Liu, Steven Shea, Moyses Szklo, David A Bluemke, Daniel H O’Leary, Russell Tracy, Karol Watson, Nathan D Wong, and Richard A Kronmal. “Coronary calcium as a predictor of coronary events in four racial or ethnic groups”. en. In: *N. Engl. J. Med.* 358.13 (Mar. 2008), pp. 1336–1345.

[48] Andrew T Drysdale, Logan Grosenick, Jonathan Downar, Katharine Dunlop, Farrokh Mansouri, Yue Meng, Robert N Fetcho, Benjamin Zebley, Desmond J Oathes, Amit Etkin, Alan F Schatzberg, Keith Sudheimer, Jennifer Keller, Helen S Mayberg, Faith M Gunning, George S Alexopoulos, Michael D Fox, Alvaro Pascual-Leone, Henning U Voss, B J Casey, Marc J Dubin, and Conor Liston. “Resting-state connectivity biomarkers define neurophysiological subtypes of depression”. en. In: *Nat. Med.* 23.1 (Jan. 2017), pp. 28–38.

[49] Caitlin M DuPont, Aidan G C Wright, Stephen B Manuck, Matthew F Muldoon, J Richard Jennings, and Peter J Gianaros. “Is stressor-evoked cardiovascular reactivity a pathway linking positive and negative emotionality to preclinical cardiovascular disease risk?” en. In: *Psychophysiology* 58.3 (Mar. 2021), e13741.

[50] Hedwig Eisenbarth, Luke J Chang, and Tor D Wager. "Multivariate Brain Prediction of Heart Rate and Skin Conductance Responses to Social Threat". en. In: *J. Neurosci.* 36.47 (Nov. 2016), pp. 11987–11998.

[51] William J Elliott. "Systemic hypertension". en. In: *Curr. Probl. Cardiol.* 32.4 (Apr. 2007), pp. 201–259.

[52] Kirk I Erickson, J David Creswell, Timothy D Verstynen, and Peter J Gianaros. "Health Neuroscience: Defining a New Field". en. In: *Curr. Dir. Psychol. Sci.* 23.6 (Dec. 2014), pp. 446–453.

[53] Oscar Esteban, Christopher J Markiewicz, Ross W Blair, Craig A Moodie, A Ilkay Isik, Asier Erramuzpe, James D Kent, Mathias Goncalves, Elizabeth DuPre, Madeleine Snyder, Hiroyuki Oya, Satrajit S Ghosh, Jessey Wright, Joke Durnez, Russell A Poldrack, and Krzysztof J Gorgolewski. "fMRIPrep: a robust preprocessing pipeline for functional MRI". en. In: *Nat. Methods* 16.1 (Jan. 2019), pp. 111–116.

[54] Laura Fedele and Thomas Brand. "The Intrinsic Cardiac Nervous System and Its Role in Cardiac Pacemaking and Conduction". en. In: *J Cardiovasc Dev Dis* 7.4 (Nov. 2020).

[55] Emily S Finn. "Is it time to put rest to rest?" en. In: *Trends Cogn. Sci.* 25.12 (Dec. 2021), pp. 1021–1032.

[56] V S Fonov, A C Evans, R C McKinstry, C R Almli, and D L Collins. "Unbiased nonlinear average age-appropriate brain templates from birth to adulthood". In: *Neuroimage* 47 (July 2009), S102.

[57] Kim Fox, Jeffrey S Borer, A John Camm, Nicolas Danchin, Roberto Ferrari, Jose L Lopez Sendon, Philippe Gabriel Steg, Jean-Claude Tardif, Luigi Tavazzi, Michal Tendera, and Heart Rate Working Group. "Resting heart rate in cardiovascular disease". en. In: *J. Am. Coll. Cardiol.* 50.9 (Aug. 2007), pp. 823–830.

[58] David M Fresco, Amy K Roy, Samantha Adelsberg, Saren Seeley, Emmanuel Garcıa-Lesy, Conor Liston, and Douglas S Mennin. "Distinct Functional Connectivities Predict Clinical Response with Emotion Regulation Therapy". en. In: *Front. Hum. Neurosci.* 11 (Mar. 2017), p. 86.

[59] Karl J Friston. "Functional and effective connectivity in neuroimaging: A synthesis". en. In: *Hum. Brain Mapp.* 2.1-2 (1994), pp. 56–78.

[60] Masaki Fukunaga, Silvina G Horovitz, Jacco A de Zwart, Peter van Gelderen, Thomas J Balkin, Allen R Braun, and Jeff H Duyn. "Metabolic origin of BOLD signal fluctuations in the absence of stimuli". en. In: *J. Cereb. Blood Flow Metab.* 28.7 (July 2008), pp. 1377–1387.

[61] Georg Gelbenegger, Marek Postula, Ladislav Pecen, Sigrun Halvorsen, Maciej Lesiak, Christian Schoergenhofer, Bernd Jilma, Christian Hengstenberg, and Jolanta M Siller-Matula. "Aspirin for primary prevention of cardiovascular disease: a meta-analysis with a particular focus on subgroups". en. In: *BMC Med.* 17.1 (Nov. 2019), p. 198.

[62] Eco J C de Geus, Peter J Gianaros, Ryan C Brindle, J Richard Jennings, and Gary G Berntson. "Should heart rate variability be "corrected" for heart rate? Biological, quantitative, and interpretive considerations". en. In: *Psychophysiology* 56.2 (Feb. 2019), e13287.

[63] Peter J Gianaros, Thomas E Kraynak, Dora C-H Kuan, James J Gross, Kateri McRae, Ahmad R Hariri, Stephen B Manuck, Javier Rasero, and Timothy D Verstynen. "Affective brain patterns as multivariate neural correlates of cardiovascular disease risk". en. In: *Soc. Cogn. Affect. Neurosci.* (Apr. 2020).

[64] Peter J Gianaros, Lei K Sheu, Fatma Uyar, Jayanth Koushik, J Richard Jennings, Tor D Wager, Aarti Singh, and Timothy D Verstynen. "A Brain Phenotype for Stressor-Evoked Blood Pressure Reactivity". en. In: *J. Am. Heart Assoc.* 6.9 (Aug. 2017), e006053.

[65] Peter J Gianaros, Frederik M Van Der Veen, and J Richard Jennings. "Regional cerebral blood flow correlates with heart period and high-frequency heart period variability during working-memory tasks: Implications for the cortical and subcortical regulation of cardiac autonomic activity". en. In: *Psychophysiology* 41.4 (July 2004), pp. 521–530.

[66] Peter J Gianaros and Tor D Wager. "Brain-Body Pathways Linking Psychological Stress and Physical Health". en. In: *Curr. Dir. Psychol. Sci.* 24.4 (Aug. 2015), pp. 313–321.

[67] Annie T Ginty, Thomas E Kraynak, James P Fisher, and Peter J Gianaros. "Cardiovascular and autonomic reactivity to psychological stress: Neurophysiological substrates and links to cardiovascular disease". en. In: *Auton. Neurosci.* 207 (Nov. 2017), pp. 2–9.

[68] Matthew F Glasser, Timothy S Coalson, Emma C Robinson, Carl D Hacker, John Harwell, Essa Yacoub, Kamil Ugurbil, Jesper Andersson, Christian F Beckmann,

Mark Jenkinson, Stephen M Smith, and David C Van Essen. “A multi-modal parcellation of human cerebral cortex”. en. In: *Nature* 536.7615 (July 2016), pp. 171–178.

[69] G H Glover, T Q Li, and D Ress. “Image-based method for retrospective correction of physiological motion effects in fMRI: RETROICOR”. en. In: *Magn. Reson. Med.* 44.1 (July 2000), pp. 162–167.

[70] Zachary D Goldberger, Javier A Valle, Vineet K Dandekar, Paul S Chan, Dennis T Ko, and Brahmajee K Nallamothu. “Are changes in carotid intima-media thickness related to risk of nonfatal myocardial infarction? A critical review and meta-regression analysis”. en. In: *Am. Heart J.* 160.4 (Oct. 2010), pp. 701–714.

[71] A R Guimaraes, J R Melcher, T M Talavage, J R Baker, P Ledden, B R Rosen, N Y Kiang, B C Fullerton, and R M Weisskoff. “Imaging subcortical auditory activity in humans”. en. In: *Hum. Brain Mapp.* 6.1 (1998), pp. 33–41.

[72] P G Guyenet and N Koshiya. “Working model of the sympathetic chemoreflex in rats”. en. In: *Clin. Exp. Hypertens.* 17.1-2 (Jan. 1995), pp. 167–179.

[73] Ann K Harvey, Kyle T S Pattinson, Jonathan C W Brooks, Stephen D Mayhew, Mark Jenkinson, and Richard G Wise. “Brainstem functional magnetic resonance imaging: disentangling signal from physiological noise”. en. In: *J. Magn. Reson. Imaging* 28.6 (Dec. 2008), pp. 1337–1344.

[74] Stefan Haufe, Frank Meinecke, Kai Görgen, Sven Dähne, John-Dylan Haynes, Benjamin Blankertz, and Felix Bießmann. “On the interpretation of weight vectors of lin-

ear models in multivariate neuroimaging". en. In: *Neuroimage* 87 (Feb. 2014), pp. 96–110.

[75] Feng J He, Jiafu Li, and Graham A Macgregor. "Effect of longer term modest salt reduction on blood pressure: Cochrane systematic review and meta-analysis of randomised trials". en. In: *BMJ* 346 (Apr. 2013), f1325.

[76] American Heart Association Council on Epidemiology et al. "Heart disease and stroke statistics—2023 update: a report from the American Heart Association". In: *Circulation* (2023).

[77] Howard N Hodis, Wendy J Mack, Victor W Henderson, Donna Shoupe, Matthew J Budoff, Juliana Hwang-Levine, Yanjie Li, Mei Feng, Laurie Dustin, Naoko Kono, Frank Z Stanczyk, Robert H Selzer, Stanley P Azen, and ELITE Research Group. "Vascular Effects of Early versus Late Postmenopausal Treatment with Estradiol". en. In: *N. Engl. J. Med.* 374.13 (Mar. 2016), pp. 1221–1231.

[78] Jennifer A Hoeting, David Madigan, Adrian E Raftery, and Chris T Volinsky. "Bayesian Model Averaging: A Tutorial". In: *Stat. Sci.* 14.4 (1999), pp. 382–401.

[79] William A Huang, Noel G Boyle, and Marmar Vaseghi. "Cardiac Innervation and the Autonomic Nervous System in Sudden Cardiac Death". en. In: *Card. Electrophysiol. Clin.* 9.4 (Dec. 2017), pp. 665–679.

[80] H V Huikuri, V Jokinen, M Syvänne, M S Nieminen, K E Airaksinen, M J Ikäheimo, J M Koistinen, H Kauma, A Y Kesäniemi, S Majahalme, K O Niemelä, and M H Frick. "Heart rate variability and progression of coronary atherosclerosis". en. In: *Arterioscler. Thromb. Vasc. Biol.* 19.8 (Aug. 1999), pp. 1979–1985.

[81] Amorina Ishai, Michael T Osborne, Brian Tung, Ying Wang, Basma Hammad, Tomas Patrich, Blake Oberfeld, Zahi A Fayad, Jon T Giles, Janet Lo, Lisa M Shin, Steven K Grinspoon, Karestan C Koenen, Roger K Pitman, and Ahmed Tawakol. "Amygdalar Metabolic Activity Independently Associates With Progression of Visceral Adiposity". en. In: *J. Clin. Endocrinol. Metab.* 104.4 (Apr. 2019), pp. 1029–1038.

[82] J Richard Jennings, Alicia F Heim, Dora Chieh-Hsin Kuan, Peter J Gianaros, Matthew F Muldoon, and Stephen B Manuck. "Use of total cerebral blood flow as an imaging biomarker of known cardiovascular risks". en. In: *Stroke* 44.9 (Sept. 2013), pp. 2480–2485.

[83] J Richard Jennings, Alicia F Heim, Lei K Sheu, Matthew F Muldoon, Christopher Ryan, H Michael Gach, Claudiu Schirda, and Peter J Gianaros. "Brain Regional Blood Flow and Working Memory Performance Predict Change in Blood Pressure Over 2 Years". en. In: *Hypertension* 70.6 (Dec. 2017), pp. 1132–1141.

[84] J Richard Jennings, Matthew F Muldoon, Ellen M Whyte, Joelle Scanlon, Julie Price, and Carolyn C Meltzer. "Brain imaging findings predict blood pressure response to pharmacological treatment". en. In: *Hypertension* 52.6 (Dec. 2008), pp. 1113–1119.

[85] Xavier Jouven, Jean-Philippe Empana, Peter J Schwartz, Michel Desnos, Dominique Courbon, and Pierre Ducimetière. "Heart-rate profile during exercise as a predictor of sudden death". en. In: *N. Engl. J. Med.* 352.19 (May 2005), pp. 1951–1958.

[86] Safi U Khan, Zulqarnain Javed, Ahmad N Lone, Sourbha S Dani, Zahir Amin, Sadeer G Al-Kindi, Salim S Virani, Garima Sharma, Ron Blankstein, Michael J Blaha, Miguel Cainzos-Achirica, and Khurram Nasir. "Social Vulnerability and Premature Cardio-

vascular Mortality Among US Counties, 2014 to 2018". en. In: *Circulation* 144.16 (Oct. 2021), pp. 1272–1279.

[87] Michael King, Joe Kingery, and Baretta Casey. "Diagnosis and evaluation of heart failure". en. In: *Am. Fam. Physician* 85.12 (June 2012), pp. 1161–1168.

[88] Mika Kivimäki and Andrew Steptoe. "Effects of stress on the development and progression of cardiovascular disease". en. In: *Nat. Rev. Cardiol.* 15.4 (Apr. 2018), pp. 215–229.

[89] D S Knopman, A D Penman, D J Catellier, L H Coker, D K Shibata, A R Sharrett, and T H Mosley Jr. "Vascular risk factors and longitudinal changes on brain MRI: the ARIC study". en. In: *Neurology* 76.22 (May 2011), pp. 1879–1885.

[90] Kumiko Kobayashi, Masahiro Akishita, Wei Yu, Masayoshi Hashimoto, Mitsuo Ohni, and Kenji Toba. "Interrelationship between non-invasive measurements of atherosclerosis: flow-mediated dilation of brachial artery, carotid intima-media thickness and pulse wave velocity". en. In: *Atherosclerosis* 173.1 (Mar. 2004), pp. 13–18.

[91] Thomas E Kraynak, Anna L Marsland, and Peter J Gianaros. "Neural Mechanisms Linking Emotion with Cardiovascular Disease". en. In: *Curr. Cardiol. Rep.* 20.12 (Oct. 2018), p. 128.

[92] Florian Lederbogen, Elisabeth Ulshöfer, Annika Peifer, Phöbe Fehlner, Edda Bilek, Fabian Streit, Michael Deuschle, Heike Tost, and Andreas Meyer-Lindenberg. "No association between cardiometabolic risk and neural reactivity to acute psychosocial stress". en. In: *Neuroimage Clin* 20 (Oct. 2018), pp. 1115–1122.

[93] Franziskus Liem, Gaël Varoquaux, Jana Kynast, Frauke Beyer, Shahrzad Kharabian Masouleh, Julia M Huntenburg, Leonie Lampe, Mehdi Rahim, Alexandre Abraham, R Cameron Craddock, Steffi Riedel-Heller, Tobias Luck, Markus Loeffler, Matthias L Schroeter, Anja Veronica Witte, Arno Villringer, and Daniel S Margulies. "Predicting brain-age from multimodal imaging data captures cognitive impairment". en. In: *Neuroimage* 148 (Mar. 2017), pp. 179–188.

[94] Richard S Liu, Sophie Dunn, Anneke C Grobler, Katherine Lange, Denise Becker, Greta Goldsmith, John B Carlin, Markus Juonala, Melissa Wake, and David P Burgner. "Carotid artery intima-media thickness, distensibility and elasticity: population epidemiology and concordance in Australian children aged 11-12 years old and their parents". en. In: *BMJ Open* 9.Suppl 3 (July 2019), pp. 23–33.

[95] Thomas T Liu. "Noise contributions to the fMRI signal: An overview". en. In: *Neuroimage* 143 (Dec. 2016), pp. 141–151.

[96] Lloyd-Jones Donald M., Hong Yuling, Labarthe Darwin, Mozaffarian Dariush, Appel Lawrence J., Van Horn Linda, Greenlund Kurt, Daniels Stephen, Nichol Graham, Tomaselli Gordon F., Arnett Donna K., Fonarow Gregg C., Ho P. Michael, Lauer Michael S., Masoudi Frederick A., Robertson Rose Marie, Roger Véronique, Schwamm Lee H., Sorlie Paul, Yancy Clyde W., and Rosamond Wayne D. "Defining and Setting National Goals for Cardiovascular Health Promotion and Disease Reduction". In: *Circulation* 121.4 (Feb. 2010), pp. 586–613.

[97] Matthias W Lorenz, Joseph F Polak, Maryam Kavousi, Ellisiv B Mathiesen, Henry Völzke, Tomi-Pekka Tuomainen, Dirk Sander, Matthieu Plichart, Alberico L Catapano, Christine M Robertson, Stefan Kiechl, Tatjana Rundek, Moıse Desvarieux,

Lars Lind, Caroline Schmid, Pronabesh DasMahapatra, Lu Gao, Kathrin Ziegelbauer, Michiel L Bots, Simon G Thompson, and PROG-IMT Study Group. "Carotid intima-media thickness progression to predict cardiovascular events in the general population (the PROG-IMT collaborative project): a meta-analysis of individual participant data". en. In: *Lancet* 379.9831 (June 2012), pp. 2053–2062.

[98] Catherine M Loria, Kiang Liu, Cora E Lewis, Stephen B Hulley, Stephen Sidney, Pamela J Schreiner, O Dale Williams, Diane E Bild, and Robert Detrano. "Early adult risk factor levels and subsequent coronary artery calcification: the CARDIA Study". en. In: *J. Am. Coll. Cardiol.* 49.20 (May 2007), pp. 2013–2020.

[99] Torben E Lund, Kristoffer H Madsen, Karam Sidaros, Wen-Lin Luo, and Thomas E Nichols. "Non-white noise in fMRI: does modelling have an impact?" en. In: *Neuroimage* 29.1 (Jan. 2006), pp. 54–66.

[100] Elena Makovac, Julian F Thayer, and Cristina Ottaviani. "A meta-analysis of non-invasive brain stimulation and autonomic functioning: Implications for brain-heart pathways to cardiovascular disease". en. In: *Neurosci. Biobehav. Rev.* 74.Pt B (Mar. 2017), pp. 330–341.

[101] Barbara K Marebwa, Robert J Adams, Gayenell S Magwood, Alexandra Basilakos, Martina Mueller, Chris Rorden, Julius Fridriksson, and Leonardo Bonilha. "Cardiovascular Risk Factors and Brain Health: Impact on Long-Range Cortical Connections and Cognitive Performance". en. In: *J. Am. Heart Assoc.* 7.23 (Dec. 2018), e010054.

[102] J B Meigs, R B D'Agostino Sr, P W Wilson, L A Cupples, D M Nathan, and D E Singer. "Risk variable clustering in the insulin resistance syndrome. The Framingham Offspring Study". en. In: *Diabetes* 46.10 (Oct. 1997), pp. 1594–1600.

[103] George A Mensah. "Eliminating disparities in cardiovascular health: six strategic imperatives and a framework for action". en. In: *Circulation* 111.10 (Mar. 2005), pp. 1332–1336.

[104] George A Mensah, Ali H Mokdad, Earl S Ford, Kurt J Greenlund, and Janet B Croft. "State of disparities in cardiovascular health in the United States". en. In: *Circulation* 111.10 (Mar. 2005), pp. 1233–1241.

[105] Ronald P Mensink, Peter L Zock, Arnold D M Kester, and Martijn B Katan. "Effects of dietary fatty acids and carbohydrates on the ratio of serum total to HDL cholesterol and on serum lipids and apolipoproteins: a meta-analysis of 60 controlled trials". en. In: *Am. J. Clin. Nutr.* 77.5 (May 2003), pp. 1146–1155.

[106] Kasra Moazzami, Matthew T Wittbrodt, Bruno B Lima, Jonathon A Nye, Puja K Mehta, Brad D Pearce, Zakaria Almuwaqqat, Muhammad Hammadah, Oleksiy Levantsevych, Yan V Sun, Paolo Raggi, Ernest V Garcia, Margarethe Goetz, Arshed A Quyyumi, J Douglas Bremner, Viola Vaccarino, and Amit J Shah. "Higher Activation of the Rostromedial Prefrontal Cortex During Mental Stress Predicts Major Cardiovascular Disease Events in Individuals With Coronary Artery Disease". en. In: *Circulation* 142.5 (Aug. 2020), pp. 455–465.

[107] Francesco Moroni, Enrico Ammirati, Marco Magnoni, Fabrizio D'Ascenzo, Matteo Anselmino, Nicoletta Anzalone, Maria Assunta Rocca, Andrea Falini, Massimo Fil-

ippi, and Paolo G Camici. “Carotid atherosclerosis, silent ischemic brain damage and brain atrophy: A systematic review and meta-analysis”. en. In: *Int. J. Cardiol.* 223 (Nov. 2016), pp. 681–687.

[108] Majon Muller, Yolanda van der Graaf, Ale Algra, Jeroen Hendrikse, Willem P Mali, Mirjam I Geerlings, and SMART Study Group. “Carotid atherosclerosis and progression of brain atrophy: the SMART-MR study”. en. In: *Ann. Neurol.* 70.2 (Aug. 2011), pp. 237–244.

[109] Pradeep Natarajan et al. “Multiethnic Exome-Wide Association Study of Subclinical Atherosclerosis”. en. In: *Circ. Cardiovasc. Genet.* 9.6 (Dec. 2016), pp. 511–520.

[110] Alina Nickel, Simon Kessner, Andreas Niebuhr, Julian Schröder, Caroline Malherbe, Felix Fischer, Marlene Heinze, Bastian Cheng, Jens Fiehler, Hans Pinnschmidt, Axel Larena-Avellaneda, Christian Gerloff, and Götz Thomalla. “Cortical thickness and cognitive performance in asymptomatic unilateral carotid artery stenosis”. en. In: *BMC Cardiovasc. Disord.* 19.1 (June 2019), p. 154.

[111] John T O’Brien. “Vascular cognitive impairment”. en. In: *Am. J. Geriatr. Psychiatry* 14.9 (Sept. 2006), pp. 724–733.

[112] Erin L O’Callaghan, Fiona D McBryde, Amy E Burchell, Laura E K Ratcliffe, Liviu Nicolae, Ivor Gillbe, Derek Carr, Emma C Hart, Angus K Nightingale, Nikunj K Patel, and Julian F R Paton. “Deep brain stimulation for the treatment of resistant hypertension”. en. In: *Curr. Hypertens. Rep.* 16.11 (Nov. 2014), p. 493.

[113] D Ongür and J L Price. "The organization of networks within the orbital and medial prefrontal cortex of rats, monkeys and humans". en. In: *Cereb. Cortex* 10.3 (Mar. 2000), pp. 206–219.

[114] Halvor Øygarden. "Carotid Intima-Media Thickness and Prediction of Cardiovascular Disease". en. In: *J. Am. Heart Assoc.* 6.1 (Jan. 2017).

[115] P Palatini and S Julius. "The physiological determinants and risk correlations of elevated heart rate". en. In: *Am. J. Hypertens.* 12.1 Pt 2 (Jan. 1999), 3S–8S.

[116] Paolo Palatini. "Heart rate as an independent risk factor for cardiovascular disease: current evidence and basic mechanisms". en. In: *Drugs* 67 Suppl 2 (2007), pp. 3–13.

[117] Tullio Palmerini, Patrick Serruys, Arie Pieter Kappetein, Philippe Genereux, Diego Della Riva, Letizia Bacchi Reggiani, Evald Høj Christiansen, Niels R Holm, Leif Thuesen, Timo Makikallio, Marie Claude Morice, Jung-Min Ahn, Seung-Jung Park, Holger Thiele, Enno Boudriot, Mario Sabatino, Mattia Romanello, Giuseppe Biondi-Zoccai, Raphael Cavalcante, Joseph F Sabik, and Gregg W Stone. "Clinical outcomes with percutaneous coronary revascularization vs coronary artery bypass grafting surgery in patients with unprotected left main coronary artery disease: A meta-analysis of 6 randomized trials and 4,686 patients". en. In: *Am. Heart J.* 190 (Aug. 2017), pp. 54–63.

[118] Matthew P Pase, Natalie A Grima, Con K Stough, Andrew Scholey, and Andrew Pipingas. "Cardiovascular disease risk and cerebral blood flow velocity". en. In: *Stroke* 43.10 (Oct. 2012), pp. 2803–2805.

[119] Shivani A Patel, Mohammed K Ali, K M Venkat Narayan, and Neil K Mehta. "County-Level Variation in Cardiovascular Disease Mortality in the United States in 2009-2013: Comparative Assessment of Contributing Factors". en. In: *Am. J. Epidemiol.* 184.12 (Dec. 2016), pp. 933–942.

[120] Eugene Patterson, Sunny S Po, Benjamin J Scherlag, and Ralph Lazzara. "Triggered firing in pulmonary veins initiated by in vitro autonomic nerve stimulation". en. In: *Heart Rhythm* 2.6 (June 2005), pp. 624–631.

[121] Rupert A Payne. "Cardiovascular risk". en. In: *Br. J. Clin. Pharmacol.* 74.3 (Sept. 2012), pp. 396–410.

[122] Fabian Pedregosa, Gaël Varoquaux, Alexandre Gramfort, Vincent Michel, Bertrand Thirion, Olivier Grisel, Mathieu Blondel, Peter Prettenhofer, Ron Weiss, Vincent Dubourg, et al. "Scikit-learn: Machine learning in Python". In: *the Journal of machine Learning research* 12 (2011), pp. 2825–2830.

[123] J Perk, A Rosengren, et al. "Prevention of cardiovascular disease: Risk factor detection and modification". In: *The ESC Textbook of* (2006).

[124] Christine Perret-Guillaume, Laure Joly, and Athanase Benetos. "Heart rate as a risk factor for cardiovascular disease". en. In: *Prog. Cardiovasc. Dis.* 52.1 (July 2009), pp. 6–10.

[125] Sanne A E Peters, Hester M den Ruijter, Michiel L Bots, and Karel G M Moons. "Improvements in risk stratification for the occurrence of cardiovascular disease by imaging subclinical atherosclerosis: a systematic review". en. In: *Heart* 98.3 (Feb. 2012), pp. 177–184.

[126] Massimo F Piepoli, Arno W Hoes, Stefan Agewall, Christian Albus, Carlos Brotons, Alberico L Catapano, Marie-Therese Cooney, Ugo Corrà, Bernard Cosyns, Christi Deaton, Ian Graham, Michael Stephen Hall, F D Richard Hobbs, Maja-Lisa Løchen, Herbert Löllgen, Pedro Marques-Vidal, Joep Perk, Eva Prescott, Josep Redon, Dimitrios J Richter, Naveed Sattar, Yvo Smulders, Monica Tiberi, H Bart van der Worp, Ineke van Dis, W M Monique Verschuren, Simone Binno, and ESC Scientific Document Group. "2016 European Guidelines on cardiovascular disease prevention in clinical practice: The Sixth Joint Task Force of the European Society of Cardiology and Other Societies on Cardiovascular Disease Prevention in Clinical Practice (constituted by representatives of 10 societies and by invited experts)Developed with the special contribution of the European Association for Cardiovascular Prevention & Rehabilitation (EACPR)". en. In: *Eur. Heart J.* 37.29 (Aug. 2016), pp. 2315–2381.

[127] Joseph F Polak, Michael J Pencina, Allison Meisner, Karol M Pencina, Lisa S Brown, Philip A Wolf, and Ralph B D'Agostino Sr. "Associations of carotid artery intima-media thickness (IMT) with risk factors and prevalent cardiovascular disease: comparison of mean common carotid artery IMT with maximum internal carotid artery IMT". en. In: *J. Ultrasound Med.* 29.12 (Dec. 2010), pp. 1759–1768.

[128] Joseph F Polak, Michael J Pencina, Karol M Pencina, Christopher J O'Donnell, Philip A Wolf, and Ralph B D'Agostino Sr. "Carotid-wall intima-media thickness and cardiovascular events". en. In: *N. Engl. J. Med.* 365.3 (July 2011), pp. 213–221.

[129] Carlo A Porro, Valentina Cettolo, Maria Pia Francescato, and Patrizia Baraldi. "Functional activity mapping of the mesial hemispheric wall during anticipation of pain". en. In: *Neuroimage* 19.4 (Aug. 2003), pp. 1738–1747.

[130] Jonathan D Power, Bradley L Schlaggar, and Steven E Petersen. "Recent progress and outstanding issues in motion correction in resting state fMRI". en. In: *Neuroimage* 105 (Jan. 2015), pp. 536–551.

[131] Chengxuan Qiu and Laura Fratiglioni. "A major role for cardiovascular burden in age-related cognitive decline". en. In: *Nat. Rev. Cardiol.* 12.5 (May 2015), pp. 267–277.

[132] Azar Radfar, Shady Abohashem, Michael T Osborne, Ying Wang, Tawseef Dar, Malek Z O Hassan, Ahmed Ghoneem, Nicki Naddaf, Tomas Patrich, Taimur Abbasi, Hadil Zureigat, James Jaffer, Parastou Ghazi, James A Scott, Lisa M Shin, Roger K Pitman, Tomas G Neilan, Malissa J Wood, and Ahmed Tawakol. "Stress-associated neurobiological activity associates with the risk for and timing of subsequent Takotsubo syndrome". en. In: *Eur. Heart J.* 42.19 (May 2021), pp. 1898–1908.

[133] Mehdi Rahim, Bertrand Thirion, Claude Comtat, Gaël Varoquaux, and Alzheimer's Disease Neuroimaging Initiative. "Transmodal Learning of Functional Networks for Alzheimer's Disease Prediction". en. In: *IEEE J. Sel. Top. Signal Process.* 10.7 (Oct. 2016), pp. 120–1213.

[134] Pradeep S Rajendran, Ray W Chui, Olujimi A Ajijola, Marmar Vaseghi, J Andrew Armour, Jeffrey L Ardell, and Kalyanam Shivkumar. "Neural Control of Cardiac Function in Health and Disease". In: *Atlas of Cardiac Innervation*. Ed. by Vasken Dilsizian and Jagat Narula. Cham: Springer International Publishing, 2017, pp. 13–35.

[135] Javier Rasero, Amy Isabella Sentis, Fang-Cheng Yeh, and Timothy Verstynen. "Integrating across neuroimaging modalities boosts prediction accuracy of cognitive ability". en. In: *PLoS Comput. Biol.* 17.3 (Mar. 2021), e1008347.

[136] Silvia A Riccio, Andrew A House, J David Spence, Aaron Fenster, and Grace Parraga. "Carotid ultrasound phenotypes in vulnerable populations". en. In: *Cardiovasc. Ultrasound* 4 (Nov. 2006), p. 44.

[137] Raymond Salvador, John Suckling, Christian Schwarzbauer, and Ed Bullmore. "Undirected graphs of frequency-dependent functional connectivity in whole brain networks". en. In: *Philos. Trans. R. Soc. Lond. B Biol. Sci.* 360.1457 (May 2005), pp. 937–946.

[138] Clifford B Saper. "The central autonomic nervous system: conscious visceral perception and autonomic pattern generation". en. In: *Annu. Rev. Neurosci.* 25 (Mar. 2002), pp. 433–469.

[139] Stefan Schandelmaier, Matthias Briel, Ramon Saccilotto, Kelechi K Olu, Armon Arpagaus, Lars G Hemkens, and Alain J Nordmann. "Niacin for primary and secondary prevention of cardiovascular events". en. In: *Cochrane Database Syst. Rev.* 6 (June 2017), p. CD009744.

[140] Amy Isabella Sentis, Javier Rasero, Peter J Gianaros, and Timothy D Verstynen. "Integrating multiple brain imaging modalities does not boost prediction of subclinical atherosclerosis in midlife adults". en. In: *Neuroimage Clin* 35 (July 2022), p. 103134.

[141] Fred Shaffer, Rollin McCraty, and Christopher L Zerr. “A healthy heart is not a metronome: an integrative review of the heart’s anatomy and heart rate variability”. en. In: *Front. Psychol.* 5 (Sept. 2014), p. 1040.

[142] Kalyanam Shivkumar, Olujimi A Ajijola, Inder Anand, J Andrew Armour, Peng-Sheng Chen, Murray Esler, Gaetano M De Ferrari, Michael C Fishbein, Jeffrey J Goldberger, Ronald M Harper, Michael J Joyner, Sahib S Khalsa, Rajesh Kumar, Richard Lane, Aman Mahajan, Sunny Po, Peter J Schwartz, Virend K Somers, Miguel Valderrabano, Marmar Vaseghi, and Douglas P Zipes. “Clinical neurocardiology defining the value of neuroscience-based cardiovascular therapeutics”. en. In: *J. Physiol.* 594.14 (July 2016), pp. 3911–3954.

[143] Alessandro Silvani, Giovanna Calandra-Buonaura, Roger A L Dampney, and Pietro Cortelli. “Brain-heart interactions: physiology and clinical implications”. en. In: *Philos. Trans. A Math. Phys. Eng. Sci.* 374.2067 (May 2016).

[144] Joel Singer, Julian N Trollor, Bernhard T Baune, Perminder S Sachdev, and Evelyn Smith. “Arterial stiffness, the brain and cognition: a systematic review”. en. In: *Ageing Res. Rev.* 15 (May 2014), pp. 16–27.

[145] Jitka Sojkova, Samer S Najjar, Lori L Beason-Held, E Jeffrey Metter, Christos Davatzikos, Michael A Kraut, Alan B Zonderman, and Susan M Resnick. “Intima-media thickness and regional cerebral blood flow in older adults”. en. In: *Stroke* 41.2 (Feb. 2010), pp. 273–279.

[146] Ruixue Song, Hui Xu, Christina S Dintica, Kuan-Yu Pan, Xiuying Qi, Aron S Buchman, David A Bennett, and Weili Xu. “Associations Between Cardiovascular Risk,

Structural Brain Changes, and Cognitive Decline". en. In: *J. Am. Coll. Cardiol.* 75.20 (May 2020), pp. 2525–2534.

[147] Rajiv N Srinivasa, Heidi C Rossetti, Mohit K Gupta, Roger N Rosenberg, Myron F Weiner, Ronald M Peshock, Roderick W McColl, Linda S Hynan, Richard T Lucarelli, and Kevin S King. "Cardiovascular Risk Factors Associated with Smaller Brain Volumes in Regions Identified as Early Predictors of Cognitive Decline". en. In: *Radiology* 278.1 (Jan. 2016), pp. 198–204.

[148] M J Stampfer. "Cardiovascular disease and Alzheimer's disease: common links". en. In: *J. Intern. Med.* 260.3 (Sept. 2006), pp. 211–223.

[149] James H Stein, Claudia E Korcarz, R Todd Hurst, Eva Lonn, Christopher B Kendall, Emile R Mohler, Samer S Najjar, Christopher M Rembold, Wendy S Post, and American Society of Echocardiography Carotid Intima-Media Thickness Task Force. "Use of carotid ultrasound to identify subclinical vascular disease and evaluate cardiovascular disease risk: a consensus statement from the American Society of Echocardiography Carotid Intima-Media Thickness Task Force. Endorsed by the Society for Vascular Medicine". en. In: *J. Am. Soc. Echocardiogr.* 21.2 (Feb. 2008), 93–111, quiz 189–90.

[150] Andrew Steptoe and Mika Kivimäki. "Stress and cardiovascular disease: an update on current knowledge". en. In: *Annu. Rev. Public Health* 34 (Jan. 2013), pp. 337–354.

[151] Jerry Suls and James Bunde. "Anger, anxiety, and depression as risk factors for cardiovascular disease: the problems and implications of overlapping affective dispositions". en. In: *Psychol. Bull.* 131.2 (Mar. 2005), pp. 260–300.

[152] Ahmed Tawakol, Amorina Ishai, Richard Ap Takx, Amparo L Figueroa, Abdelrahman Ali, Yannick Kaiser, Quynh A Truong, Chloe Je Solomon, Claudia Calcagno, Venkatesh Mani, Cheuk Y Tang, Willem Jm Mulder, James W Murrough, Udo Hoffmann, Matthias Nahrendorf, Lisa M Shin, Zahi A Fayad, and Roger K Pitman. "Relation between resting amygdalar activity and cardiovascular events: a longitudinal and cohort study". en. In: *Lancet* 389.10071 (Feb. 2017), pp. 834–845.

[153] Ahmed Tawakol, Michael T Osborne, Ying Wang, Basma Hammed, Brian Tung, Tomas Patrich, Blake Oberfeld, Amorina Ishai, Lisa M Shin, Matthias Nahrendorf, Erica T Warner, Jason Wasfy, Zahi A Fayad, Karestan Koenen, Paul M Ridker, Roger K Pitman, and Katrina A Armstrong. "Stress-Associated Neurobiological Pathway Linking Socioeconomic Disparities to Cardiovascular Disease". en. In: *J. Am. Coll. Cardiol.* 73.25 (July 2019), pp. 3243–3255.

[154] Julian F Thayer and Richard D Lane. "Claude Bernard and the heart–brain connection: Further elaboration of a model of neurovisceral integration". In: *Neurosci. Biobehav. Rev.* 33.2 (Feb. 2009), pp. 81–88.

[155] Judith M Thornton, Tipu Aziz, David Schlugman, and David J Paterson. "Electrical stimulation of the midbrain increases heart rate and arterial blood pressure in awake humans". en. In: *J. Physiol.* 539.Pt 2 (Mar. 2002), pp. 615–621.

[156] Yunjie Tong, Lia M Hocke, Xiaoying Fan, Amy C Janes, and Blaise Deb Frederick. "Can apparent resting state connectivity arise from systemic fluctuations?" en. In: *Front. Hum. Neurosci.* 9 (May 2015), p. 285.

[157] C Triantafyllou, R D Hoge, G Krueger, C J Wiggins, A Potthast, G C Wiggins, and L L Wald. “Comparison of physiological noise at 1.5 T, 3 T and 7 T and optimization of fMRI acquisition parameters”. en. In: *Neuroimage* 26.1 (May 2005), pp. 243–250.

[158] Lena Tschiderer, Gerhard Klingenschmid, Lisa Seekircher, and Peter Willeit. “Carotid intima-media thickness predicts carotid plaque development: Meta-analysis of seven studies involving 9341 participants”. en. In: *Eur. J. Clin. Invest.* 50.4 (Apr. 2020), e13217.

[159] Jia Tuo, Yunhai Liu, Weihua Liao, Wenping Gu, Shuai Yang, Xinglin Tan, Tao Tang, Hua Chen, Jie Feng, Yanbin Wen, Wei He, and Qing Huang. “Altered brain volume and its relationship to characteristics of carotid plaques in asymptomatic patients”. en. In: *Medicine* 97.52 (Dec. 2018), e13821.

[160] Amna Umer, George A Kelley, Lesley E Cottrell, Peter Giacobbi Jr, Kim E Innes, and Christa L Lilly. “Childhood obesity and adult cardiovascular disease risk factors: a systematic review with meta-analysis”. en. In: *BMC Public Health* 17.1 (Aug. 2017), p. 683.

[161] G Valenza, R Sclocco, A Duggento, L Passamonti, V Napadow, R Barbieri, and N Toschi. “The central autonomic network at rest: Uncovering functional MRI correlates of time-varying autonomic outflow”. en. In: *Neuroimage* 197 (Aug. 2019), pp. 383–390.

[162] Anthony J M Verberne and Neil C Owens. “Cortical Modulation of theCardiovascular System”. In: *Prog. Neurobiol.* 54.2 (Feb. 1998), pp. 149–168.

[163] Timothy D Verstynen and Vibhas Deshpande. “Using pulse oximetry to account for high and low frequency physiological artifacts in the BOLD signal”. en. In: *Neuroimage* 55.4 (Apr. 2011), pp. 1633–1644.

[164] Salim S Virani, Alvaro Alonso, Hugo J Aparicio, Emelia J Benjamin, Marcio S Bittencourt, Clifton W Callaway, April P Carson, Alanna M Chamberlain, Susan Cheng, Francesca N Delling, Mitchell S V Elkind, Kelly R Evenson, Jane F Ferguson, Deepak K Gupta, Sadiya S Khan, Brett M Kissela, Kristen L Knutson, Chong D Lee, Tené T Lewis, Junxiu Liu, Matthew Shane Loop, Pamela L Lutsey, Jun Ma, Jason Mackey, Seth S Martin, David B Matchar, Michael E Mussolino, Sankar D Navaneethan, Amanda Marma Perak, Gregory A Roth, Zainab Samad, Gary M Satou, Emily B Schroeder, Svati H Shah, Christina M Shay, Andrew Stokes, Lisa B VanWagner, Nae-Yuh Wang, Connie W Tsao, and American Heart Association Council on Epidemiology and Prevention Statistics Committee and Stroke Statistics Subcommittee. “Heart Disease and Stroke Statistics-2021 Update: A Report From the American Heart Association”. en. In: *Circulation* 143.8 (Feb. 2021), e254–e743.

[165] Roberto Viviani, Irene Messina, and Martin Walter. “Resting state functional connectivity in perfusion imaging: correlation maps with BOLD connectivity and resting state perfusion”. en. In: *PLoS One* 6.11 (Nov. 2011), e27050.

[166] Tor D Wager, Christian E Waugh, Martin Lindquist, Doug C Noll, Barbara L Fredrickson, and Stephan F Taylor. “Brain mediators of cardiovascular responses to social threat: part I: Reciprocal dorsal and ventral sub-regions of the medial prefrontal cortex and heart-rate reactivity”. en. In: *Neuroimage* 47.3 (Sept. 2009), pp. 821–835.

[167] Ahad Wahid, Nishma Manek, Melanie Nichols, Paul Kelly, Charlie Foster, Premila Webster, Asha Kaur, Claire Friedemann Smith, Elizabeth Wilkins, Mike Rayner, Nia Roberts, and Peter Scarborough. "Quantifying the Association Between Physical Activity and Cardiovascular Disease and Diabetes: A Systematic Review and Meta-Analysis". en. In: *J. Am. Heart Assoc.* 5.9 (Sept. 2016).

[168] Tao Wang, Bin Mei, and Junjian Zhang. "Atherosclerotic carotid stenosis and cognitive function". en. In: *Clin. Neurol. Neurosurg.* 146 (July 2016), pp. 64–70.

[169] Wendy Wang, Faye L Norby, Kristen M George, Alvaro Alonso, Thomas H Mosley, Rebecca F Gottesman, Michelle L Meyer, and Pamela L Lutsey. "Association of Carotid Intima-Media Thickness and Other Carotid Ultrasound Features With Incident Dementia in the ARIC-NCS". en. In: *J. Am. Heart Assoc.* 10.9 (May 2021), e020489.

[170] Carrington R Wendell, Shari R Waldstein, Michele K Evans, and Alan B Zonderman. "Distributions of Subclinical Cardiovascular Disease in a Socioeconomically and Racially Diverse Sample". en. In: *Stroke* 48.4 (Apr. 2017), pp. 850–856.

[171] Carrington Rice Wendell, Alan B Zonderman, E Jeffrey Metter, Samer S Najjar, and Shari R Waldstein. "Carotid intimal medial thickness predicts cognitive decline among adults without clinical vascular disease". en. In: *Stroke* 40.10 (Oct. 2009), pp. 3180–3185.

[172] Wilby Williamson, Adam J Lewandowski, Nils D Forkert, Ludovica Griffanti, Thomas W Okell, Jill Betts, Henry Boardman, Timo Siepmann, David McKean, Odaro Huckstep, Jane M Francis, Stefan Neubauer, Renzo Phellan, Mark Jenkinson, Aiden Do-

herty, Helen Dawes, Eleni Frangou, Christina Malamateniou, Charlie Foster, and Paul Leeson. “Association of Cardiovascular Risk Factors With MRI Indices of Cerebrovascular Structure and Function and White Matter Hyperintensities in Young Adults”. en. In: *JAMA* 320.7 (Aug. 2018), pp. 665–673.

[173] P W Wilson, W B Kannel, H Silbershatz, and R B D’Agostino. “Clustering of metabolic factors and coronary heart disease”. en. In: *Arch. Intern. Med.* 159.10 (May 1999), pp. 1104–1109.

[174] M A Winkleby, D E Jatulis, E Frank, and S P Fortmann. “Socioeconomic status and health: how education, income, and occupation contribute to risk factors for cardiovascular disease”. en. In: *Am. J. Public Health* 82.6 (June 1992), pp. 816–820.

[175] David H Wolpert. “Stacked generalization”. In: *Neural Netw.* 5.2 (Jan. 1992), pp. 241–259.

[176] Jiawei Yin, Xiaoling Jin, Zhilei Shan, Shuzhen Li, Hao Huang, Peiyun Li, Xiaobo Peng, Zhao Peng, Kaifeng Yu, Wei Bao, Wei Yang, Xiaoyi Chen, and Liegang Liu. “Relationship of Sleep Duration With All-Cause Mortality and Cardiovascular Events: A Systematic Review and Dose-Response Meta-Analysis of Prospective Cohort Studies”. en. In: *J. Am. Heart Assoc.* 6.9 (Sept. 2017).

[177] Alberto Zanchetti. “The Hypertensive Patient With Multiple Risk Factors”. en. In: *Am. J. Hypertens.* 10.S7 (Oct. 1997), 223S–229S.